Intrinsic Near-Infrared Properties of the Variable Source Sagittarius A*

INAUGURAL-DISSERTATION

zur
Erlangung des Doktorgrades
der Mathematisch-Naturwissenschaftlichen Fakultät
der Universität zu Köln

vorgelegt von

Gunther Witzel
aus Bonn

Köln 2012

Berichterstatter: Prof. Dr. Andreas Eckart
Prof. Dr. Andreas Zilges

Prof. Dr. Peter Schneider

Tag der mündlichen Prüfung: 04. 04. 2012

Contents

Zusammenfassung **V**

Abstract **VII**

1. Introduction **1**
1.1. Adaptive optics measurements 3
1.2. The variable near-infrared source Sgr A* 6
1.3. Radiation mechanisms 8

2. A statistical analysis of the variability of Sgr A* in the near-infrared **13**
2.0.1. Definitions and concepts 13
2.0.2. NIR time series of SgrA* 15
2.1. Data reduction 17
2.1.1. The data base 17
2.1.2. Data reduction and flux density calibration 17
2.1.3. Light curves of Sgr A* 21
2.2. Statistical analysis of the flux density distribution 23
2.2.1. Optimal data visualization 23
2.2.2. Power-law representation of the intrinsic flux density distribution 27
2.3. Time series analysis 36
2.3.1. RMS-flux density relation 37
2.3.2. Simulating light curves 38
2.3.3. The structure function and the PSD 42
2.4. Extreme flux density excursions and the X-ray echo 51
2.4.1. Maximum expected NIR flux density 51
2.4.2. A possible explanation of the X-ray light echo 52
2.5. Summary 54

3. Near Infrared Polarimetry **57**
3.1. Basics of Polarimetry 58
3.2. Metallic reflection 60
3.3. The optical train of NACO 61

3.4. A model for the instrumental polarization of NACO 62
3.4.1. Instrumental polarization generated by M3 62
3.4.2. The IP of the adaptive optics module NAOS 64
3.4.3. The retarder plate 64
3.4.4. The entire instrumental polarization of NACO 66
3.5. The instrumental polarization in numbers 66
3.6. CONICA and the polarimetric analyzer 68
3.6.1. Müller-matrix for transmittance differences 70
3.6.2. Flat-field correction 71
3.7. Correcting the data for the instrumental systematics 74
3.8. Observations 75
3.8.1. The data 75
3.8.2. Gauging the model: standards and IRS16 stars 77
3.9. Comparison of different calibration methods 80
3.9.1. The “channel switch” method 80
3.9.2. The “boot strapping” method 82
3.9.3. Effects on time-resolved polarimetric measurements of Sgr A* 85
3.10. Summary 85

4. Conclusions and perspectives **87**

A. Data quality **89**

B. Light curves **91**

C. Flux density statistics **107**

D. Correction matrices for the optical components of NACO **109**

E. Supplement information for the polarimetric calibration of NACO **113**

Abbreviations **117**

Bibliography **119**

List of Figures **130**

List of Tables **131**

Danksagung **133**

Für meinen Vater

Zusammenfassung

Im Focus dieser Dissertation steht die hochvariable Strahlungsquelle im Zentrum unserer Milchstraße Sagittarius A* (Sgr A*). Die Arbeit umfasst zwei Teile: eine umfassende Darstellung der vorhandenen Ks-band (Nahinfrarot-) Beobachtungen mit dem Very Large Telescope der Europäischen Südsternwarte aus den letzten sieben Jahren und eine Analyse der instrumentellen systematischen Effekte bei polarimetrischen Messungen mit der adaptiven Optik NAOS und der Kamera CONICA.

Im ersten Teil charakterisiere ich die statistischen Eigenschaften der Nahinfrarotvariabilität von Sgr A*, einer Quelle, die in direktem Zusammenhang mit dem zentralen Schwarzen Loch im Zentrum unserer Milchstraße gesehen wird. Ich zeige, dass zur Beschreibung der Flussdichteverteilung ein einfaches Potenzgesetz geeignet ist. Somit kann die an anderer Stelle geäußerte Ansicht, dass die Flussdichteverteilung einen klaren Bruch und somit einen Hinweis auf zwei verschiedene Variabilitätsprozesse gibt, nicht bestätigt werden. Ich weise eine lineare Abhängigkeit der Variabilität von der Flussdichtehelligkeit der Quelle nach. Dieser Befund zusammen mit der Potenzgesetzverteilung impliziert ein phänomenologisches, formal nicht-lineares statistisches Variabilitätsmodell, mit dem es mir gelungen ist, Lichtkurven zu simulieren, deren Charakteristika und zeitliches Verhalten den beobachteten entsprechen, und die Vorhersagen für - im Beobachtungszeitraum nicht nachgewiesene - höhere Flußdichten und lange Zeitskalen zulassen. Mit diesem Modell lässt sich zeigen, dass ein Helligkeitsausbruch, wie er möglicherweise in den letzten 400 Jahren stattgefunden hat - wofür ein Lichtecho im Röntgenbereich emittiert von Molekülwolken in der weiten Umgebung von Sgr A* spricht - durchaus als Extremwert der gefundenen Statistik erklärbar ist. Weiterhin kann ich zeigen, dass Aussagen darüber, inwieweit ausgezeichnete Zeitskalen kürzer als 100 min bei dem zeitlichen Verhalten der Variabilität wesentlich sind, mit den hier präsentierten Daten nicht gemacht werden können. Dies ist eine Frage, die im Zusammenhang mit orbitalen Bewegungen in der Akkretionscheibe des Schwarzen Loches nahe am Ereignishorizont diskutiert wird.

Im zweiten Teil analysiere ich die instrumentelle Polarisation von NAOS/CONICA, einer Nahinfrarotkamera mit adaptiver Optik. Ziel war es, den Einfluss dieser systematischen Effekte auf Zeitreihen der polarimetrischen Parameter im Falle von Sgr A* zu bestimmen. Hierzu habe ich den Stokes/Müller-Formalismus zur Beschreibung der Effekte metallischer Reflektion auf den Polarisationszustand herangezogen. Das so be-

stimmte Modell der instrumentellen Polarisation wurde mit Beobachtungen von Kalibrationsquellen verglichen. Desweiteren habe ich verschiedene übliche Kalibrationsmethoden in ihrer Wirkung anhand von Simulationen und anhand dreier ausgewählter Lichkurven verglichen. Als Ergebnis habe ich eine deutliche Abhängigkeit der instrumentellen, maximal 4-prozentigen Polarisation von der Ausrichtung des Telekops und außerdem eine fehlerhafte Eichung der Vorzugsrichtung der Verzögerungsplättchens nachgewiesen. Mit dem neuen Modell der instrumentellen Polarisation wird es möglich sein, Genauigkeiten von etwa einem Prozentpunkt im Polarisationsgrad und, im Falle von Quellen mit Polarisationsgraden höher als 4%, 5° Winkelgenauigkeit zu ereichen. Für Zeitreihenmessungen wie im Falle von Sgr A* überwiegen die statistischen Fehler.

Abstract

This thesis on observational astronomy focuses on the highly variable near-infrared source Sagittarius A* (Sgr A*) at the center of the Milky Way, associated with the central $4 \times 10^6 M_\odot$ super-massive black hole. It is divided in two parts: a comprehensive data description of Ks-band measurements of Sgr A*, covering the last seven years of observations with the Very Large Telescope and the state-of-the-art instrument NAOS/CONICA, and an effort in polarimetric instrumentation, the calibration of the instrumental polarization properties of NAOS/CONICA in the Ks-band.

In the first part I characterize the statistical properties of the near-infrared variability of Sgr A*, the electromagnetic manifestation of the Galactic Center super-massive black hole, and find the flux density to be power-law distributed. I cannot confirm the evidence of a two state process with different flux density distributions behind the variability, as reported in other publications. I find a linear rms-flux relation for the flux density range up to 12 mJy on a timescale of 24 minutes. This and the power-law flux density distribution imply a phenomenological, formally non-linear statistical variability model with which I can simulate the observed variability and extrapolate its behavior to higher flux levels and longer timescales. I can show that a bright outburst within the last 400 years, that has been discussed as the possible reason for the X-ray emission from massive molecular clouds surrounding the Galactic Center, can be expected as an extreme value of our statistics without the need for a cosmic event. I give arguments, why data with our time support cannot be used to decide on the question whether the power spectral density of the underlying random process shows more structure at timescales below 100 min compared to what is expected from a red noise random process, as discussed in the context of orbiting hot spots in the accretion flow of the black hole.

In the second part I report on the results of calibrating and simulating the instrumental polarization properties of the Very Large Telescope adaptive optics camera system NAOS/CONICA (NACO) in the Ks-band. Here my goal was to understand the influence of systematic calibration effects on the time-resolved polarimetric observations of Sgr A*. I used the Stokes/Mueller formalism for metallic reflections to describe the instrumental polarization. The model is compared to standard-star observations and time-resolved observations of bright sources in the Galactic Center. I simulated the differences between calibration methods and tested their influence on three examples

of polarimetric Ks-band light curves of Sgr A*. I find the instrumental polarization to be highly dependent on the pointing position of the telescope and about 4% at maximum. I report a polarization angle offset of 13.2° due to a position angle offset of the $\lambda/2$-wave plate with respect to the data-header value that affects the calibration of NACO data taken before autumn 2009. With the new model of the instrumental polarization of NACO it is possible to measure the polarization with an accuracy of 1% in polarization degree. The uncertainty of the polarization angle is $\leq 5°$ for polarization degrees $\geq 4\%$. For densely sampled polarimetric time series I find that the improved understanding of the polarization properties gives results that are consistent with the previously used method to derive the polarization of Sgr A*. The difference between the derived and the previously employed polarization calibration is well within the statistical uncertainties of the measurements, and for Sgr A* they do not affect the results from our relativistic modeling of the accretion process.

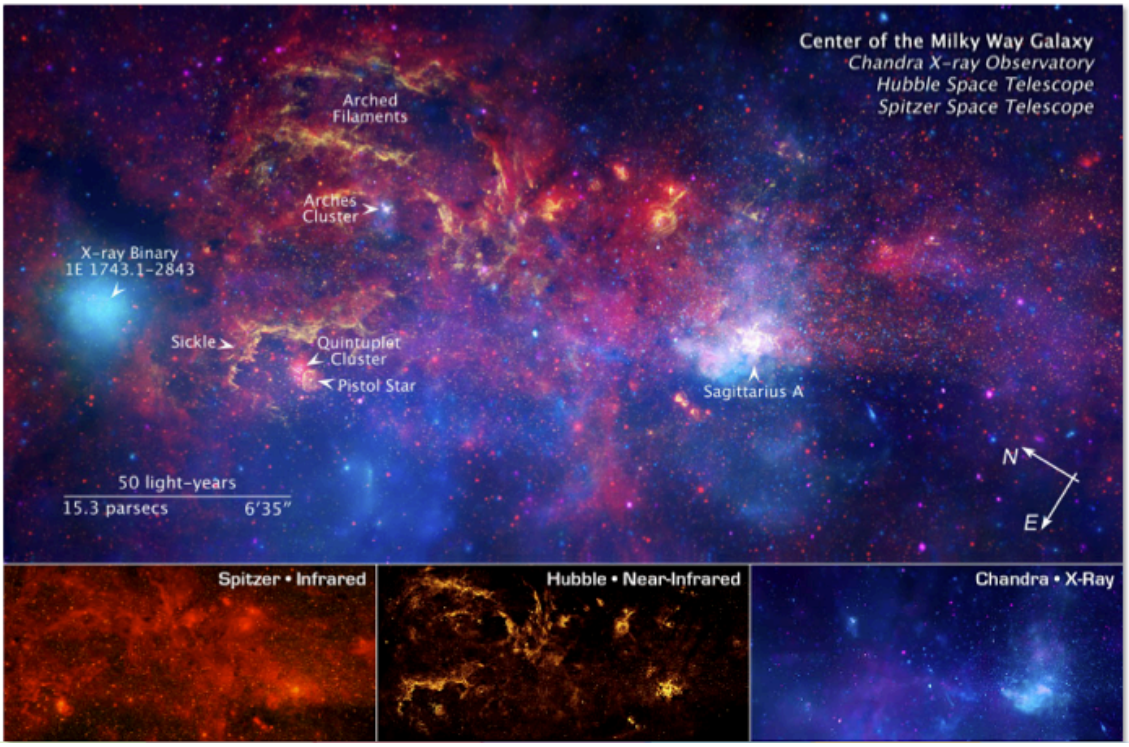

Fig. 1.1.: The Galactic Center in the near-infrared, infrared and X-ray. Credit for Spitzer image: NASA, Jet Propulsion Laboratory, and S. Stolovy (Spitzer Science Center/Caltech). Credit for Hubble image: NASA, ESA, and Q.D. Wang (University of Massachusetts, Amherst). Credit for Chandra image: NASA/CXC/UMass/D. Wang et al.

1. Introduction

The existence of galaxies is a discovery of the early twentieth century. Edwin Hubble found the Andromeda nebula to be far more distant than the objects in the Milky Way, and opened the door to extragalactic astronomy. Since then the development of new and powerful telescopes and principles, covering the whole electromagnetic spectrum, while reaching an astonishing resolution and sensitivity, has empowered astronomers to make unprecedented progress in discovering exotic objects and deciphering the physical processes in the near and far distant universe. Although seemingly trivial, an important step was the identification of our own Milky Way as a barred spiral galaxy. As a matter of fact, objects in our Milky Way allow the most detailed studies due to their proximity. A key method of astronomical research is to compare and complement our knowledge about the structure and the physical processes in our

Milky Way with what we know about other, more distant galaxies and vice versa. The distance of extragalactic objects has another aspect: because of the finite speed of light we are not only looking in to the far distance, but also into the past. Due to this fact we can infer information on the evolution of galaxies that happens on time scales no human life span or cultural deliverance could cover otherwise.

In the last decades a class of very exotic objects, first discovered as very luminous sources (the so called Quasars), started playing a central role: black holes. It is a widely accepted fact that all or at least most of the galaxies house a super-massive (millions and billions of solar masses) black hole at their center. The correlation of the masses with other properties of the housing galaxies implies a connection between the evolution of the super-massive black holes and the galaxies. The discovery of the radio source Sagittarius A* by Balick & Brown (1974) and the subsequent supply of evidence for a compact object with 4×10^6 solar masses in the center of our galaxy showed that our Milky Way is no exception in this respect. This makes the center of the Milky Way a unique opportunity to study processes associated with black holes and their interaction with the hosting galaxies in detail.

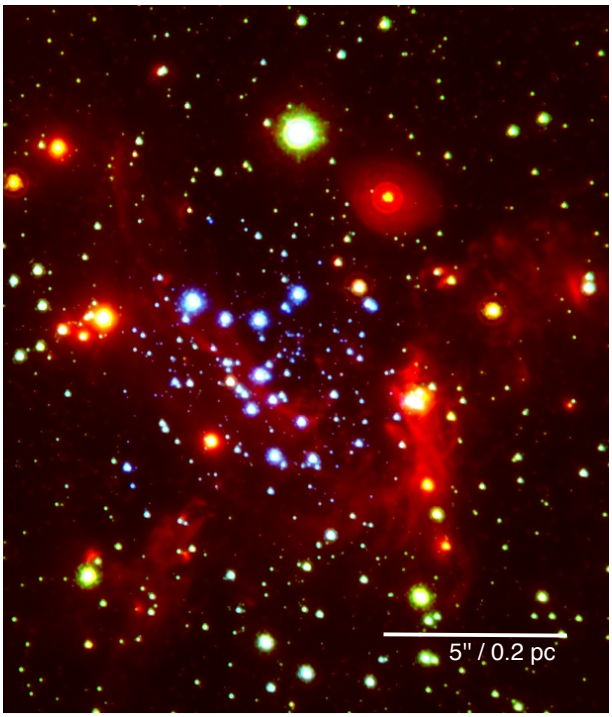

Fig. 1.2.: HKL-composite of the nuclear cluster.

The dynamical center of our galaxy is at a distance of about 8 kpc (e.g. Schödel et al. 2002). The innermost parsecs are a very dynamical region that contains a dense nuclear star cluster, dense molecular clouds, supernova remnants, a dense molecular ring

orbiting the nucleus on a scale of a few parsecs, and a three arm structure of ionized gas, the so called mini-spiral. This variety of structures and objects only can be investigated by combining observations at different wavelengths. Fig. 1.1 gives an impression, how different the innermost 240×120 light-years look like in the infrared, near-infrared and X-ray regime. At optical wavelengths the line of sight towards the very center is obscured by dust, resulting in an extinction of a factor of 10^{-12}. The multi-wavelength approach is necessary not only to reveal different constituents of the central region, but also different aspects of the radiation processes of the individual objects. The most particular object is situated at the heart of the nuclear star cluster: the radio, near-infrared and X-ray source Sagittarius A* (Sgr A*) that is the electromagnetic manifestation of the central black hole of our galaxy. The evidence that this object indeed can be associated with a super-massive black hole was established in essence by two important findings: the very little proper motion of the compact source itself, determined from VLBI radio measurements (Backer & Sramek 1999; Reid et al. 1999), and the precise determination of the orbits of in the meantime about 30 stars within the S-star cluster in the near-infrared (NIR), resulting in an estimation of the enclosed mass of about 4.4×10^6 solar masses (Eckart & Genzel 1996, 1997; Eckart et al. 2002; Schödel et al. 2002; Eisenhauer et al. 2003; Ghez et al. 2000, 2005, 2008; Gillessen et al. 2009). Fig. 1.2 shows a three color composite of NIR observations in the H-, Ks- and L-band of the innermost parsec around Sgr A*.

1.1. Adaptive optics measurements

Numerous measurements of the stellar orbits, and the observations this thesis is based on, have been conducted with one of the most advanced telescopes of our time, the Very Large Telescope (VLT) of the European Southern Observatory (ESO) in the north of Chile. This observatory, located at 2600 m over sea level on Paranal mountain in the middle of the Atacama desert, runs four telescopes with 8.2 m mirrors, each supported by an active optics system and equipped with optical and infrared instruments, and four smaller auxiliary telescopes.

The NIR instrument with which the astrometric measurements mentioned before and the database of this thesis have been obtained is NAOS/CONICA (NACO), mounted at one of the Nasmyth foci of the Unit Telescope 4 (Yepun). This instrument provides adaptive optics corrected observations in the wavelength range of $1-5\,\mu$m[1]. It consists of the adaptive optics system NAOS and the imager and spectrograph CONICA which includes a mode for differential polarimetric imaging.

[1]For the technical descriptions of the VLT and the AO system I follow Eckart et al. (2005), Bertram (2007) and Ageorges et al. (2007).

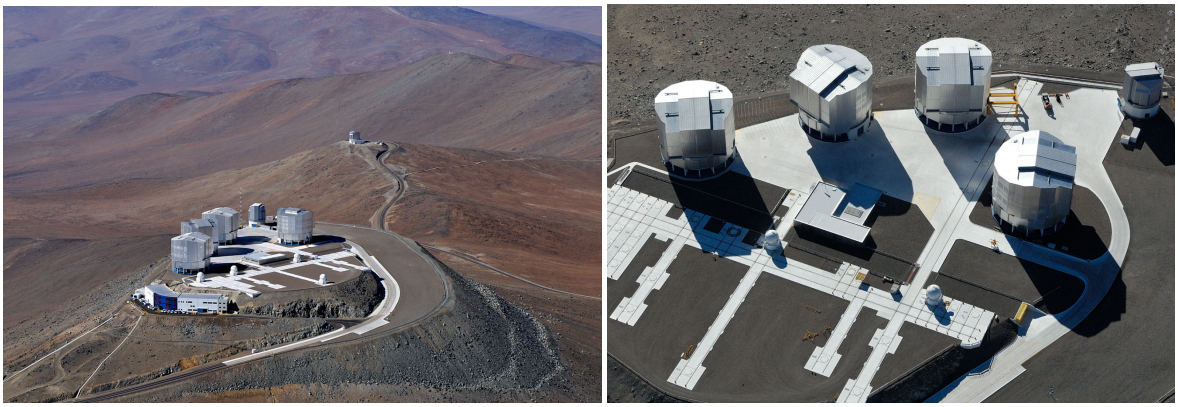

Fig. 1.3.: The Very Large Telescope observatory in the Atacama dessert in the north of Chile. Image courtesy:ESO/Hüdepohl (atacamaphoto.com)

Atmospheric turbulence on the line-of-sight causes fluctuations of the refractive index on a wide range of spatial and temporal scales. These fluctuations distort the otherwise flat wavefronts of light coming from far distant astronomical objects and hence do not allow a better resolution than about 0.7 arcsec in the NIR. For high angular resolution ground based imaging adaptive optics overcome this restriction and nearly reach a resolution at the diffraction limit.

Single aperture adaptive optics (AO) is a real time system for measuring phase perturbations of the wavefront by a phase reference source and correcting them in a closed loop. It enables the observer to obtain images at the diffraction limit with long integration times. The phase reference source has to be located within the so called isoplanatic patch around the target where the atmospheric transfer function is almost constant. The low frequency perturbations are usually corrected by an additional system, a so called tip-tilt sensor and correcting mirror. This system corrects for the displacement of the image on the detector. The higher frequency contributions are corrected with the higher order AO system that restores the wavefront with a deformable mirror (DM) that is located close to a pupil image of the conjugated atmospheric layer where the turbulence occurs. The DM has a size of 10 to 20 cm and is equipped with an arrangement of piezoelectric actuators (a few hundred for 8 m-class telescopes in NIR) that shape the mirror into a conjugate of the measured aberrations. The corrections have to be done on time scales of a few 10 to 100 Hz and with an accuracy of $\lambda/20$ to $\lambda/50$. The seeing and thus the requirements of an AO system depend on the wavelength. In NIR the isoplanatic patch is in the oder of $20''$. In the visible domain it can drop down to about $5''$. Common AO systems correct at wavelengths longer than 1 μm.

Fig. 1.5 shows a schematic view of a typical AO loop. For determining the distortions different devices are used: Shack-Hartmann, pyramid wavefront, and curvature sensors. The Shack-Hartmann device that is used in the case of NAOS divides the tele-

Fig. 1.4.: NAOS/CONICA at the Nasmyth focus of VLT UT 4, Yepun. The red cylinder is the camera system CONICA. Image courtesy:ESO.

scope pupil into multiple sub-pupils. Several images of the point-like reference source occur on the detector and the slope of the wavefront at the position of the sub-pupil can be measured from the displacement of the sub-images with respect to a reference position. The control loop between the wavefront sensor and the deformable mirror has to be very fast. The necessary commands have to be calculated within about 1 millisecond. In order to minimize the integration times a bright star (brighter than magnitude 17 in the visible and magnitude 10 in the NIR domain) is required. The necessity of the presence of bright stars reduces the sky coverage to a few percent. To overcome this problem artificial laser guide stars are used.

The corrected PSF typically contains a diffraction limited core and a broad seeing foot that has a similar or even larger size than the uncorrected seeing cloud.This is essential for the discussion of halo noise below (see section 2.2.2). A measure of the quality of the correction is the so called Strehl ratio, the ratio between the peak intensity of the corrected and the peak intensity of the theoretical point spread function (PSF). A demonstration of the improvement of the Strehl ratio by adaptive optics is shown in fig. 1.6.

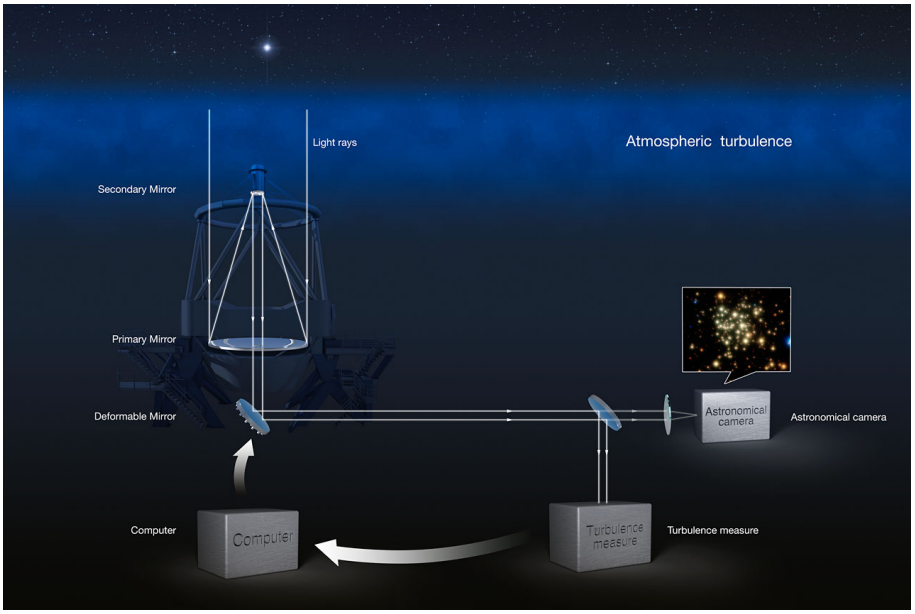

Fig. 1.5.: Scheme of an adaptive optics system. Image courtesy:ESO.

A comprehensive overview on Galactic Center research is given in Genzel et al. (2010), Eckart et al. (2005) and Melia (2007). A description of the physical mechanisms involved in imaging through the atmosphere and their mathematical treatment can be found in Bertram (2007) and references therein.

1.2. The variable near-infrared source Sgr A*

Sgr A*, located at the center of the our galaxy, is a highly variable near-infrared and X-ray source. While first detected as a bright, ultra compact, and comparatively steady radio source, the strong variability in the NIR and X-ray regime, and the variable polarization of the NIR emission provide reasonable ground to believe that properties of the black hole and its emission and accretion mechanisms can be studied at these wavelengths (Baganoff et al. 2001; Porquet et al. 2003, 2008; Genzel et al. 2003; Eckart et al. 2004, 2006a,c,b, 2008a,b,c; Yusef-Zadeh et al. 2006a,b, 2007, 2008; Dodds-Eden et al. 2009; Sabha et al. 2010).
Since the first near-infrared (NIR) polarimetric Wollaston prism observation of Sgr A* in 2004 (Eckart et al. 2006a), polarized flares have been regularly observed (Meyer et al. 2006a,b, 2007; Eckart et al. 2008a, Zamaninasab et al. 2010). In the NIR short bursts of increased emission exceeding 5 mJy occur four to six times a day and last typically for about 100 minutes (see Fig. 1.7). The linear polarization degrees can reach 20% to 50% of the total intensity. The polarized NIR flares are often associated with simultaneous X-ray flares (Baganoff et al. 2001; Porquet et al. 2003, 2008; Genzel et al. 2003; Eckart et al. 2004, 2006a,c,b, 2008a,b,c; Meyer et al. 2006a,b, 2007;

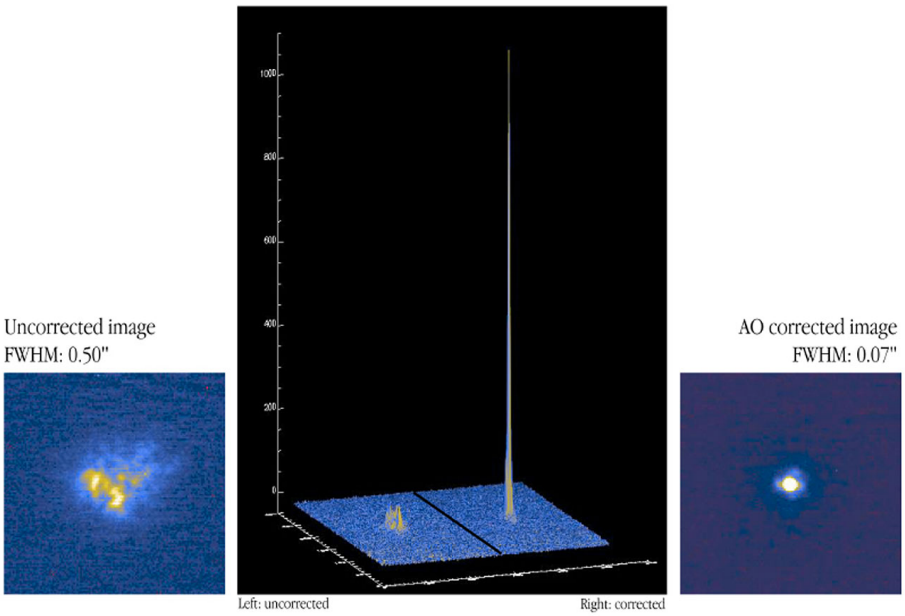

Fig. 1.6.: Improvement of the Strehl ratio by the AO system of NACO. Image courtesy:ESO.

Yusef-Zadeh et al. 2006a,b, 2007, 2008; Dodds-Eden et al. 2009; Sabha et al. 2010), suggesting Synchrotron Self-Compton (SSC) or inverse Compton emission as the responsible radiation mechanisms (Eckart et al. 2004, 2006a,c; Yuan et al. 2004; Liu et al. 2006; Eckart et al. 2012).

Considering the time behavior of the polarized NIR light curves some models that assume the variability to be linked to emission from single or multiple hot spots in the accretion disk near the last stable orbit of the black hole have been applied successfully to individual datasets (Meyer et al. 2006a,b, 2007; Zamaninasab et al. 2008). But within the discussion about the role of timescales and, in particular, the presence of a quasi-periodic oscillation (QPO) corresponding to orbital motion near the innermost stable orbit of the black hole, Do et al. (2009) argue that QPOs in total intensity light curves cannot be established with sufficient significance against random fluctuations. On the other hand, based on relativistic models, Zamaninasab et al. (2010) predicted a correlation between the modulations of the observed flux density light curves and changes in polarimetric data (also see Eckart et al. 2006a, Meyer et al. 2006a, Meyer et al. 2006b, Meyer et al. 2007; Eckart et al. 2008a, Cunningham & Bardeen 1973; Stark & Connors 1977; Abramowicz et al. 1991; Karas & Bao 1992; Hollywood et al. 1995; Dovčiak et al. 2004, Dovčiak et al. 2008). A comparison of predicted and observed light curve features (obtained from 7 nights of polarimetric observations with VLT and Subaru telescope) through a pattern recognition algorithm resulted in the detection of a signature possibly associated with orbiting matter under the influence of strong gravity. This pattern is found to be statistically significant against randomly

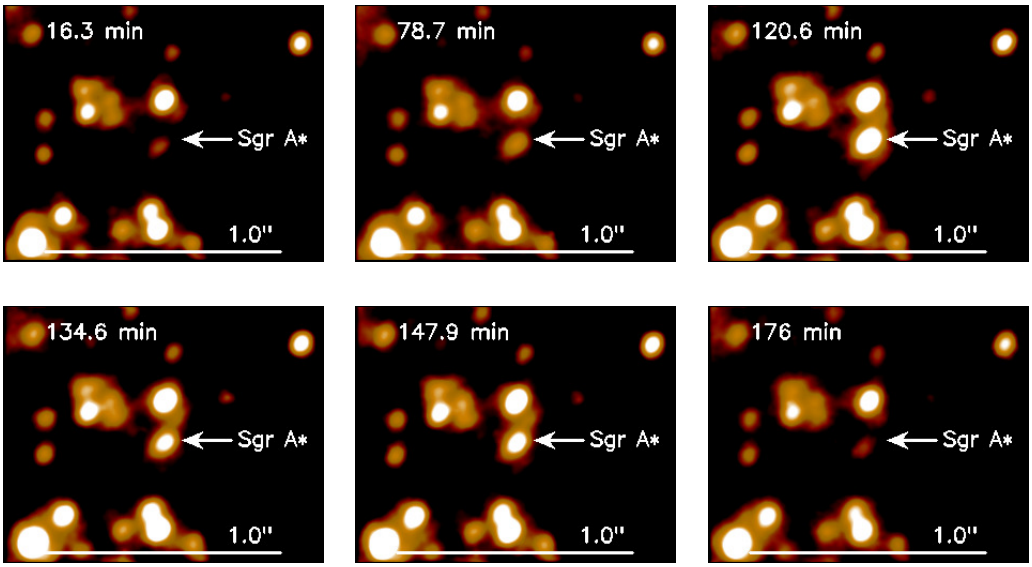

Fig. 1.7.: Sgr A* in a flaring state. These pictures show NIR K-band measurements from 2007.

polarized red noise.

1.3. Radiation mechanisms

Sgr A* is very under-luminous with respect to its Eddington limit ($10^{-8.5} L_{\mathrm{Edd}}$, Genzel et al. 2010). The Eddington luminosity is the maximum luminosity for a symmetrical accretion flow and is reached in the case of equilibrium between the inward driving gravitational force and the outward driving radiative force originating from the inner part of the accretion flow. This made it necessary to develop the so called radiatively inefficient accretion flow models.

Sgr A* shows a combination of time invariant and variable emission at all wavelengths[2]. While in the NIR and X-ray domain Sgr A* is highly variable, the emission in the radio domain is comparatively quiescent. As summarized in Genzel et al. (2010) this can be explained by a steady state emitting predominantly at radio and sub-millimeter wavelength originating from synchrotron emission of a thermal distribution of relativistic electrons, and a variable state generated by transiently heated electrons. In Fig. 1.8 I show the steady state spectral energy distribution (SED) of Sgr A* that, for the different parts of the spectrum, can be modeled by synchrotron emission from thermal and non-thermal relativistic electrons, inverse Compton up-scattering of the synchrotron photons by thermal electrons, and by a Bremsstrahlung contribution. It is important to note that the quiescent state SED at mid- to near-infrared wavelength

[2]In the description of the steady radiation mechanisms I follow Genzel et al. (2010).

is not well determined because the quiescent fluxes at these frequencies are below the detection limits. Because of the limited sensitivity and resolution of the instruments in addition to the extended structures visible at these wavelengths only upper limits could be obtained.

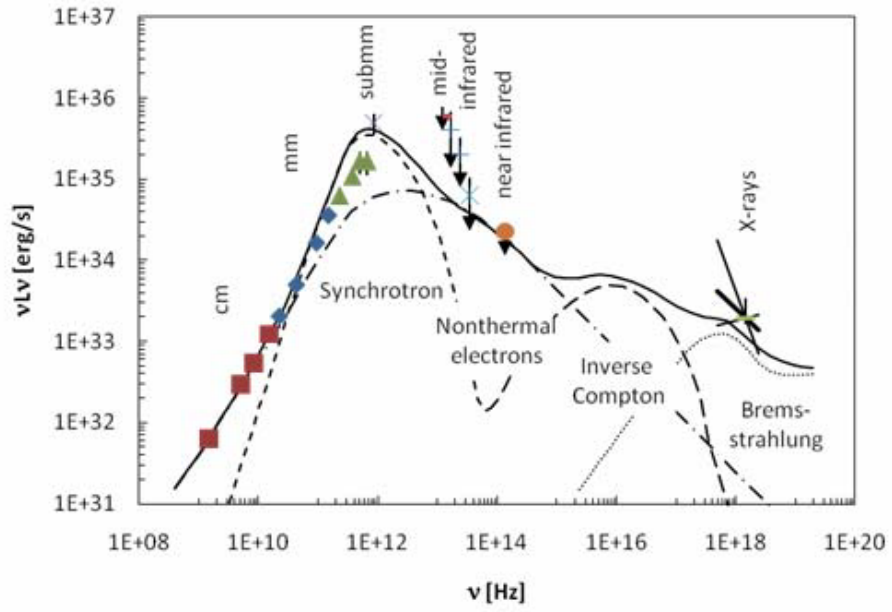

Fig. 1.8.: Steady state spectral energy distribution of Sgr A* from Genzel et al. (2010) and references therein. At the radio frequencies it is well described by synchrotron emission from thermal relativistic electrons (dashed line) with a flattening toward lower frequencies due to a contribution from non-thermal electrons (dashed-dotted line). The long dashed line represents a contribution of inverse Compton up-scattering of synchrotron photons by thermal electrons, the steady emission in the X-ray domain is dominated by Bremsstrahlung from the outer part of the accretion flow (dotted line).

The processes behind the variable part are still under debate. While many ideas and models are linked, as mentioned before, to accretion mechanism within an accretion disc, there are also approaches involving the foot point of a short jet (Falcke & Markoff 2000; Yuan et al. 2003; Markoff et al. 2001; Markoff & Falcke 2003). In Eckart et al. (2012) we show that a very likely explanation for the synchronous NIR and X-ray outbursts are synchrotron and synchrotron self-Compton mechanisms. In this model that is able to reproduce the behavior of all cases of observed simultaneous NIR and X-ray variability a synchrotron spectrum with a turnover frequency from optically thick to optically thin emission at a few hundred GHz to one THz is dominating the NIR emission. The X-ray flares are linked to this NIR-variability by inverse Compoton-scattering of the synchrotron photons by the same population of relativistic electrons that are generating the synchrotron radiation. Another important radiation mechanism is connected to correlations between the NIR and sub-mm variability, as they are re-

ported in Eckart et al. (2008c). Flares in the sub-mm occur with delays of 0.75 to 2 hours with respect to the NIR, and adiabatic expansion describes the evolving flux densities of both wavelength very well. The expansion speed for these emitting regions are of the order of 0.005 c and very low compared to the expected relativistic sound speed in orbital velocity in the vicinity of the super-massive black hole, resulting in either a large bulk motion of the adiabatically expanding source components or a strong confinement within the immediate surrounding of Sgr A*.

In the case of the relativistic modeling of the polarimetric Ks-band fluctuations in Zamaninasab et al. (2008) and Zamaninasab et al. (2010) the appearance of a possibly evolving hot spot for an observer far from the black hole under relativistic effects like boosting and lensing, and in particular the expected development of the polarization degree and angle, lead to a typical pattern of the polarimetric parameters, as mentioned above. This pattern basically includes a distinct total intensity peak, with a preceding rapid change in polarization angle (a common feature of many strong gravity scenarios) and a following peak in polarization degree. From an observer's point of view it is unfortunate that a strong depolarization attends the rapid change of the angle, because for a reliable determination of the polarization angle significant polarized flux is essential, and calibration problems or instrumental effects can easily generate similar patterns, as it is discussed in chapter 3.5.

In Genzel et al. (2010) the authors point out that "in the interpretation of the observed variability it is a key issue whether the brightest variable emission from Sgr A* at near-infrared and X-ray wavelength are statistical fluctuations from the probability distribution at low flux, or flare events with distinct properties". Indeed, the interpretation of a two state variability process with bright flares on top of moderate fluctuations seems to be suggested by the X-ray light curves that exhibit very bright distinct peaks. The authors speculate that the contrasting subsumption of the short timescale variability (on the one hand as an orbital signature in the accretion flow (e.g. Genzel et al. 2003; Eckart et al. 2006c; Dodds-Eden et al. 2009), and on the other hand as purely statistical fluctuations originating from featureless red noise (Do et al. 2009) can be explained by the transition between both variability states. They suggest a bright, polarized, power-law flux distributed flaring state with significant detection of QPOs, and a fainter, log-normal distributed stochastic process. This interpretation is based on the findings by Dodds-Eden et al. (2011), as described in detail in chapter 2.

The motivation for the work presented in this thesis is to investigate the robustness of the proposed double state scenario. It considers two aspects: the statistics of the Ks-band NIR variability, and the robustness of the calibration of the polarimetric observations. The key question mentioned above is answered in the next chapter as far as it is possible on the base of the available data.

In chapter 2 I present the results of my investigation of Ks-band flux density time series of Sgr A*. In chapter 3 I describe my analysis of the polarimetric mode of NAOS/CONICA. In chapter 4 I present conclusions and perspectives for future steps in analyzing the variability of Sgr A*. In the Appendix supplement information is presented.

2. A statistical analysis of the variability of Sgr A* in the near-infrared

2.0.1. Definitions and concepts

First, I want to introduce some mathematical concepts which the following analysis is based on. This serves as a short recapitulation of some important definitions. I follow the definitions and notation of Priestley (1982) and Theiler et al. (1993).
A random process is defined as a sequence of random variables $X(t)$, with t, in our case, a discrete sequence of time points. A time series is a sequence of measurements $x(t)$ which can be considered as a particular realization of the underlying random process. The probabilistic behavior is fully described if we are given the joint probability of $\{X(t_1),X(t_2),X(t_3),...,X(t_n)\}$ for all n and all choices for $t_1,t_2,t_3,...,t_n$. Under the assumption of weak stationarity (stationarity up to order $m = 2$), the mean, variance and the autocorrelation function become time invariant and contain all information about the main characteristics of the time behavior. A random process is stationary up to order $m = 2$ if, for any $t_1,t_2,t_3,...,t_n$ and k, all joint moments up to order $m = 2$ of $\{X(t_1),X(t_2),X(t_3),...,X(t_n)\}$ exist and equal the corresponding joint moments up to order $m = 2$ of $\{X(t_1+k),X(t_2+k),X(t_3+k),...,X(t_n+k)\}$. A stationary process is also ergodic, i.e. the mean, the variance, and the autocorrelation function can be obtained from the values at different time points of a single realization and do not require the availability of many realizations.
The autocorrelation function is defined as:

$$\rho(\tau) = \frac{\langle [X(t)-\mu][X(t+\tau)-\mu]\rangle}{\sigma^2} \quad , \tag{2.1}$$

with σ^2 the variance of the (stationary) random process and τ a time separation. The autocorrelation function quantifies, so to say, the memory of the random process, i.e. given a value at a time t it describes the time interval on which probabilistic predictions can be made with a certain accuracy. Another approach to describe the time behavior is the power spectral density (PSD), which, under general conditions of existence and stationarity, is defined for zero mean processes as the Fourier transform of the autocor-

relation function. The PSD describes the time behavior in terms of the average (over all realizations) of the contribution to the total "power" from components in $X(t)$ with a given frequency. A PSD has the properties of a probability distribution and, in particular, is normalized to the total power realized in the process. Statistical estimators of the PSD are called periodograms (see e.g. Priestley 1982).

The coherence timescale (or correlation timescale) of a process can be understood as the time separation of two points where the autocorrelation function falls below a certain value sufficiently close to zero and remains below this limit for larger τ, i.e. it represents the typical timescale where the process loses its memory.

As we will see in this chapter, light curves with a time correlation that is described by a power-law distributed PSD are of special interest. If the power-law slope is larger than unity such a correlation often is referred to as "red noise". In the case of red noise light curves the correlation timescale corresponds to the frequency where the power-law describing the PSD breaks (and, e.g., forms a constant plateau). If the length of the observation is shorter than the correlation timescale the observed time series is called weakly non-stationary.

The PSD might show several timescales where the characteristic of the correlation changes, e.g. represented by changes of the slope of the power-law. These distinct timescales do not represent the memory of the total process, but are also referred to as correlation timescales (this looser definition is plausible in the case of, e.g., a sum of independent processes with different correlation timescales).

An important tool to access information on the time behavior of a stationary process is the structure function. The first order structure function for a finite data sequence is defined in section 2.3.3. As Simonetti et al. (1985) show, the structure function is proportional to τ^2, where τ is a time separation much shorter than the shortest correlation time of the random process, and constant for τ greater than the longest correlation time scale. As we will see later, for non-equally spaced data the interpretation of the structure function becomes more challenging.

A stationary linear random process (discrete and equally sampled) is defined as:

$$X_k = \sum_{i=0}^{\infty} g_i \varepsilon_{k-i} \quad , \tag{2.2}$$

with X_k the kth data point, $\{\varepsilon_t\}$ being a purely random process (uncorrelated for all k) and $\{g_i\}$ a sequence of constants satisfying $\sum_{i=0}^{\infty} g_i^2 < \infty$. If X_k for each k is Gaussian distributed, it is called a Gaussian linear random process. Finite discrete parts of a realization of a Gaussian linear random process can be obtained for any PSD by drawing Fourier coefficients (for each frequency) from a zero mean Gaussian distribution with width σ proportional to the PSD value, and subsequent Fourier transformation to the time domain (Timmer & Koenig 1995).

2.0.2. NIR time series of SgrA*

Since the first detection of variable emission of Sgr A* in the NIR in 2003 (Genzel et al. 2003), apart from Zamaninasab et al. (2010) a number of publications concentrated on the statistical properties of the flaring activity rather than on interpreting individual observations. Based on NIR light curves of 7 nights observed with Keck telescope Do et al. (2009) analyzed the flux distribution of Sgr A* and the significance of quasi periodic oscillations, finding a pure red noise behavior. They conclude that during fainter states of Sgr A* at maximum 35% of the flux arising at the position of Sgr A* is of stellar origin, attributing the major part to a continuously variable process associated with the black hole. On the base of 14 light curves observed between 2004 and 2008, including very long alternating observations with VLT and Keck, Meyer et al. (2009) discovered first a dominant timescale at about 150 min, supporting linear scaling relations of break timescales of the PSD with the black hole mass. They determined the power-law slope of the high frequency part of the PSD to be 2.1 ± 0.5. A wide multi-wavelength study was conducted by Yusef-Zadeh et al. (2009), including 7 half days of Hubble space telescope data and 6 nights of VLT data, observed alternating in NIR wave-length regime. The authors analyzed the flux density histograms and modeled typical light curves by a sum of Gaussian profiles. Bremer et al. (2011) investigated the H-Ks-band spectral index[1] for bright phases of Sgr A* based on an unprecedentedly large database covering about seven years of NIR VLT data, and found a spectral index of $\alpha = -0.7$ as can be expected for pure synchrotron radiation. An analysis by Eckart et al. (2012) of 8 simultaneous X-ray and NIR flares in combination with multi-wavelength observations in 2009 shows that a robust description of all multi-wavelength flare events only can be reached under the assumption of a synchrotron - synchrotron self-Compton radiation mechanism.

The up to now most comprehensive statistical approach in the analysis of the Ks-band total intensity variability observed with NACO at the VLT has been conducted by Dodds-Eden et al. (2011). In this analysis the authors give an overview about the difficult confusion situation in the crowded field around Sgr A* that makes an analysis of the faint emission difficult. They also emphasize the importance of these faint states for the overall statistical evaluation of the variability of Sgr A*. The authors analyzed all VLT K-band data between 2004 and 2009, resulting in a detailed investigation of the flux density statistics. Based on the flux density histogram the authors claim the evidence for two states of variability, a log-normal distributed quiescent state for fluxes < 5 mJy, and a power-law distributed flaring state for fluxes > 5 mJy, arguing that it seems to be very unlikely that the same variability process is responsible for both high

[1] The spectral index is a measure of the dependence of the flux density on the observational frequency. For the flux density S and the frequency ν it is defined as $\alpha(\nu) = \frac{d\log[S(\nu)]}{d\log[\nu]}$.

and low flux emission from Sgr A*. As a description for the observed distribution of the flux density x (measured in mJy) Dodds-Eden et al. (2011) suggest the following probability density:

$$P_{0+\mathrm{err}}(x) = \int P_0(x') \frac{1}{\sqrt{2\pi}\sigma_{\mathrm{obs}}(x)} \exp\left[\frac{-(x-x')^2}{2\sigma_{\mathrm{obs}}(x)^2}\right] dx' \tag{2.3}$$

i.e., a convolution of an Gaussian error with flux density-dependent width

$$\frac{\sigma_{\mathrm{obs}}}{\mathrm{mJy}} = 0.174 \cdot \left(\frac{x}{\mathrm{mJy}}\right)^{0.5} \tag{2.4}$$

and an intrinsic two state probability density:

$$P_0(x) = \begin{cases} kP_{\mathrm{logn}}(x) & : \quad x \leq x_b + x_t \\ kP_{\mathrm{logn}}(x_t + x_b)\left(\frac{x-x_b}{x_t}\right)^{-s} & : \quad x > x_t + x_b \end{cases} \tag{2.5}$$

with k a dimensionless normalizing factor, and the log-normal part defined as

$$P_{\mathrm{logn}}(x) = \frac{1}{\sqrt{2\pi}\sigma_* (x-x_b)} \exp\left\{-\frac{\left[\ln\left(\frac{x-x_b}{\mathrm{mJy}}\right) - \mu_*\right]^2}{2\sigma_*^2}\right\} \tag{2.6}$$

The parameters of their best fit model are $\sigma_* = 0.75$, $\mu_* = 0.05$, $s = 2.7$, $x_t = 4.6$ mJy, and $x_b = 3.59$ mJy (here the unit of the probability density is mJy^{-1}).

My statistical analysis presented in this thesis serves the following goals:

- to provide a more comprehensive, uniformly reduced data set of Ks-band observations from 2003 to early 2010;
- to conduct a rigorous analysis of the observed flux density distribution;
- to explain why a proper statistical analysis of the Ks-band light curves cannot reproduce the results found by Dodds-Eden et al. (2011);
- to conduct a rigorous time series analysis on the base of a representative dataset;
- to propose a comprehensive statistical model that, using standard methods for generating Fourier transform based surrogate data, describes all aspects of the observed (total intensity) data and allows to simulate light curves with the observed time behavior and flux density distribution;
- and to investigate extreme variability events in the context of my statistics.

2.1. Data reduction

In the following I describe the data and the reduction methods I applied in order to obtain time-resolved photometric information on Sgr A*. Whereas the data base in large portions is the same as used for the analysis by Dodds-Eden et al. (2011), I have chosen different reduction methods: Lucy-Richardson deconvolution in order to guarantee the best possible isolation of the target sources from nearby point-like sources and to minimize the contribution of extended flux, a well controlled flux density calibration with 13 stars, and an objective quality cut based upon seeing and Strehl ratio values.

2.1.1. The data base

My analysis is based on ESO archive data. All observations have been conducted with the NIR adaptive optics instrument NAOS/CONICA at the Very Large Telescope (VLT) in Chile (Lenzen et al. 2003; Rousset et al. 2003). I included all available Ks-band frames of the central cluster of the GC from early 2003 to mid of 2010. For all observations the NIR wavefront sensor of the NAOS adaptive optics system was used to lock on the NIR bright supergiant IRS 7 (variable, $m_{\mathrm{Ks}} = 6.5$ in the 1990s, $m_{\mathrm{Ks}} = 7.4$ in 2006 and $m_{\mathrm{Ks}} = 7.7$ in 2011, $5.6''$ north of Sgr A*). Two different cameras, S13 and S27, with $13''$ and $27''$ field of view[2], respectively, and a polarimetric mode with inserted Wollaston prism and mask have been available. The latter restricted the area of calibrators that are in common for all frames, to the innermost arcsecond around Sgr A*.

I concentrated on datasets with a length of more than 40 minutes (shorter datasets are often severely affected by bad weather conditions in which case the observer decided fast to change to another wavelength or target). Problematic sets or frames, which showed particular behavior during the basic reduction steps or do not show Sgr A* or a sufficient number of calibrators, have not been included for the photometric analysis. Ultimately I investigated 12855 frames photometrically. Table B.1 shows a list of all datasets that are part of this analysis. Two restrictions for timing analysis are obvious: Sgr A* is observed best in the second half of the night in the winter of the southern hemisphere. At other times Sgr A* is located below or close to the horizon or not observable at all due to daylight.

2.1.2. Data reduction and flux density calibration

I performed every reduction step for every frame as uniformly as possible. The reduction included basic steps like a careful sky subtraction and flat fielding, and correction

[2] and accordingly with different pixel sampling

for bad pixels. For total intensity data I used a sky flat field if available, for polarimetric data a lamp flat field (Witzel et al. 2011). Most of the data was observed using a jitter routine with random offsets to prevent systematical influences on the measurements by detector artifacts. These offsets need to be detected and corrected for to guarantee stable aperture photometry at a constant position. This was achieved with a cross correlation algorithm for sub-pixel accuracy alignment (ESO Eclipse Jitter, Devillard 1999). For each aligned frame I determined an estimate of the point spread function (PSF) with the IDL routine Starfinder (Diolaiti et al. 2000) using isolated stars in the $2''$ surrounding of Sgr A*. The PSF-fitting algorithm of Starfinder provided an estimate of the extended background in each single frame and a list of detected stars with position and relative flux density. I decided not to use the values resulting from Starfinder photometry (for a detailed reasoning see below). Instead I used the Lucy-Richardson (LR) deconvolution algorithm to separate neighboring point-like sources. In order to reduce the contribution of artificial point-like sources that the LR algorithm randomly creates from extended flux I subtracted half the average over the background frame obtained by Starfinder as a constant value from each image. This significantly reduces the white noise contribution to the photometric measurement. In the case of polarization data I aligned all (four to six) polarization channels of each observation night with the cross correlation algorithm, and in the case of data observed with the different pixel scale of the S27 camera ($0.02715''$) I resampled the pixel scale to $0.01327''$ (S13). Finally a beam restoration was carried out with a Gaussian beam of a FWHM corresponding to the resolution at 2.2μm (~ 60 mas).

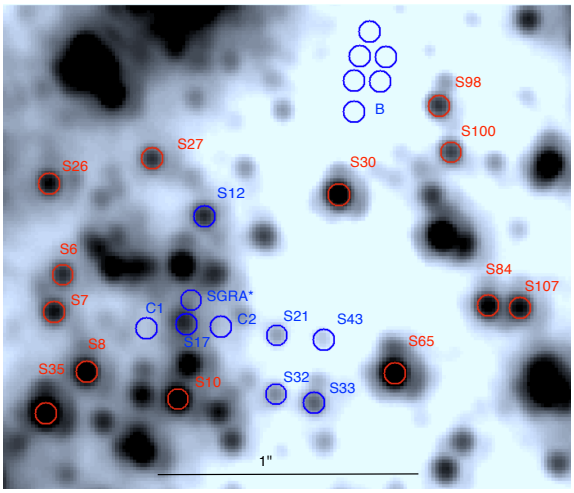

Fig. 2.1.: Ks-band image from 2004 September 30. The red circles mark the constant stars (Rafelski et al. 2007) which have been used as calibrators, the blue the position of photometric measurements of Sgr A*, comparison stars and comparison apertures for background estimation. Source identifications from Gillessen et al. (2009).

After the described preparative steps I conducted aperture photometry with 8 back-

star	m_{Ks}	flux density [mJy]
S26	14.94	6.79
S27	15.41	4.41
S6	15.35	4.66
S7	14.92	6.92
S8	14.21	13.31
S35	13.20	33.74
S10	13.95	16.91
S65	13.58	23.78
S30	14.12	14.46
S98	15.27	5.01
S100	15.29	4.92
S84	14.66	8.79
S107	14.82	7.59

Table 2.1.: This table shows a list of my calibrators. The flux density for each star was calculated correcting for extinction with $m_{\text{ext}} = 2.46$.

ground apertures and at the position of 13 constant calibrators (Rafelski et al. 2007), of 6 comparison stars, and at the position of Sgr A* (see Fig. 2.1). The background was estimated at the location of lowest background (6 apertures) and close to Sgr A* (2 apertures) where no obvious point-like source is visible. I applied a circular masking of radius $0.04''$ at the measurement positions. For a small number of observations, according to the available field of view, I accepted a smaller set of calibrators (at least seven).

The positions of the apertures in each night have been defined as consistently as possible: For Sgr A* with the help of its brighter states, for the stars with the help of mosaics (averages over the single frames of one night in order to increase the signal to noise and to also estimate the centroid of the fainter comparison stars) carefully following their proper motions. For the background apertures and the aperture of Sgr A* when it was faint I conducted triangulation relative to nearby stars. One set of positions then was used for all frames of the corresponding night. For some polarimetric observations NACO was rotated. In these cases I determined a rotation matrix for the position coordinates, making them comparable to the closest unrotated observations.

For each aperture I summed up its total content in analog-to-digital units (ADU). For the polarimetric data the obtained ADU values of orthogonal channels were added. I subtracted the average background value (B-apertures) in ADU from the calibrator values and conducted a flux density calibration using the photometric values for the calibrators in Tab. 2.1.2 (R. Schödel, priv. communication). Because of the high proper motions of the stars within this field the state of confusion of the calibrators

changes from epoch to epoch. I applied the following algorithm to reduce the epoch-dependent systematic error of the calibration:
First I calculated for each calibrator k the quantity:

$$\frac{f_k}{\mathrm{ADU}} = \frac{c_k}{\mathrm{ADU}} \cdot 10^{0.4 \cdot m_{\mathrm{ref}}} \quad , \tag{2.7}$$

with c_k the background subtracted ADU values for the k-th calibrator, and m_{ref} its reference magnitude. I sorted these values, rejected the three largest and the three smallest values (for the data sets with less calibrators I accordingly reject a smaller number), and took the arithmetic average f_0 over the remaining values. With the zero point from Tokunaga (2000) I then obtained the magnitude m_A and flux density F_A for each aperture A by

$$\begin{aligned} m_A &= -2.5 \cdot \log\left(\frac{c_k}{f_0}\right) \\ F_A &= 667 \cdot 10^3 \cdot 10^{-0.4 \cdot (m_A - m_{\mathrm{ext}})} \quad , \end{aligned} \tag{2.8}$$

with $m_{\mathrm{ext}} = 2.46$ the K-band extinction correction as determined in Schödel et al. (2010). This procedure ensures a best possible constance of the flux density calibration under the changing conditions of each dataset.
As a last step I collected parameters for each frame that provide information on the data and calibration quality and allowed me to reject data points based on objective criteria. These parameters are: Julian date, integration time (NDITxDIT), rotator position angle (orientation of NACO), airmass, guide star seeing, coherence time of the atmosphere, camera, all obtained from the header of the fits data, and the number of stars detected by Starfinder, the Strehl ratio calculated from the extracted PSF using the ESO Eclipse routine STREHL, the average deviation of the calibrators from their literature value, the RMS of the values f_k, and, as the most important quality check, the average flux of the calibrators. This last quantity is obtained for each frame by dividing the single measured flux density by the reference value and averaging over all available (i.e. not rejected) calibrators.
I emphasize that both methods - PSF-fitting and Lucy-Richardson aperture photometry - for estimating the flux density of a point source are in general equivalently well working as Meyer et al. (2008) have shown. On the other hand, in the case of the presence of extended flux underlying a (in comparison to the background) dim and confused point source observed under varying correction performance of the AO-system, the fitting statistics (i.e. the way Starfinder divides the given flux at a position into background and point source flux, the over-estimation of the flux due to noise-peaks if the center of the fit is not fixed, and the statistics of non-detections due to the quality thresholds

set in Starfinder) are difficult to control for this big data set with inhomogeneous correction conditions. I have to mention that also deconvolution has drawbacks, namely a lower astrometric accuracy I have to account for with a suitable big aperture. But the statistics of the interplay between the background (coming from non-resolved sources, truly extended emission and PSF contributions from the surrounding point sources), AO and point-like flux at a given position is directly propagated to the statistics of the measured fluxes, which is crucial for understanding the instrumental influence on my flux statistics. Especially my statistics do not suffer from non-detections that might introduce a selection effect. I will come back to the measurement statistics in section 2.2.

2.1.3. Light curves of Sgr A*

As a result of the reduction procedure described in section 2.1.2 I obtained the data shown in the upper panel of Fig. 2.2. For convenience and following the visualization used in Dodds-Eden et al. (2011) I show a concatenated light curve with all time gaps longer than 30 minutes removed. This visualization shows the data of all nights as a pseudo-continuous light curve allowing for a comparison of the variability and the confusion in each epoch. A visualization of the true time support is presented in Fig. 2.3. The timing analysis in section 2.3 is based on the true time support, and not on the concatenated light curve.

These 12855 data points still include points of bad observation conditions and insufficient calibration reliability. I used an objective frame rejection algorithm by incorporating information on seeing (only frames with seeing $< 2''$ accepted), Strehl ratio (only frames $> 6\%$), fraction of stars detected by Starfinder[3], the standard deviation of the f_0-values (obtained from the individual calibrators for each frame) normalized by the average f_0-value (only frames $< 16\%$), and the normalized average calibrator flux density as described in section 2.1.2 (only frames > 0.96 and < 1.04).

The top panel of Fig. 2.2 additionally shows a long-time trend of the data from year to year. With respect to these "offsets" of the lowest measured flux densities between the years I follow the analysis by Dodds-Eden et al. (2011) and their conclusion that confusion by faint stars is responsible for this long-time trend. In order to make the different years comparable I subtracted the median of the lowest 5% of each epoch, resulting in 0 mJy for 2003, 0.3 mJy for 2004, 1.0 mJy for 2005, 1.0 mJy for 2006, 1.3 mJy for 2007, 2.8 mJy for 2008, 2.1 mJy for 2009, and 0.7 mJy for 2010. The strong

[3]This is a method to reject frames of worse quality than the majority of the individual observation night. For each sub-frame of the night (i.e. the part of the jittered frames that is common to all) I count the stars detected by Starfinder. I then calculate the average number of detections over the night and the standard deviation and reject all frames with a negative deviation from the average of more than 1.7 times the standard deviation.

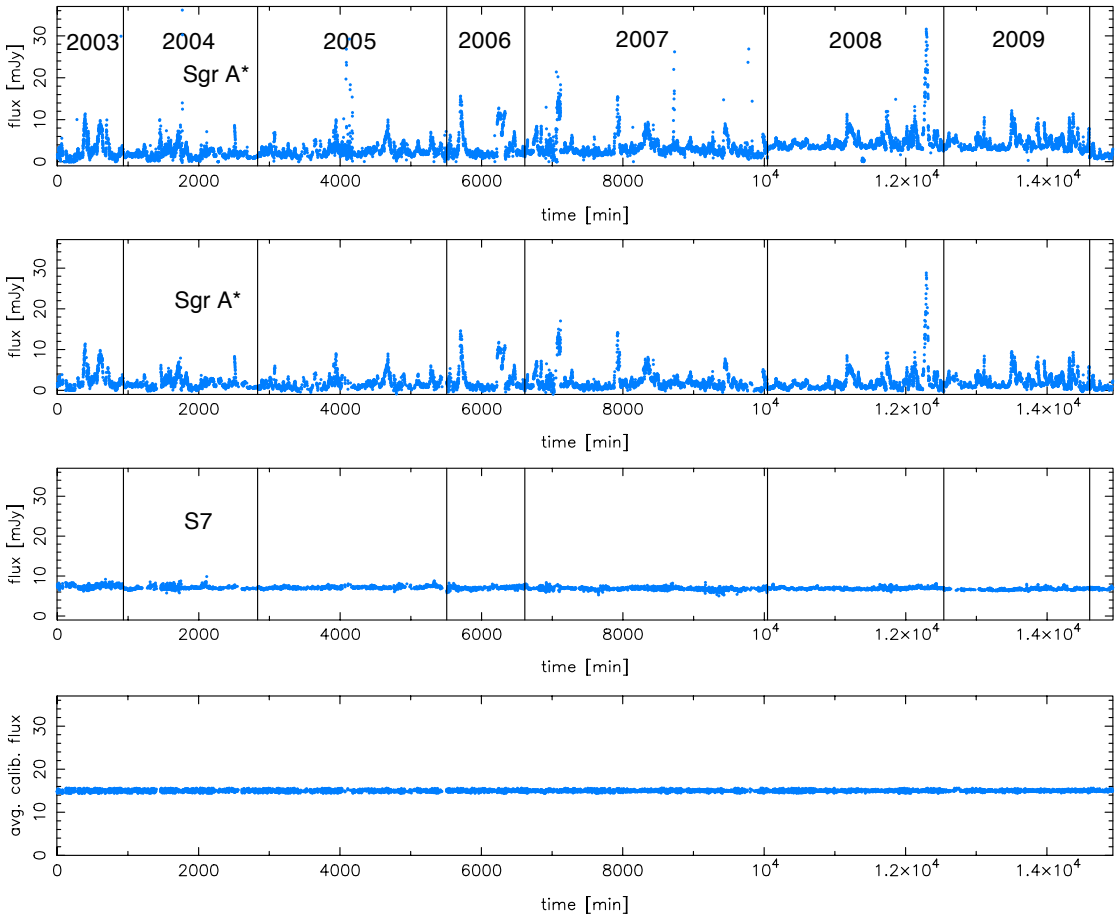

Fig. 2.2.: The concatenated light curve of Sgr A* and S7, time gaps longer than 30 minutes removed. The top panel shows the result of aperture photometry before the quality cut, the next panel the same data after quality cut. The third shows a light curve of S 7, a nearby star that has been used as a calibrator. The time gaps are the result of the rejection procedure described in section 2.1.2. The lower panel shows the average ratio between the measured flux of each calibrator and its reference value (Tab. 2.1.2), scaled with a factor of 15. Its noise corresponds to the error a hypothetical noise-free aperture with a flux density of 15 mJy would have only due to the uncertainties of the calibrators.

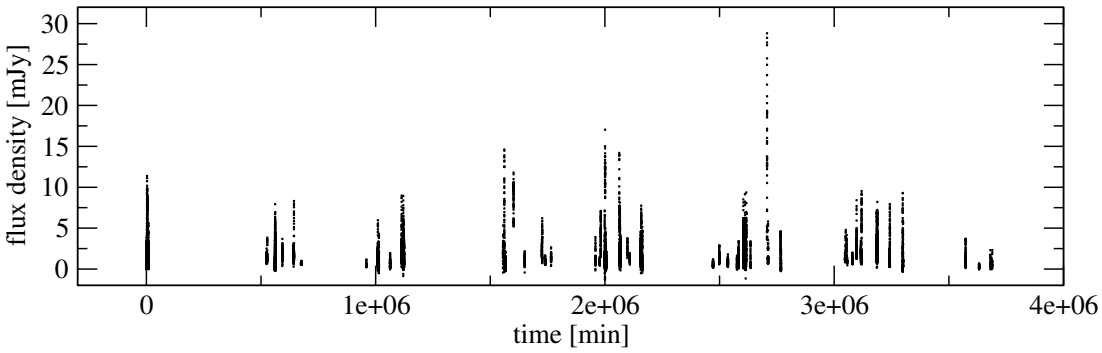

Fig. 2.3.: Light curve of Sgr A* like in Fig. 2.2. In this case no time gaps have been removed, the data is shown in its true time coverage. A comparison of both plots shows: only about 0.4% of the 7 years have been covered by observations.

confusion by the star S2 in 2003 and 2004[4] could be suppressed by the deconvolution reduction step.

The second panel of Fig. 2.2 shows the data after quality cut and subtraction of the faint stellar contribution. For comparison and as an indicator of the calibration stability I show additionally the light curve of one of the calibrators, S7, in the third panel, and in the lowest the average calibrator flux density scaled to 15 mJy.

For a more detailed inspection I present 112 data blocks (defined by continuity, not interrupted by gaps longer than 30 minutes) in Appendix B.

2.2. Statistical analysis of the flux density distribution

In this section I investigate the properties of the flux density statistics of the variability of Sgr A*. This analysis gives information on both the intrinsic flux density distribution of the variability as well as the instrumental effects within our measurements. The differentiation between instrumental features within the distribution and the intrinsic component turns out to be crucial in the context of the question whether the intrinsic flux density distribution provides evidence for two physical mechanisms at work. Additionally, this analysis allows me to develop a full statistical model of the variability of Sgr A* in the next section.

2.2.1. Optimal data visualization

The first step in the analysis of the flux density distribution of Sgr A* is a proper graphical representation of the data in form of a histogram. Histograms are non-parametric

[4] which is the reason why Dodds-Eden et al. (2011) did not include the 2003 data and which is clearly visible in the 2004 epoch of their uncorrected light curve

estimators for the probability density behind the sample. A representation of my data in a simple flux density histogram, normalized by total number of points and bin size, is shown in Fig. 2.4.

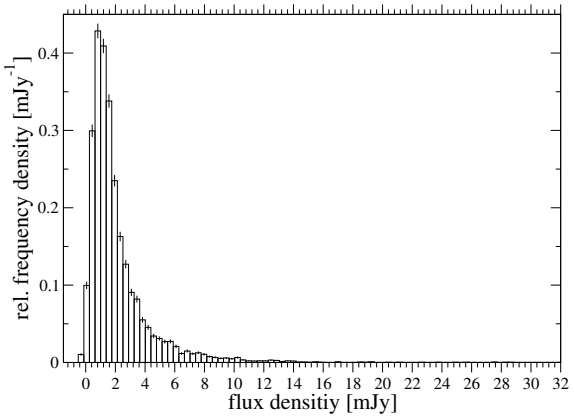

Fig. 2.4.: Flux density histogram of Sgr A*, based on the data shown in Fig. 2.2

To investigate the high flux density tail of this distribution a logarithmic histogram with an equally spaced logarithmic binning is best suited. The number of bins for a given data range is a crucial parameter for the evaluation of the structure of the sample distribution. Following the study of Knuth (2006) I first determine the best bin size. As the author points out, the idea is to choose a number of bins sufficiently large to capture the major features in the data while ignoring fine details due to random sampling fluctuations. By considering the histogram as a piecewise-constant model of the probability density function from which n data points x_i were sampled the author derives an expression for the relative logarithmic posterior probability (RLP) for each bin number:

$$\begin{aligned} \mathrm{RLP} &= n\log N + N\log\Gamma\left(\frac{N}{2}\right) \\ &+ \log\Gamma\left(\frac{1}{2}\right) - \log\Gamma\left(n+\frac{N}{2}\right) \\ &+ \sum_{\lambda=1}^{N}\log\Gamma\left(n_\lambda+\frac{1}{2}\right) \quad . \end{aligned} \tag{2.9}$$

with N the number of bins and n_λ the value of the λth bin. To find the best number of bins M the posterior probability has to be maximized:

$$M = \arg\max_N\{\mathrm{RLP}\} \quad . \tag{2.10}$$

The best estimator for the bin value μ_λ and its variance σ_λ^2 given the bin values n_λ is deduced to be:

$$\mu_\lambda = \left(\frac{M}{v}\right)\left(\frac{n_\lambda + \frac{1}{2}}{n + \frac{M}{2}}\right) \tag{2.11}$$

and

$$\sigma_\lambda^2 = \left(\frac{M}{v}\right)^2 \left[\frac{\left(n_\lambda + \frac{1}{2}\right)\left(n - n_\lambda + \frac{M-1}{2}\right)}{\left(n + \frac{M}{2} + 1\right)\left(n + \frac{M}{2}\right)^2}\right] \quad . \tag{2.12}$$

with v the interval between the maximum and the minimum measurement value.
Knuth (2006) demonstrates in his study that these results outperform several other rules for choosing bin sizes, e.g. “Scott’s rule” or “Stone’s rule”.
I applied the described binning method to my data of Sgr A*. To make the flux density distribution comparable to the results by Dodds-Eden et al. (2011), which include the flux density of the star S17 due to a double aperture method, I added 3 mJy to the flux density of Sgr A*. I find a best bin number of $M = 32$. The dependence of the log posterior on the bin number is shown in Fig. 2.5. The best piecewise-constant model describing my sample is shown in Fig. 2.6 Unless stated otherwise the histograms in this thesis have been created using this method.

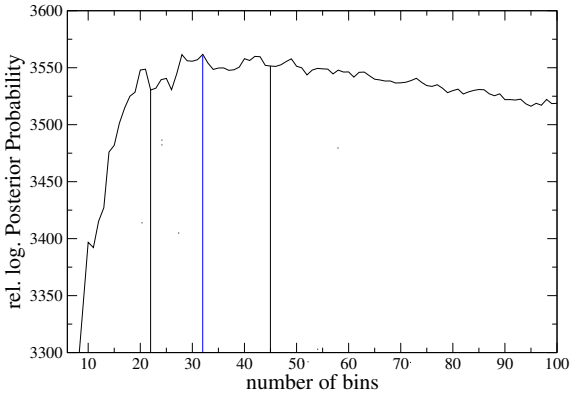

Fig. 2.5.: Optimal data based binning. I show the log posterior probability as a function of the number of bins. The maximum for the logarithmic flux density of Sgr A* is reached for 32 bins.

Additionally to the best histogram model obtained from Eq. (2.11) and Eq. (2.12) I over-plotted a graph of the distribution[5] proposed by Dodds-Eden et al. (2011) . It is obvious that my sample is more populated in the middle flux density range between 5 mJy and 15 mJy and shows a linear behavior between 4 mJy and 17 mJy, not showing any break or change of slope. That the shape of my histogram is not sensitive to the binning is shown in Appendix C, Fig. C.1, where I present histograms with 22 bins for the range of the observed flux density values (resulting in a comparable bin width

[5] slightly shifted on the x-axis to account for the proper offset due to the double aperture method used by Dodds-Eden et al. (2011), which before I included only roughly by adding 3 mJy, and to make it fit best the extremes of my histogram

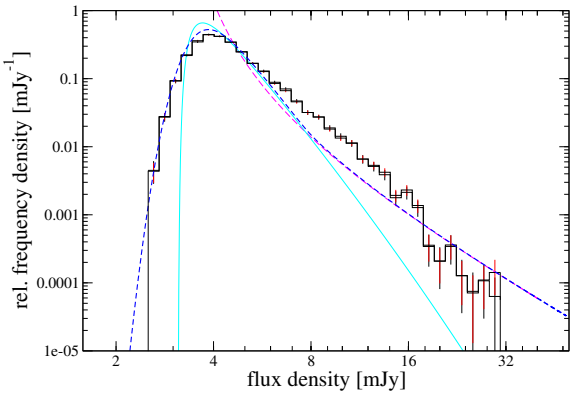

Fig. 2.6.: Best piecewise-constant probability density model for the flux densities of Sgr A*. The red error bars are the uncertainty of the bin height for the full amount of 10639 data points. The second bin height visible in some cases and the black error bars belong to the average histograms of 1000 datasets with 6774 data points (Dodds-Eden et al. 2011), generated by randomly removing points from my full dataset. The over-plotted cyan and magenta dashed lines show the log-normal distribution and the power-law distribution found in the analysis by Dodds-Eden et al. (2011), the blue the combined distribution of those components, convolved with a Gaussian with a flux density-dependent σ (compare Eqn. 2.3 to 2.6).

as used by Dodds-Eden et al. 2011) and 45 bins[6], both reproducing the linear trend. Rather than being a matter of representation, this difference is related to the different sample selection (10639 data points in this thesis in comparison to 6774 points in the case of Dodds-Eden et al. (2011)). To better understand the character of the selected subsample in Dodds-Eden et al. (2011) (their quality cut is based on the visual impression of the individual frame), I selected randomly 6774 points from my sample and generated in this way 1000 surrogate datasets, binned each dataset in a histogram with the same bin size as for my total sample, averaged the bin values over all surrogate sets, obtained an error from the standard deviation, and plotted the result as the second bin height (now with black error bars) in Fig. 2.6. One can clearly see that for most of the bins there is barely any difference, showing that a random influence cannot be responsible for the difference of both distributions. This test shows the robustness of the linear behavior of the histogram also in the case of smaller datasets under random selection. On the other hand, in my dataset I do not see the observation conditions to be correlated with the flux density states of Sgr A* (compare Fig. 2.2 and Fig. A.1 in Appendix A). In general the fraction of worse-than-average data should be represented in the uncertainties, and not simply eliminated, because otherwise errors might be underestimated due to an introduced bias, and I have to conclude here that probably the subsample used by Dodds-Eden et al. (2011) shows a severe selection effect.

The linear behavior in the log-log diagram points towards a power-law distribution $p \propto x^{-\alpha}$ as a possible description for all flux densities above ~ 4 mJy. The statistical

[6]The latter I show in an unweighted and in an integration time-weighted version.

significance of this visual impression is analyzed in the next section. I mention here that a power-law distribution is only showing a linear behavior in a log-log diagram if it is of the form:

$$p \propto (x - x_0)^{-\alpha}, \;\; x_0 = 0 \;\; . \tag{2.13}$$

Otherwise the logarithm of the probability density $\log(p)$ is only linear as a function of $\log(x)$ for big values of x:

$$\begin{aligned} \log(p) &= -\alpha \cdot \log(x - x_0) + \text{const} \\ &= -\alpha \cdot \log(x) - \alpha \cdot \log(1 - \frac{x_0}{x}) + \text{const} \; . \end{aligned} \tag{2.14}$$

This is the main reason why the distribution claimed by Dodds-Eden et al. (2011) shows a break: In this case the high flux density tail is described by a power-law with $x_0 \approx 0.8$ smJy, and this power-law does not show a linear behavior in the log-log diagram if plotted versus the sum of intrinsic flux density, background and flux density of S2. It starts to deviate from a linear behavior (it, so to say, "breaks") close to the transition value F_t of the total distribution (see Fig. 2.6, blue and magenta dashed line). Thus, even if we accept the selection of data points by Dodds-Eden et al. (2011), the visual impression of the necessity of introducing a break in the distribution is a feature of the data visualization, and the power-law actually is suited also in their case to describe quite well the data down to a flux density value of about 4 mJy. This means, even under the assumption that the data selection of Dodds-Eden et al. (2011) is valid, the discussion of a double state model for Sgr A* and its significance is very much depending on the plausibility of the assumption of a log-normal distribution for low intrinsic flux densities. I come back to this point in the next section.
The reason for the fact that we see the distribution developing linearly is a coincidental equality of $-x_0 = 3$ mJy for my data (see next section) and the flux density of S17 (≈ 3 mJy) which I added to the flux density of Sgr A* to make it comparable with the distribution proposed by Dodds-Eden et al. (2011).

2.2.2. Power-law representation of the intrinsic flux density distribution

I begin with a description of the instrumental effects and uncertainties of my photometry. Fig. 2.7 shows the flux density histograms of 10 stars (calibrators and comparison stars). As expected, the width of the distribution is decreasing with decreasing flux density of the source. To estimate the FWHM of the scatter of my photometry at a given flux density I fit Gaussian distributions to the flanks of the histograms. The σ

values of these fits as a function of the mean flux density is shown in Fig. 2.8. For my photometry I clearly find smaller uncertainties than Dodds-Eden et al. (2011) for their aperture photometry, very similar to their Starfinder photometry, or the photometry of Do et al. (2009). In contrast to both of these studies the functional dependency shows a clear flattening towards small flux densities and I can not confirm the dominance of photon noise (Dodds-Eden et al. 2011). I find a parabola to be a suited (phenomenological) description up to flux densities of 32 mJy. Actually the uncertainties in the flux density range between 0 and 10 mJy are more or less constant. This corresponds well to the visual impression that the variable AO-correction and its influence on the background contribution due to PSF halos of bright sources (halo noise, Fritz et al. 2010) as well as distortion effects and their interplay with the deconvolution are the dominant reasons for the uncertainties.

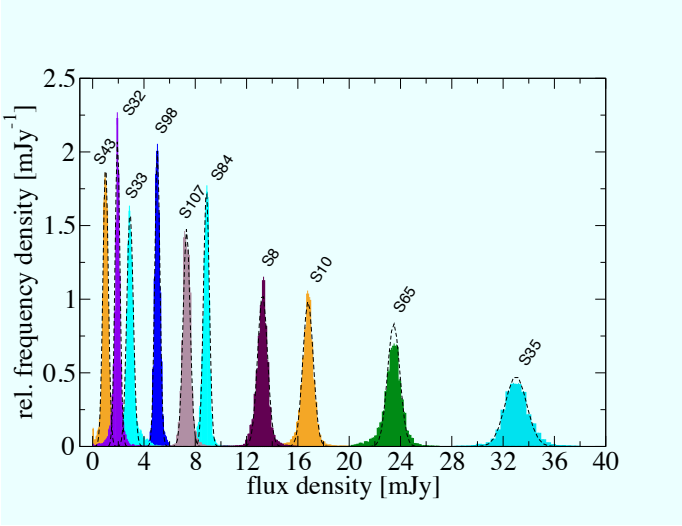

Fig. 2.7.: The normalized flux density histograms of ten calibration stars. The dashed curves are Gaussian fits to the flanks of the distribution, suppressing the broader tails of the distributions. This guarantees a proper measurement of the FWHM of the distributions.

The role of halo noise becomes evident when looking at the control apertures close to Sgr A* (Fig. 2.1, C-apertures). Their average flux density is clearly not zero, and the measurement values are scattered around the mean with a FWHM comparable to the width of all flux density distributions of the stars fainter than 10 mJy. The aperture west of Sgr A* shows a varying contribution of faint confusion on the level of a few tenth of a mJy (Fig. 2.9). The average flux density of these "empty" apertures is about 0.6 mJy.

In the following I investigate if a power-law distribution indeed is suited to describe my sample. I follow the strategy described in Clauset et al. (2007) for identifying power-law distributions and determining their parameters. The authors of this study point out that a least square regression to a histogram in log-log representation can generate

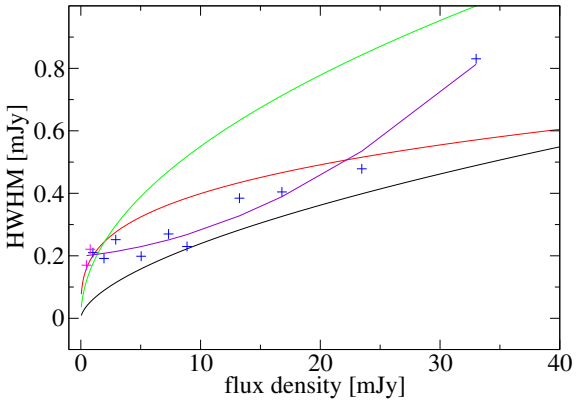

Fig. 2.8.: The measurement error as a function of flux density. The purple line is a quadratic fit to the measured σ-values of the calibration stars shown in Fig. 2.7 (blue crosses). The red line is the power-law dependency found by Do for their data, the green line and the black line the dependency found by Dodds-Eden et al. (2011) for their aperture photometry and their PSF-fitting photometry, respectively. The two magenta crosses represent the measured σ-values at the position of the C-apertures, compare Fig. 2.1.

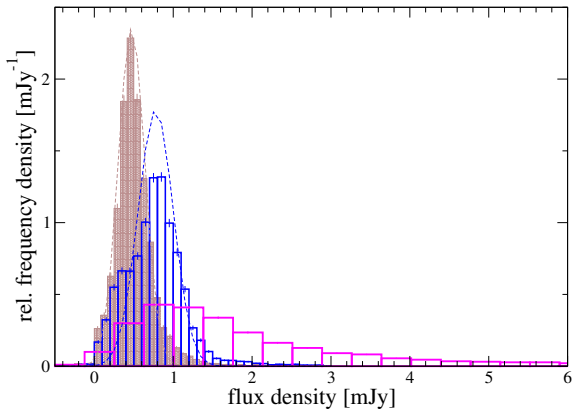

Fig. 2.9.: The flux density histograms of the two background (C-) apertures (blue, brown) close to Sgr A* in comparison to the flux distribution of Sgr A* (magenta). The dashed curves are Gaussian fits to the flankes of the distributions.

significant systematic errors, mainly due to the non-Gaussianity of the variation of the logarithmic bin height. Furthermore, binning the data in a histogram introduces further parameters corrupting standard goodness-of-fit estimators. The procedure described in the following overcomes this problems.

The probability density of a power-law distribution is defined as:

$$p(x) = \begin{cases} 0 & : \quad x \leq x_{\min} + x_0 \\ \frac{\alpha-1}{x_{\min}} \cdot \left(\frac{x-x_0}{x_{\min}}\right)^{-\alpha} & : \quad x > x_{\min} + x_0 \end{cases} , \tag{2.15}$$

with $x_{\min} + x_0$ the lowest value to which the data is power-law distributed, making the power-law normalizable with normalization factor $(\alpha - 1) \cdot x_{\min}^{\alpha-1}$. The corresponding cumulative distribution is given by:

$$P(x) = \begin{cases} 1 & : \quad x \leq x_{\min} + x_0 \\ \left(\frac{x-x_0}{x_{\min}}\right)^{1-\alpha} & : \quad x > x_{\min} + x_0 \end{cases} . \tag{2.16}$$

The steps for analyzing power-law distributed data are as follows (Clauset et al. 2007):

- Find estimators for $x_{\min}$ and x_0 and the maximum likelihood estimator for α. The maximum likelihood estimator for α given any value for $x_{\min}$ and x_0 is calculated using the equations

$$\alpha_{\text{est}} = 1 + n_{\text{tail}} \left[\sum_{i=1}^{n_{\text{tail}}} \ln \frac{x_i - x_0}{x_{\min}} \right]^{-1} , \quad x > x_{\min} + x_0 \tag{2.17}$$

$$\sigma_{\text{est}} = \frac{\alpha_{\text{est}} - 1}{\sqrt{n_{\text{tail}}}} , \tag{2.18}$$

  with n_{tail} the number of data points higher than $x_{\min} + x_0$. Estimators for $x_{\min}$ and x_0 are obtained by choosing $x_{\min}$ and x_0 in a way that makes the probability density and the best-fit power-law model (i.e. the power-law with α the maximum likelihood estimator) as similar as possible. The similarity is estimated by Kolmogorov-Smirnov (KS) statistics:

$$D = \max_{x \geq x_{\min} + x_0} |C(x) - P(x)| , \tag{2.19}$$

  with $P(x)$ the cumulative distribution of the best-fit power-law model and $C(x)$ the relative cumulative frequency of the empirical data sample. The parameter D has to be minimized. The error on $x_{\min}$ and x_0 can be found by a nonparametric "bootstrap" method, i.e. (given n empirical data points) by drawing a new set of n data points uniformly at random from the empirical data and determining the standard deviation of $x_{\min}$ and x_0 for these surrogate samples.

- Test for plausibility by calculating the goodness-of-fit between the empirical data and the power-law. The goodness-of-fit parameter q is defined as the fraction of synthetic data drawn from the best-fit probability model that has a worse KS statistics than the empirical data sample. Here it is important to obtain the KS value D for each synthetic sample in the same way as for the empirical data, i.e. the estimators for $x_{\min}$, x_0 and α have to be found for each synthetic sample individually and the KS values has to be calculated relative to the individual best-fit power-law. To ensure that the $x_{\min}$ values are determined under the same conditions like for the empirical data sample we have to make sure that the synthetic sample follows the empirical data sample distribution for the values smaller than

$x_{\min} + x_0$. This is realized by choosing with probability $1/n_{\text{tail}}$ a random number from the best-fit empirical power-law and with probability $1 - 1/n_{\text{tail}}$ a value from the empirical data below the $x_{\min} + x_0$ estimate (with n_{tail} the number of data points higher than $x_{\min} + x_0$). A q-value > 0.05, or more conservative > 0.1, makes the power-law model a plausible assumption.

With a simulation of 1000 surrogate samples for determining the errors of $x_{\min}$ and x_0 and 6000 synthetic samples for testing for plausibility I obtained the values:

$$\begin{aligned} x_0 &= (-2.94 \pm 0.1)\ \text{mJy} \\ x_{\min} &= (4.22 \pm 0.1)\ \text{mJy} \\ \alpha &= (4.215 \pm 0.05) \\ q &= 0.2 \qquad . \end{aligned} \tag{2.20}$$

A goodness-of-fit parameter $q = 0.2$ means that in a fifth of the cases a sample drawn from a power-law with parameters as in Eq. (2.20) will show deviations worse than my empirical sample, making the power-law description plausible for all flux densities higher than 4.2 mJy (note that the exact value of x-axis offset is $x_0 = -2.9$ mJy, close to the value found due to the linear appearance of the histogram in the log-log diagram). A diagram of the cumulative distribution function (CDF) of the best-fits power-law and the empirical relative cumulative frequency is shown in Fig. 2.10 . For a comparison I also over-plotted the CDF of the model proposed by Dodds-Eden et al. (2011) (restricted to flux density values higher than $x_{\min}$). Fig. 2.11 shows the value of the power-law slope α as a function of $x_{\min}$. As expected, the best $x_{\min}$ is close to the point where α starts to be constant for a range of $x_{\min}$ values (compare Fig. 3.3 in Clauset et al. 2007).

Here I have to mention that Eq. (2.17) only represents the maximum likelihood estimator for the power-law slope if the x_i are independent or at least uncorrelated, otherwise the estimator is biased. Now we know that for my sample the x_i are not uncorrelated, since the flux densities are occurring in "flares", it means in a time continuous development. This describes simply the fact that finding the flux density to be at a level of 15 mJy implies very low probability for a level of 5 mJy to be reached within e.g. the next 3 minutes. This predictable behavior disappears on longer timescales, and it is not possible anymore, knowing the flux density at a time t_0, to predict the flux density level e.g. 100 minutes later very reliably. This has been investigated by Meyer et al. (2009) in their analysis of the power spectral density discovering the longest correlation timescale to be at about 150 minutes. Here I am analyzing data covering about 15000 minutes (a hundred times longer than the timescale on which the correlation of

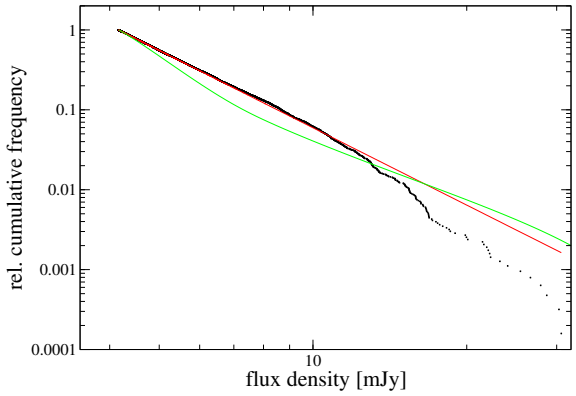

Fig. 2.10.: Estimation of the goodness parameter p by a Kolmogrov statistic. The value p is defined by the maximum difference of the measured CDF (black) with respect to the CDF of the best fitting power-law (red). In green I show the CDF of the model proposed by Dodds-Eden et al. (2011) (restricted to flux density values higher than x_{min}).

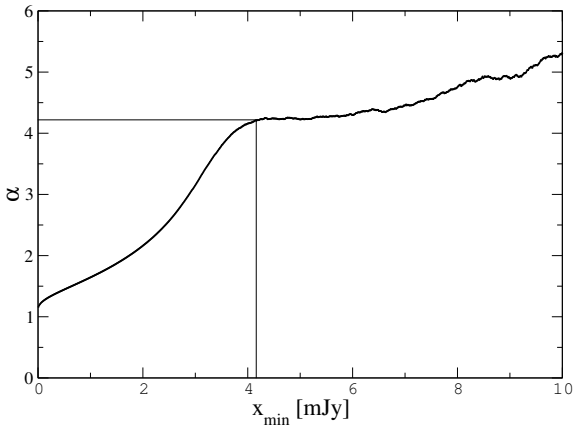

Fig. 2.11.: The scaling parameter α as a function of the value for x_{min} (compare Fig. 3.3 in Clauset et al. 2007).

the data vanishes according to Meyer et al. 2009) and spread over 7 years. This means to first order and because the estimator in Eq. (2.17) is most sensitive to data points close to x_{min} (where the histogram is most populated and the value of each bin can be considered to be fairly independent from the neighboring bins) the bias is negligible. This of course is different for the high flux density tail where the histogram is populated only with data points of the rare strong outbursts. Especially for my dataset all histogram bins at higher flux densities than about 17 mJy are populated only due to one very bright outburst. As we will see later, this is the reason why for higher flux densities the empirical cumulative distribution deviates more and more from the ideal CDF of the model and the statistics becomes incomplete. This effect is also visible in Fig. C.2 of Appendix C, where I show the ideal CDF, the empirical cumulative distribution and the cumulative distribution of some of the uncorrelated synthetic samples I generated for the estimation of the goodness parameter q. For high flux densities

many synthetic datasets show a more similar behavior with respect to their best-fit CDF than my empirical sample, even if their KS value D is worse. In this context it is important to notice that the synthetic samples with a worse KS statistics may differ significantly from the ideal CDF at lower flux density ranges which is not well visible in a log-log diagram (see Fig. C.2, Appendix C). These arguments also show that a χ^2-minimization fitting to the histogram is questionable, especially if the χ^2-values is used to establish the significance of a distribution break based on the highest, most correlated bins.

Up to this point we found a description for flux densities higher than $x_{\rm min}+x_0$. I can show that my data sample is consistent with a pure power-law describing the intrinsic flux density distribution under the influence of an instrument with limited resolution and sensitivity and that $x_{\rm min}+x_0$ can be interpreted as the detection limit of NACO for Sgr A* due to being embedded in extended flux and its confusion by faint unresolved stars. The argument is simple: if we weight the power law distribution for fluxes higher than $x_{\rm min}+x_0$ with a factor $n/n_{\rm tail}$, with $n_{\rm tail}$ the number of data points with values higher than $x_{\rm min}+x_0$, we can extend the power-law to smaller flux densities until its integral becomes unity:

$$x^*_{\rm min} = \left(\frac{n_{\rm tail}}{n}\right)^{\frac{1}{\alpha-1}} \cdot x_{\rm min} \quad . \tag{2.21}$$

In my case with the values of Eq. (2.20) I find $x^*_{\rm min} = 3.57 \pm 0.1$ mJy. Taking into account $x_0 = -2.94 \pm 0.1$ mJy, this power-law distribution shows a cut-off at $x^*_{\rm min}+x_0 = 0.63 \pm 0.15$ mJy , which is identical to the average flux density of the two background apertures close to Sgr A*. The measured distribution now can indeed be obtained by convolving the power-law distribution with a Gaussian distribution to account for the measurement error:

$$p_{\rm obs}(x) = \int p(z) \frac{1}{\sqrt{2\pi}\sigma^*} \exp\left[\frac{-(x-z)^2}{2\sigma^{*2}}\right] dz \ , \tag{2.22}$$

with σ^* the FWHM of the error distribution, which for my data sample can be considered constant up to ≈ 15 mJy (see Fig. 2.8), and $p(z)$ the power-law probability density as in Eq. (2.15). For higher values the histogram starts to be incomplete, and the bias due to the time correlation is dominating the statistical errors. The slope of the power-law is slightly changed by the convolution, but for values of σ^* of the magnitude of the observational errors this effect is within the errors of α.

By using again KS-statistics I find a constant value of $\sigma^* \approx 0.32$ mJy as a best fit to the histogram (see Fig. 2.12). This value is larger than the observed error $\sigma^* \approx 0.2$ mJy of isolated sources (see Fig. 2.8). The reason is that the photometry on Sgr A* for a large fraction of the data is influenced by the nearby star S17, and that I subtracted a

constant offset from epoch to epoch, for which it is difficult to find a realistic error. Both influences effectively broaden the expected distribution (which as a result is not Gaussian anymore in general, but somewhat less peaked). That this is not a disadvantage of the deconvolution method with respect to the double-aperture method preferred by Dodds-Eden et al. (2011) can be seen in Fig. 2.8. The error of the double aperture photometry for the low flux density range of Sgr A* (starting at flux densities > 3 mJy) is also in the range of > 0.3 mJy.

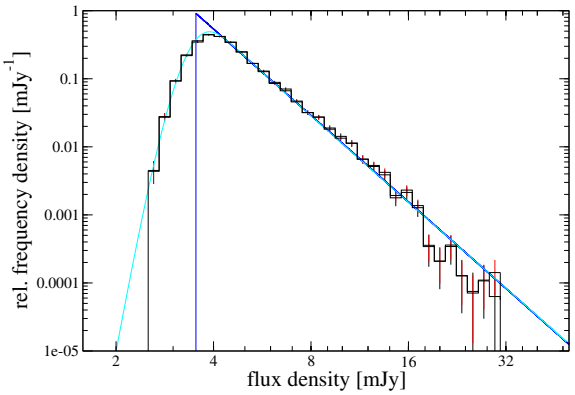

Fig. 2.12.: Flux density histogram like in Fig. 2.6. The blue line shows the extrapolation of the best power-law fit, the cyan line the power-law convolved with a Gaussian distribution with $\sigma =$ 0.32 mJy.

I conclude that it is not possible to verify the evidence of an *intrinsic* turnover (that could indicate the peaked shape of a log-normal distribution) based on the larger scatter of the low states of Sgr A* with respect to the typical error of an isolated source of this flux density. The difference of 0.1 mJy between the typical error of a faint source of 0.2 mJy and the error value for our best fit of 0.32 mJy is well within the uncertainties of our knowledge about the true error distribution at the position of Sgr A* as Fig. 2.9 demonstrates. Having no evidence for a log-normal distribution for low flux density values, the necessity of a break in the distribution to account for the highest flux densities vanishes, even if we accept the data selection of Dodds-Eden et al. (2011) and ignore the fact that all flux density bins higher than 17 mJy are populated due to one bright event only. Rather than a double state description I prefer a simple power-law with a slope of $\alpha = 4.2 \pm 0.1$ and an intrinsic pole at $x_{0,\mathrm{intr.}} = x_0 - \mathrm{backgr.} = -\mathrm{x}^*_{\mathrm{min}} = -3.57 \pm 0.1$ mJy. Since flux density is a positive quantity, this intrinsic power-law naturally breaks at $x^*_{\mathrm{min,intr.}} = x^*_{\mathrm{min}} + x_{0,\mathrm{intr.}} = 0$ mJy. The instrumental effects on the photometry are sufficiently described by a Gaussian distribution centered around the background value of 0.6 ± 0.1 mJy with a constant $\sigma = 0.32$ mJy. This instrumental effect leads to a detection limit, which here is defined as the limit up to which a reliable photometry is not possible, of $\sim 0.7 \pm 0.16$ mJy intrinsically, and $\sim 1.3 \pm 0.15$ mJy for the actual measurements which include the back-

ground flux density of 0.63 ± 0.15 mJy. With the power-law model we find a mean value for the flux density of $\langle x \rangle_{\text{intr.}} = 0.9 \pm 0.15$ mJy (corrected for the background), or $\langle x \rangle_{\text{obs.}} = 1.5 \pm 0.1$ mJy (including the background flux density). This shows that, assuming we can extrapolate the power-law to smaller flux densities below the detection limit, we find the average flux density to be very close to the detection limit, indicating a severe limitation of the knowledge about the variability of Sgr A* we are able to infer from my data. The relation of x_0, x_{min}, x^*_{min} and the background flux density is schematically shown in Fig. 2.13.

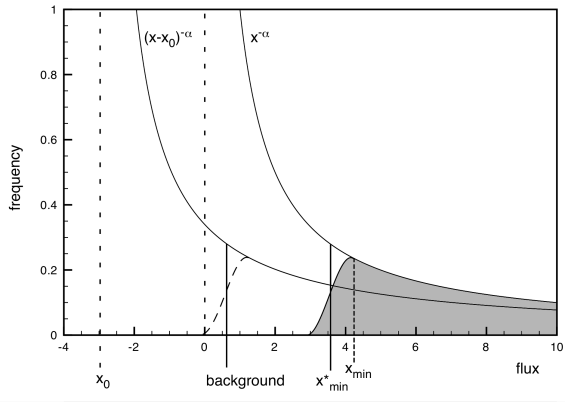

Fig. 2.13.: Schematic view of the power-law flux density distribution and the parameters x_{min}, x^*_{min}, x_0 and the background flux density (y-axis in arbitrary units, x-axis in mJy). I show the measured flux density distribution (grey area) after adding 2.94 mJy to account for x_0, the pole of the measured non-shifted power-law (which belongs to the non-shifted distribution indicated by the long-dashed line), and the intrinsic distribution with and without correction for x_0 (described by the continuous lines $\propto x^{-\alpha}$ and $\propto (x - x_0)^{-\alpha}$, respectively). As in Eq. (2.15), x_{min} is the minimum flux density down to which the shifted measured distribution is a power-law, and x^*_{min} is the minimum flux density obtained by an extrapolation of the power-law toward lower values, assuming the distribution below x_{min} to be dominated by instrumental effects. Therefore, x^*_{min} represents the *intrinsic* minimum flux density in the case of the x_0-shifted distribution. For the case of the non-shifted distribution the intrinsic minimum is represented by $x^*_{\text{min}} + x_0$, which equals the background flux density within my uncertainties. Thus, the intrinsic minimum $x^*_{\text{min,intr.}} = x^*_{\text{min}} + x_0 - \text{backgr.}$ (now additionally corrected for the background) equals zero.

Of course I cannot *prove* that the flux density distribution is a strict power-law distribution. I only can show that the observable intrinsic flux densities can well be described by this model. This assumption is simpler and needs less parameters than the broken distribution proposed by Dodds-Eden et al. (2011). Nevertheless, it might well be that the real distribution shows some structure at flux densities below the detection limit. In particular it might even follow a log-normal distribution (with a high multiplicative standard deviation to account for the linear appearance in the log-log plot). The log-normal distribution used in the model of Dodds-Eden et al. (2011) and an evidence for a break in the distribution at an observable flux density level, however, can be ruled out.

2.3. Time series analysis

In this section I investigate the nature of the already mentioned time correlation of the flux density measurements. In a more formal description: assuming that all measurements are samples of the very same random process, and starting with the idea that this random process is (weakly) stationary (for which the impression of a stable mean and variance is indicative), I consider the flux density distribution of section 2.2 as the marginal probability distribution of the random process. Now I want to find a characterization of the joint probability distribution. Whereas in general 'red noise' light curves only can be considered as weakly non-stationary, the (weak) stationarity for the underlying random process is a consequence of the PSD break found by Meyer et al. (2009) that is far shorter than the covered time period of 15000 minutes.

A first, very simple approach for characterizing the time behavior of the variability is the following: let us associate the average sampling of the concatenated light curve of ~ 1.2 minutes to every data point. In this way we can relate the total time the source spent in the range of a given flux density bin to the total time covered by observations (~ 15000 minutes), and we get a rough estimator for the fraction of time the source spends at that flux density. For a more detailed analysis we have to use standard time series analysis tools, like periodograms as estimators for the power spectral density (PSD) of the process, Lomb-Scarle periodograms, the autocorrelation function or the structure function (Scargle 1982; Priestley 1982; Simonetti et al. 1985). As Meyer et al. (2009) point out, the given window function (covering $\sim 3.6 \cdot 10^6$ min with a coverage fraction of only $\sim 0.4\%$) makes standard Fourier transform techniques unsuitable (see Fig. 2.3). Similarly the Lomb-Scargle periodogram, generally suited as a PSD estimator for non-equally sampled data, is based on the average sampling, which in this case is > 3000 min. Do et al. (2009) used the approach of comparing and averaging the Lomb-Scargle periodograms of data subsets with similar length and sampling to access the PSD of the higher frequencies. In our case this approach again would introduce selection statistics, and I decided to generally follow the method presented by Meyer et al. (2009), a Monte Carlo (MC) approach, similar to the PSRESP method by Uttley et al. (2002). Dodds-Eden et al. (2011) mention that the MC simulation approach used in Do et al. (2009) and Meyer et al. (2009) are based on a comparison sample with a flux density distribution that is Gaussian, and in particular allows negative values, questioning the validity of the method. In the following I overcome these concerns by developing an algorithm that allows me to simulate time series with the flux density distribution we observe.

2.3.1. RMS-flux density relation

For the study of X-ray binary variability (linear) rms-flux relations represent an important piece of information. The rms (root mean square) - as it is used here - is a measure for the magnitude of the variability of the light curve. Following Uttley et al. (2005) the absolute rms amplitude of variability $\sigma_{\rm rms}$ of a time series of n data points, x_i, is defined as as:

$$\sigma_{\rm rms} = \sqrt{\frac{1}{n-1}\sum_{i=1}^{n}(x_i - \langle x \rangle)^2}\,. \tag{2.23}$$

In the case of weakly non-stationary segments of a stationary light curve $\sigma_{\rm rms}$ varies randomly about a mean value. Under certain circumstances this mean scales with the average flux density of the segment $\langle x \rangle$. This is called a "rms-flux relation".

In particular, Uttley et al. (2005) related the rms-flux relation, which could be observed on all timescales for some of their sources, to a formally non-linear, in their case exponential statistical model that convincingly reproduces the behavior of the observed X-ray light curves. With this model the authors rule out additive (shot-noise) models or self-organized criticality as the responsible processes and conclude that the variability processes must be multiplicative. Because the rms-flux relation is stable for all spectral states of the Black Hole X-ray Binary System Cyg X-1 independent of its PSD shape it is believed to be a more fundamental property of the variability than the PSD shape.

I report here the discovery of the rms-flux relation for Sgr A* in the NIR. Following the description of the timescale dependent rms analysis in Uttley et al. (2005) and using time series IDL-codes written by S.Vaughan I estimated dependence of the rms on the flux density over a frequency range from the average Nyquist-frequency of $\sim 0.5\,\mathrm{min}^{-1}$ to $0.06\,\mathrm{min}^{-1}$ (corresponding to timescales of 2 to 16 minutes) for data sections with a length of 24 min. The algorithm works as follows: I divided the light curves in segments of 24 minutes, took the average as a flux density estimate, and determined the PSD of this section. I then obtained the rms for timescales between 2 and 16 minutes by taking the square root of the integral of the PSD over the corresponding frequency range.

The dominant timescale of the PSD is of the order of a few hundred minutes (150 min, Meyer et al. 2009). Realizations of the random process that are not significantly longer than this timescale are weakly non-stationary. So for a given mean flux density the rms-values of my data sections of 24 minutes are significantly scattered around their average value. To account for this I re-binned the obtained rms-values into flux density-bins with width $\Delta x = 1.2$ mJy. The result is shown in Fig. 2.14. I find a clear, in the first approximation linear rms-flux dependence.

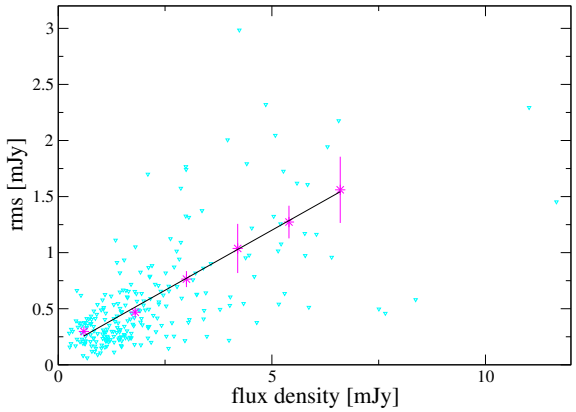

Fig. 2.14.: Relation between the rms (on timescales of 2 to 16 min) and average flux density for data segments of 24 min (blues points). In red the re-binned data, in black the best linear fit.

2.3.2. Simulating light curves

A simple argument for the plausibility of a rms-flux relation is given by Uttley et al. (2005). The authors point out that a product of two sinusoidal variations with two well separated frequencies, where the lower 'modulates' the amplitude of the higher frequency, would show a linear rms-flux relation. In contrast to this, a linear and Gaussian random process would not show any correlation between flux density and rms. Because the rms-flux relation in their case holds for all observed timescales, the authors choose the ansatz:

$$x(t) = \prod_{i=1}^{\infty} [1 + A_i \sin(2\pi \nu_i t + \phi_i)] \quad , \tag{2.24}$$

with ϕ_i uncorrelated random phases and A_i uncorrelated random amplitudes. For this multiplicative sine model the authors then can show that x_t under general conditions is log-normal distributed, that it can be obtained from a Gaussian linear random process $l(t)$ by the transform $x_t \approx \exp[l(t)]$, and that for this kind of transform one indeed can derive the rms-flux relation to be a linear function.

Whereas the rms-flux relation often is considered as indicative for a multiplicative process being at work, it actually can be shown (Uttley et al. 2005 and references therein) that for every non-Gaussian, skewed distribution the sample mean and variance are correlated (the distribution is heteroskedastic). Thus, another, less favored possibility to explain the rms-flux relation and the skewness of the flux density distribution is simply a non-Gaussian linear process. It is because of this reason that one has to speak of a *formally* non-linear description, and without the modeling in the framework of a concrete physical model it must remain unclear, whether the non-linearity has a physical meaning rather than being the property of the mathematical description.

In this case we do not know, if the observed rms-flux relation also is valid for a bigger

range of time and flux density scales. As mentioned in section 2.2, we only detect the variability of Sgr A* about half of the time with reliable photometric accuracy. Furthermore, we have to use data segments of a length comparable to or shorter than the dominant timescale. Additionally, the segments have to be comparably short with respect to the typical data length (about 130 minutes in average) to provide a sufficiently big number of rms-flux data pairs. On the other hand, the segments should be long enough to contain enough data points for a reliable rms estimation. In the case of my data these constraints only allow an investigation of the presented timescales.
The flux density distribution does not seem to be log-normal distributed (although this cannot be excluded with absolute certainty). Some conditions for the derivation of the log-normal behavior in Uttley et al. (2005) might be violated in our case. One of the conditions in the derivation (under which the central limit theorem is applicable) is PSD which is almost constant over a wide frequency range. Since we clearly see a dominant timescale in our data, this condition is not well fulfilled, and from this perspective I would not necessarily expect the flux densities to be log-normal distributed, even if the multiplicative approach of Eq. (2.24) can be applied to this case. It is also possible that for this case Eq. (2.24) is not a good representation of the random process, either because we only have a finite product, or the factors are not sinusoidal.
In Uttley et al. (2005) the authors use Eq. (2.24) to show the plausibility of the multiplicative approach in the context of an rms-flux relation and a log-normal distribution, deducing an exponential transform of a linear, Gaussian random process as a good approximation of their random process. In order to find a statistical description in my case I follow another approach: I ask which is the transform that has to be applied to a Gaussian distributed random variable to obtain a random variable that is power law distributed with the parameters found in section 2.2.2. I then assume that I can apply this transform to a linear, Gaussian process to find a description of the observed process. This actually is a standard method for generating Fourier transform based surrogate data with a non-linear appearance (see Theiler et al. 1992).
The statistical flux density model I described in section 2.2.2 has a simple analytic form. This allows us to deduce an analytic transform

$$x_t = T(y_t) \quad , \tag{2.25}$$

with y_t a Gaussian, linear process with unity variance, T the transform, and x_t a power-law distributed process. In the following I describe how we find this transform.
Let be y a random variable with Gaussian probability density p_y of zero mean and unit variance:

$$p_y(y) = \frac{1}{\sqrt{2\pi}} \exp\left(\frac{-y^2}{2}\right) \tag{2.26}$$

and x a random variable with a power-law probability density p_x:

$$p_x(x) = \begin{cases} 0 & : \quad x \leq c \\ \frac{\alpha-1}{c} \cdot \left(\frac{x}{c}\right)^{-\alpha} & : \quad x > c \end{cases} , \tag{2.27}$$

with $\alpha > 1$. We are looking for a transformation $x = T(y)$ such that p_y transforms to p_x. For such a transform the probability to find a value in the immediate surrounding of y has to equal the probability to find a value in the immediate surrounding of the corresponding $x = T(y)$:

$$p_y(y)dy = p_y\left[T^{-1}(x)\right] \frac{d\left[T^{-1}(x)\right]}{dx} dx \stackrel{!}{=} p_x(x)dx \ , \tag{2.28}$$

or

$$p_x(x) = p_y\left[T^{-1}(x)\right] \frac{d\left[T^{-1}(x)\right]}{dx} \ . \tag{2.29}$$

To solve this equation I use a normalization argument:

$$\int_{-\infty}^{y} p_y(y')dy' = \int_{c}^{x} p_x(x')dx' \ . \tag{2.30}$$

With

$$\int_{c}^{\infty} x^{-\alpha} dx = \frac{1}{(\alpha-1)} \cdot c^{1-\alpha} \tag{2.31}$$

Eq. (2.30) can be reduced to

$$\frac{1}{2}\left[\mathrm{erf}\left(\frac{y}{\sqrt{2}}\right) + 1\right] = 1 - \left(\frac{x}{c}\right)^{(1-\alpha)} \ , \tag{2.32}$$

with $\mathrm{erf}(y)$ the Gaussian error function. This can be solved for x:

$$x = c \cdot \left\{\frac{1}{2}\left[1 + \mathrm{erf}\left(\frac{y}{\sqrt{2}}\right)\right]\right\}^{\frac{1}{(1-\alpha)}} = T(y) \ . \tag{2.33}$$

To reproduce light curves with an intrinsic power-law distribution of the flux densities on top of a constant background flux density as discussed in section 2.2.2 we have to replace c with x^*_{min} and subtract x_0:

$$T(y_t) = x^*_{\mathrm{min}} \cdot \left\{\frac{1}{2}\left[1 + \mathrm{erf}\left(\frac{y_t}{\sqrt{2}}\right)\right]\right\}^{\frac{1}{(1-\alpha)}} - x_0 \ , \tag{2.34}$$

with x^*_{min} defined in Eq. (2.21), x_0 as in Eq. (2.20), and α the slope of the power-law. With this transform I am able to generate surrogate light curves (i.e. single realizations of the underlying process) for every input power spectral density (PSD) with the following algorithm:

- Generate a Gaussian, linear light curve following the method by Timmer & Koenig (1995). This includes drawing Fourier coefficients for each frequency from a Gaussian distribution with a variance proportional to the value of the PSD at that frequency, and Fourier transforming to time domain.
- Normalize the obtained Gaussian process to a variance of unity. Optionally re-sample the equally spaced data to the time support of the observed data.
- Transform the light curve according to Eq. (2.25) and Eq. (2.34).
- Add an independently drawn quantity (e.g. Gaussian) for each time point to account for the white noise contribution of the measurement.

As I show in the next section, the obtained surrogate data does not only exhibit the observed flux density distribution by construction, but also the time behavior of the light curves of Sgr A*. Applied to a linear Gaussian light curve with the PSDs discussed in section 2.3.3 I obtained light curves of an typical appearance as shown in Fig. 2.18 and 2.19. The non-linearity introduced by a transformation as described here is static. This means that for each time point we apply the same transform, and the non-linearity is only in the amplitude distribution of the observed quantity and not in its dynamics (see Theiler et al. 1992). This can be illustrated with light curves generated with a double broken power-law PSD of the form:

$$S(f_j) = \begin{cases} f_a^{-\alpha_2+\alpha_1} f_j^{-\alpha_1} & : \quad f_j < f_a \\ f_j^{-\alpha_2} & : \quad f_a \leq f_j < f_b \\ f_b^{-\alpha_2+\alpha_3} f_j^{-\alpha_3} & : \quad f_b \leq f_j \end{cases} , \tag{2.35}$$

with $f_a < f_b$ the break frequencies, and $\alpha_1 < \alpha_2 < \alpha_3$ the power-law slopes.
With the algorithm described above I generated 100 equally sampled light curves with a sampling of 0.1 min and a length of 50000 minutes. For each surrogate light curve I calculated the periodogram as an estimator of the PSD after transformation according to:

$$\begin{aligned} \mathrm{Per(f_j)} &= |\mathrm{DFT(f_j)}|^2 \\ &\sim \left[\sum_{i=1}^{n} x_i \cos(2\pi f_j t_i)\right]^2 \\ &+ \left[\sum_{i=1}^{n} x_i \sin(2\pi f_j t_i)\right]^2 , \end{aligned} \tag{2.36}$$

with DFT the discrete Fourier transform. For a review of common conventions of normalization see Vaughan et al. (2003). Here we want to compare the shape of the

PSD, and due to the normalization step applied to the Gaussian linear light curve only relative power is of importance. Because the Fourier based periodogram is not a consistent estimator of the PSD (i.e. for a single realization its standard variation is equal to the mean values at each frequency, irrespective of number of data points) some kind of averaging has to be applied (Timmer & Koenig 1995, Vaughan et al. 2003), and I averaged over the 100 surrogate sets I generated.
A comparison of the input and the output PSD is shown in Fig. 2.15. In the first approximation and with the exception of the high-frequency part (that is dominated by the white noise contribution) and a calibration factor the PSD is invariant under the transformation.

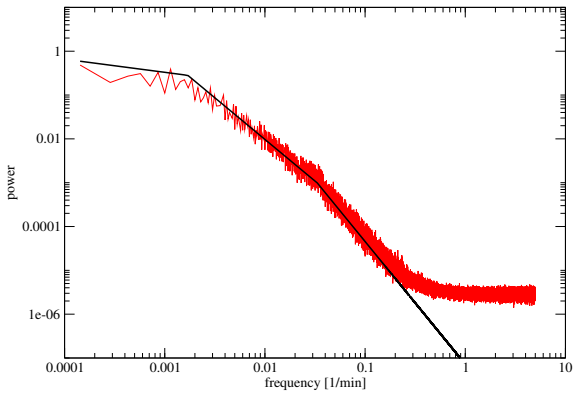

Fig. 2.15.: The PSD under transformation according to Eq. (2.34). In black a double broken power-law input PSD, in red the output PSD after applying the transform. The power is given in arbitrary units.

2.3.3. The structure function and the PSD

Now I can investigate the time correlation within the random process. One way to do this is an investigation of the structure function, a running variance method that measures the mean value of the flux density variance for a given time separation τ (Simonetti et al. 1985; Do et al. 2009):

$$V(\tau) = \langle [x(t+\tau) - x(t)]^2 \rangle \ . \tag{2.37}$$

The structure function of my data sample (on its true time support) is shown in Fig. 2.16. I only considered time separations with more than 300 flux density pairs. Clearly the night-day gap between ~ 360 min and ~ 1200 min (A) and a section with low density of data points beginning at ~ 7500 min due to the typical length of the observation runs (B) are visible. The structure function shows the expected tendency for a flat behavior at small τ-values (white noise of the measurement), a steeply increasing, power-law

like middle section, and a flat behavior at longer timescales (Meyer et al. 2009). Interestingly the structure function also shows a number of features starting at ~ 25 min, which give the impression of a second break at this timescale. This timescale is of particular interest in the discussion of the role of physical processes close to the innermost stable orbit.

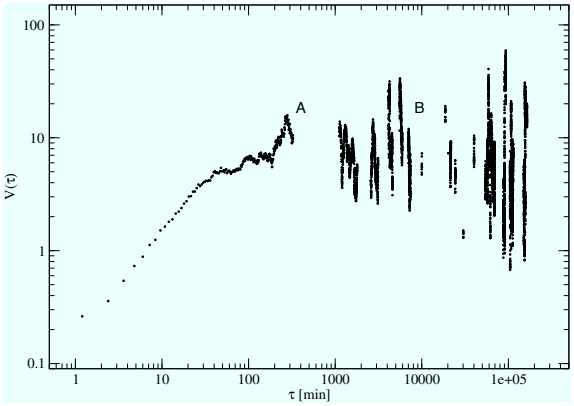

Fig. 2.16.: The structure function of the observed data sample (time binning 1.2 min).

The analysis of the structure function is problematic. A comprehensive study about the use and the caveats of structure function methods can be found in Emmanoulopoulos et al. (2010). The authors point out that spurious breaks may occur for many realizations of random processes with even featureless PSDs, only reflecting the interplay of the PSD of the underlying random process and the data length. This can be easily understood, because timescales much longer than the data length can define the sample average around which the shorter timescales (smaller than the data length) might vary with similar, repeated fluctuations (see Fig. 4 in Emmanoulopoulos et al. 2010). This makes the true average of the underlying random process an essential piece of information, which in our case can be easily inferred. Although we do not know the true distribution below the detection limit, the average of the flux densities above this limit (2.3 ± 0.1 mJy including the background) is an upper limit to the true average value. Because the true average has to be greater than zero, its uncertainty is small in comparison to the values reached by many outbursts. Thus, the main feature of the structure function, the flattening towards long timescales, is indeed an intrinsic feature. This also is supported by the fact that Meyer et al. (2009) find zero percentage of acceptance for single slope power-law PSDs.

Other concerns of Emmanoulopoulos et al. (2010) are more important for our case: the structure function values for different timescales are not independent and not Gaussian, and for broken intrinsic PSFs the break timescale can occur at systematically lower values, making usual fitting algorithms and their error estimation unsuited. Furthermore, the authors show that one may expect plenty of artificial features in the case of non-

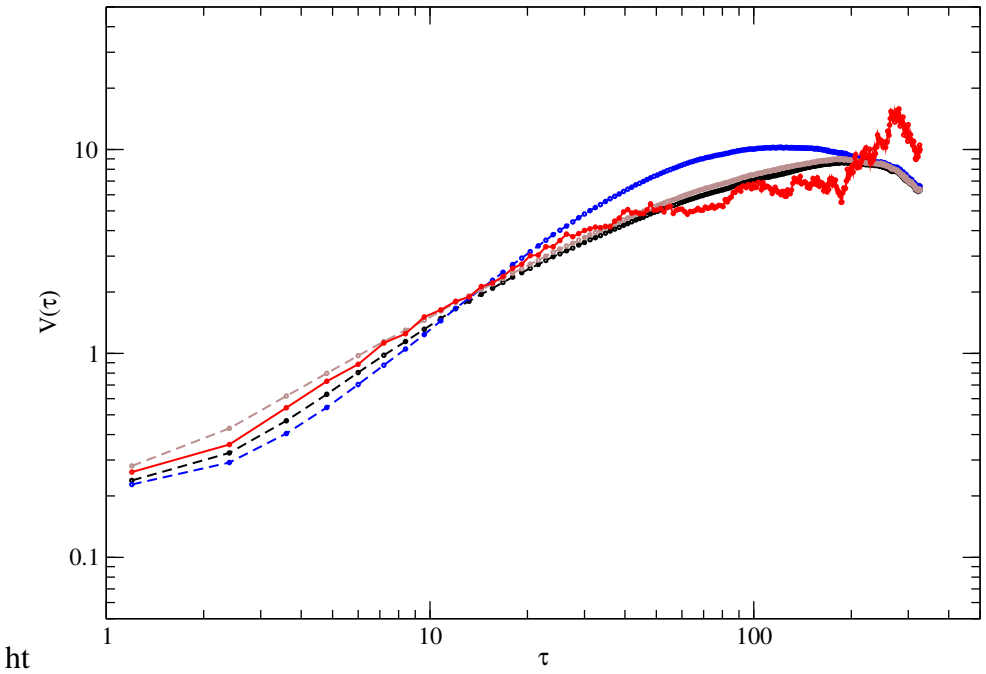

Fig. 2.17.: Comparison of the observed structure function (red) and the structure functions of the best fitting single broken PSD (brown, 92% of acceptance), the best fitting double broken PSD (black, 94%), and a single broken PSD with 68% of acceptance (break at 210 min, blue). For details see text.

equally spaced data. While the latter concern indeed makes it necessary to carefully investigate the discussed features of our structure function at shorter timescales (compare the structure function for dense and sparse sampling in Fig. 12 of Emmanoulopoulos et al. 2010), the former can be overcome by the procedure introduced by Meyer et al. (2009).

The steps are as follows:

- Starting with a double broken power-law PSD of the form of Eq. (2.35) we generate 5000 light curves (as described above) for a number of combinations of the parameters (α_1, α_2, α_3, f_a, f_b). Each light curve has a length of $4 \cdot 10^6$ min and a sampling of 1 min and is re-sampled to the time support of the observed data.

- We calculate the structure function for each surrogate light curve in the same way as for the observed data sample.

- We define a goodness parameter for the comparison of the single structure function with the "average" structure function for each set of parameters. The probability of acceptance of a parameter set is defined as the percentage of the 5000 surrogate light curves that have a worse goodness-value with respect to the "average" structure function than the observed sample.

Meyer et al. (2009) used standard χ^2-values and an arithmetic average of the structure functions for the estimation of the goodness of the individual fit. To account for a possible non-Gaussian distribution of the structure function values for a given separation τ, I prefer a modified χ^2 estimation (Emmanoulopoulos et al. 2010):

$$\chi^2_{ps} = \sum_k \left(\frac{\langle \log[V(\tau_k)] \rangle - \log[V(\tau_k)]}{\sigma_k} \right)^2 \tag{2.38}$$

with σ_k the standard variation of $\log[V(\tau_k)]$. I use the logarithm to make the skewed distribution of each structure function value more "symmetric". In particular the difference of the mean and the most probable value, which is a consequence of the skewness, is reduced making the modified χ^2 a measure of the distance to the most probable rather than to the average structure function, as it is necessary for a maximum likelihood approach.

Since f_a corresponds to much shorter timescales than the overall length of the observed light curve ($3.6 \cdot 10^6$ min), and the power-law slope of the PSD at small frequencies is very flat (~ -0.3, Meyer et al. 2009), it is not necessary to produce much longer light curves to avoid red-noise leakage. Also a higher sampling rate and a subsequent smoothing in order to simulate the effect of the detector integration does not change the results of my simulation.

I first explored the parameter space by manual fitting and then defined the range of parameters, for which I set up the Monte Carlo simulation. For the structure function I used time separation bins of 1.2 min and concentrated on the first 287 points (up to a time separation of ~ 340 min) for the estimation of the acceptance values, using the constant slope of $\alpha_1 = 0.3$ found by Meyer et al. (2009) for the long timescales. The well fitting combinations are constrained by the fact that the normalization step makes the choice of e.g. α_3 dependent on the choice of f_b. Additionally, the differences between f_a and f_b should correspond to a timescale that still can be measured within a typical observation length (~ 130 min). Finally, the difference between α_2 and α_3 should still be big enough to differentiate the double broken PSD model from a single broken model. For a double broken power-law PSD I tested all combinations of the following parameter set:

$$\begin{aligned} \alpha_1 &= 0.3 \\ \alpha_2 &= 1.8/1.9/2.0 \\ \alpha_3 &= 2.5/2.8/3.3 \\ f_a &= 0.001/0.0017/0.0025 \\ f_b &= 0.0133/0.0333/0.0533 \ , \end{aligned} \tag{2.39}$$

with f_a and f_b given in min^{-1} , and to obtain a finer grid, additionally all combinations of

$$\begin{aligned} \alpha_1 &= 0.3 \\ \alpha_2 &= 1.85/1.9/1.95 \\ \alpha_3 &= 2.65/2.8/3.05 \\ f_a &= 0.0014/0.0017/0.002 \\ f_b &= 0.0233/0.0333/0.0433 \ . \end{aligned} \tag{2.40}$$

For a single broken power-law PSD I tested the conbinations of:

$$\begin{aligned} \alpha_1 &= 0.3 \\ \alpha_2 &= 2.0/2.3/2.6/2.9 \\ f_a &= 0.002/0.004/0.008/0.01 \ . \end{aligned} \tag{2.41}$$

I find the highest probability of acceptance of 96% for a double broken power-law with slopes of $\alpha_2 = 1.9$ and $\alpha_3 = 3.3$ and break timescales at 20 min and 590 min, respectively. Several combinations in the ranges of $\alpha_2 = 1.8-2.0$, $\alpha_3 = 2.5-3.3$ for the slopes, and $f_b = 20-40$ min and $f_a = 500-700$ min for the break timescales reach acceptance values above 90%. Considering the typical statistical fluctuations of the acceptance values of about 2 percentage points they can be considered as equivalent. In comparison the single broken PSD models with a break in the range of the 90% confidence interval of Meyer et al. (2009) (154^{+124}_{-87} min) only reach 75% at maximum. On the other hand, the high acceptance values are typically reached for values of $f_b = 0.0017/0.002$ and $\alpha_2 = 1.8-2.0$, independent of the values for f_a and α_3. Indeed, a single broken power-law PSD with $\alpha_2 = 2.0$ and $f_a = 0.002$ (500 min) also reaches an acceptance level of 92%, making the question if the true PSD has more structure than a single break, undecidable on the base of the presented dataset. The behavior of all parameter sets discussed here for timescales longer than 500 min (not depicted here) match the measured structure function.

In Fig. 2.17 I show the most probable structure function estimated from 5000 surrogate datasets for a high probability double broken PSD model with break timescales at 30 and 590 min (94% of acceptance) and the highly probable single broken PSD model (92% of acceptance, break at 500 min). Both are almost identical. Additionally, I present the most probable structure function for a single broken PSD model with a lower break timescale at 210 min and a probability of acceptance of 68%. We can clearly see that all three structure functions show a flattening towards longer timescales

beginning at about 25 min, independent of their dominant timescale or the shape of the PSD. This shows that the features in the observed structure function starting at ~ 25 min are dominated by the influence of the window function of the dataset and cannot be interpreted as intrinsic.

Light curves generated with the double broken PSD with 92% acceptance and with the single broken PSD with 68% acceptance are shown in Fig. 2.18 and Fig. 2.19. Fig. 2.20 shows the comparison of long light curves for the high probability single and double broken cases, demonstrating their similarity on long timescales. Also on shorter timescales the high probability single broken models generate light curves which are not obviously different from the high probability double broken cases. It is plausible that a difference that is difficult to see in time continuous data can not be significant in data with a sparse time coverage. Note that due to the dominant timescale in both light curves of about 500-600 min there are time intervals (sometimes even more than a day) where the brighter flares start from higher flux density levels than the normal minimum level. In the case of a sparse data coverage this can lead to an misinterpretation of these minimum level differences as variability on long timescales, and from this point of view the interpretation of these differences as variations on timescales of weeks and month given in Dodds-Eden et al. (2011) is not the only possible explanation.

I have to make two comments on error bars and confidence levels: First, there is no good method to provide error bars for the observed structure function, because it would require knowledge about the true PSD and its interaction with the window function of the observation. Additionally, the distribution of the single point in the structure function can be very skewed and it is questionable whether e.g. a standard deviation over the MC light curves can be established as a good error estimate. Secondly, the break timescale of 500 min found lies outside the 90% confidence interval of Meyer et al. (2009), while their value is well within my 90% confidence interval.

There are three reasons why the errors in Meyer et al. (2009) possibly are underestimated: the authors compared the observed structure function with Gaussian surrogate data, they used a standard χ^2 values for comparing the structure functions, and they simulated their 10000 structure functions from combinations of 100 MC light curves for the long and 100 light curves for the short timescales, introducing a statistical coherence that does not reflect the true statistics. Another possibility of course might be that the process is not absolutely stationary and that the dominant timescale is not time invariant. On the other hand, in contrast to my sample Meyer et al. (2009) also consider the combined, long light curves of VLT and KECK observations, accessing the timescale of 500 min, which is not represented in my sample, and it might well be that the information on the true break timescale is represented better in the analysis of Meyer et al. (2009) than in my data sample presented here.

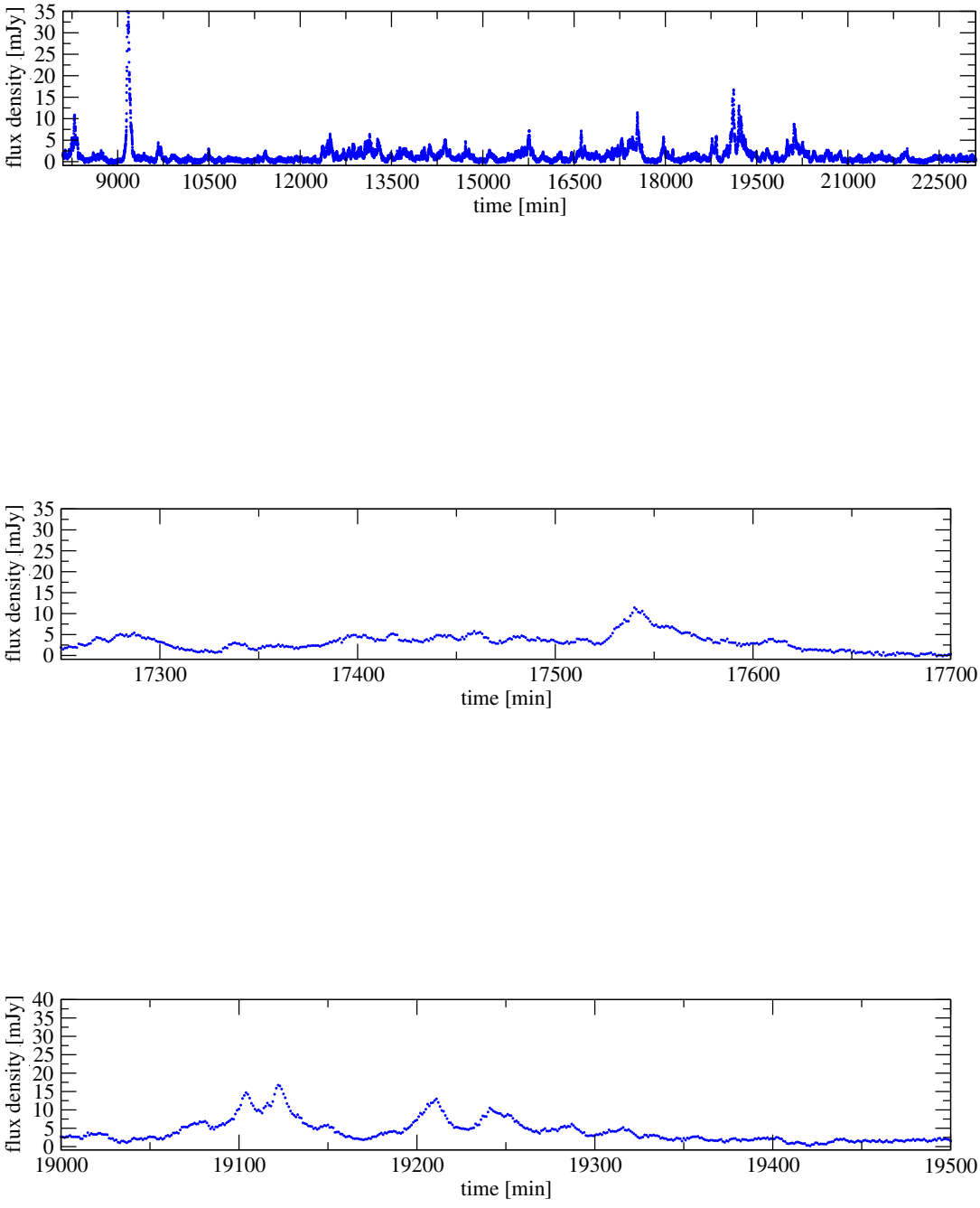

Fig. 2.18.: Simulated lightcurves taken from a $4 \cdot 10^6$ min time series created with the best double-broken power-law PSD. The upper panel shows typical 15000 min, the lower panels 500 min closeups with lower and higher flux density levels. Light curves created with the best single broken PSD show to a first order the same behavior as the presented case (compare Fig. 2.20).

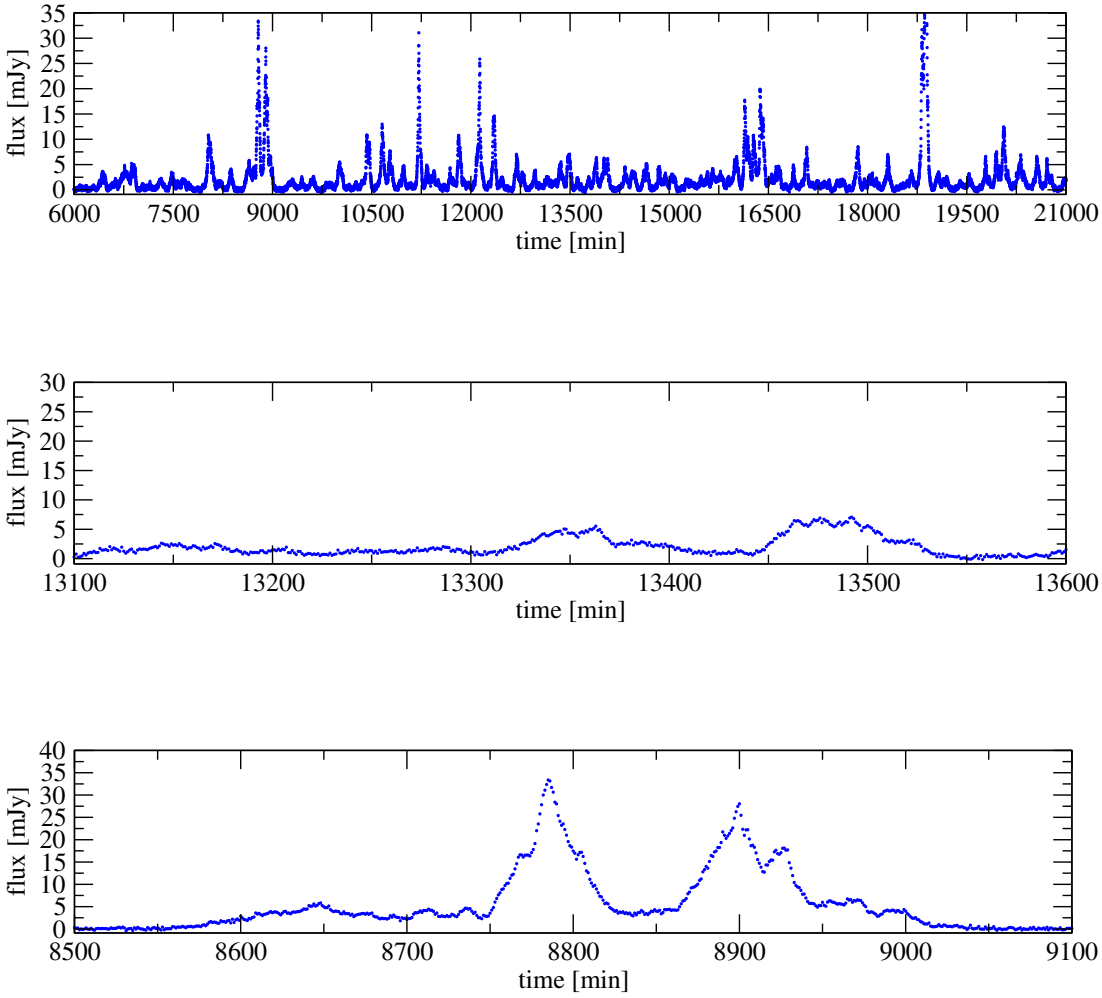

Fig. 2.19.: Simulated lightcurves taken from a $4 \cdot 10^6$ min time series created with a single-broken power-law PSD with an acceptance of 68%, corresponding to the blue structure function in Fig. 2.17. The upper panel shows typical 15000 min, the lower panels 500 min closeups with lower and higher flux density levels.

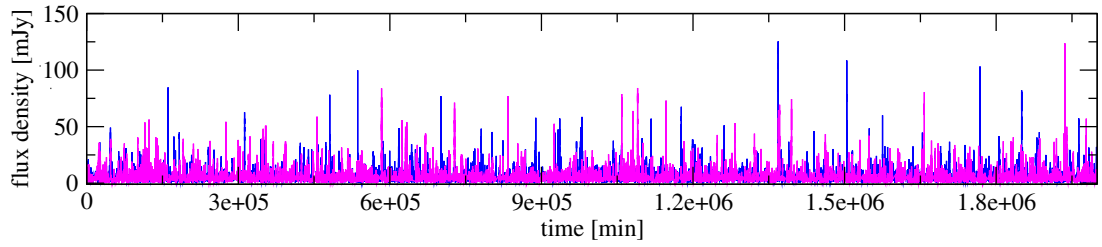

Fig. 2.20.: Long term appearance of light curves generated with the best single (blue) and the best double (magenta) broken PSD. On a time period of $2 \cdot 10^6$ min no obvious difference is noticeable.

Anyhow, confidence levels deduced from acceptance values take into account the probability that the observed sample is not representative for the true variability but a statistical "outlier", a possibility that, considering the coverage fraction of 0.4%, makes any conclusion unreliable. For example, on a 90% confidence level, the light curves generated from PSDs with acceptance values of 68% and 94%, respectively, (Fig. 2.20) are indistinguishable. On the other hand, under the assumption that we actually are looking at a typical sample that represents the variability of a continuous 15000 min data piece quite well, we find a clear argument against the 68%-PSD: The generated light curve shows too many flares on the 20-30 mJy level. This demonstrates that the insignificance of a break at lower timescales due to identical acceptance values is more fundamental than the criticism that we might look at an exotic realization of the underlying process, or that the analysis suffers from an accidental selection effect: With the time support of our observations, especially with the day-night gap, we cannot decide on question whether a PSD-break at timescales between 25 and 100 minutes is constituent for variability, even if we assume that my data sample is representative.

As a last step I can use the 5000 re-sampled light curves with the best fitting structure function to test the plausibility of the power-law assumption as described in section 2.2.2 (now taking into account the time correlation). I find a goodness parameter of $q = 0.79$ (as defined in section 2.2.2), much higher than the value of $q = 0.2$ for independent data, firmly establishing the plausibility for the power-law description of the probability density. The observed CDF and the CDFs of 20 randomly selected surrogate light curves are shown in Fig. 2.21. The values of the parameters in Eq. (2.20) can be confirmed also for the case of correlated data, the uncertainties are slightly bigger (0.15 mJy for x_0 and $x_{\min}$, and 0.3 for α).

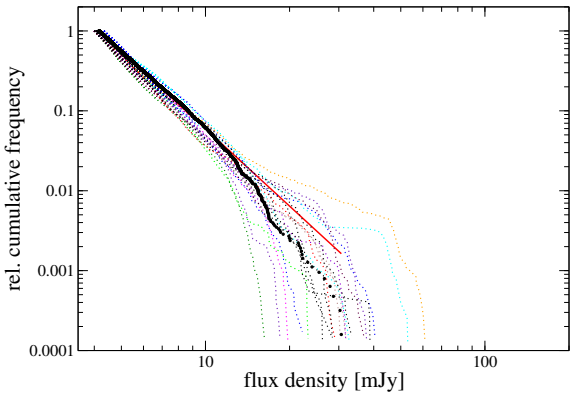

Fig. 2.21.: The observed CDF (black) of flux densities and 20 randomly selected CDFs of time correlated power-law surrogate data (colored dashed lines). The best fit CDF is shown as a continuous red line.

2.4. Extreme flux density excursions and the X-ray echo

In this section I investigate the consequences of an extrapolation of the measured time correlated power-law to high flux density levels and long timescales. It is obvious that infinitely bright outbursts are unphysical, rising the question of a physical constraint for the maximum flux densities that can be expected.

2.4.1. Maximum expected NIR flux density

Recent measurements of the VLBI source Sgr A* at 230 GHz resulted in a lower limit to the brightness temperature of $T_b = 2 \times 10^{10}$K (Doeleman et al. 2008). For the case of a synchrotron source the relations between observed and intrinsic flux densities and frequencies

$$S_{obs} = \delta^{3-\alpha} S_{int} \tag{2.42}$$

$$\nu_{obs} = \delta \nu_{int} \tag{2.43}$$

$$\delta = (1-\beta^2)^{\frac{1}{2}} \cdot [1-\beta \cdot \cos(\phi)]^{-1} \tag{2.44}$$

$$\beta = \frac{v}{c} \ , \tag{2.45}$$

with v the bulk motion of the synchrotron region, ϕ the viewing angle toward the emitting component, α the spectral slope, and ν_{int} the self-absorption peak frequency in GHz, result in a brightness temperature (including the possibility of beaming):

$$T_b = \frac{1.22\ S_{obs}}{\theta^2 \nu_{obs}^2} = \frac{1.22\ S_{int}}{\theta^2 \nu_{int}^2} \delta^{1-\alpha} \quad , \tag{2.46}$$

θ is the source diameter in milliarcseconds and T_{12} is the equipartition brightness temperature in units of 10^{12}K (see Eckart et al. 2012). Thus, for constant θ and δ the brightness temperature is proportional to the flux density. From 345 GHz and 690 GHz SMA measurements, there is evidence that the self-absorption peak frequency of most synchrotron source components in Sgr A* peak around 345 GHz (Marrone 2006; Marrone et al. 2006a,b, see also Eckart et al. 2012). With the lower limit for the brightness temperature mentioned before, which has been obtained close to this peak frequency, we can calculate a flux density limit which extreme outbursts in the NIR must reach, assuming that the size of the luminous region stays approximately constant and that the brightness temperature is linked to optically thin infrared emission. On the other hand the maximum brightness of the synchrotron source Sgr A* is certainly given by the inverse Compton limit of 10^{12}K (or a few times 10^{12}K in the case of boosting). With both constraints the maximum brightness of Sgr A* can be expected to be about

100 times brighter than regular flare amplitudes. Since these amplitudes reach K-band flux densities of around 20 to 30 mJy, extreme values about 3 Jy can be expected. Only for smaller source sizes and lower self-absorption frequencies, or higher bulk motions during the flare the expected extreme K-band flux density may be lower.

2.4.2. A possible explanation of the X-ray light echo

The present X-ray luminosity of Sgr A* is more than 10 orders of magnitude less than its Eddington luminosity. The observation of hard X-ray emission and iron fluorescence from some of the massive molecular clouds surrounding the Galactic Center has been interpreted as a light echo of a luminous past flare, that may have happened up to 400 years ago (Revnivtsev et al. 2004, Sunyaev & Churazov 1998, Terrier et al. 2010). Terrier et al. (2010) report the observation of a clear decay of the hard X-ray emission from the molecular cloud Sgr B2 during the past seven years. They argue that this decay strengthens the case for such a bright flare in the past and significantly weakens the alternative explanations involving low-energy cosmic rays. The authors also argue that the luminosity of the event was 1.5-5$\times 10^{39}$ erg s^{-1} and that the period of intense activity of Sgr A* that may be responsibly for the observed light echo ended about 150 years ago.

If we assume that the infrared flares are linked to X-ray flares by the underlying radiation mechanism, it makes sense to compare the statistics of the brightest X-ray events with my infrared flare statistics that we obtained over the recent $\sim$7 year period. Lets us assume that such a bright flare in the X-ray domain occurred between 150 and 400 years ago. This means that its occurrence is between a factor 5×10^{-2} and 7×10^{-5} less frequent than the brightest infrared flares observed until today (one 30 mJy event every 15000 minutes - as obeserved - to one 30 mJy event every 7 years in the case that the brightest observed flare was the brightest over the total periode of seven years). The bulk of the X-ray flares observed in recent years lies between 10^{34} to $3\times$ 10^{35} ergs/s (Baganoff et al. 2001, 2003, Porquet et al. 2003, 2008). Assuming an optically thin spectrum between the NIR and X-ray domain, and assuming that the brightest K-band flares (of 10 to 30 mJy) sample the brightest X-ray flares, we can expect that the K-band flux density associated with the flare 150-400 years ago has been 0.05×10^5 to 5×10^5 times higher (corresponding to 50-15000 Jy) than what we have observed until today. This is 2 to 4 orders of magnitude above the K-band flux density limit I estimated for the case of the inverse Compton limit. Hence an optically thin NIR/X-ray flare can be excluded as the source of the light echo.

However, the requirements on the K-band flare brightness are considerably reduced if we assume a synchrotron self-Compton (SSC) mechanism as a source of the bright X-ray flare. We assume a synchrotron radio spectrum with a turnover between the

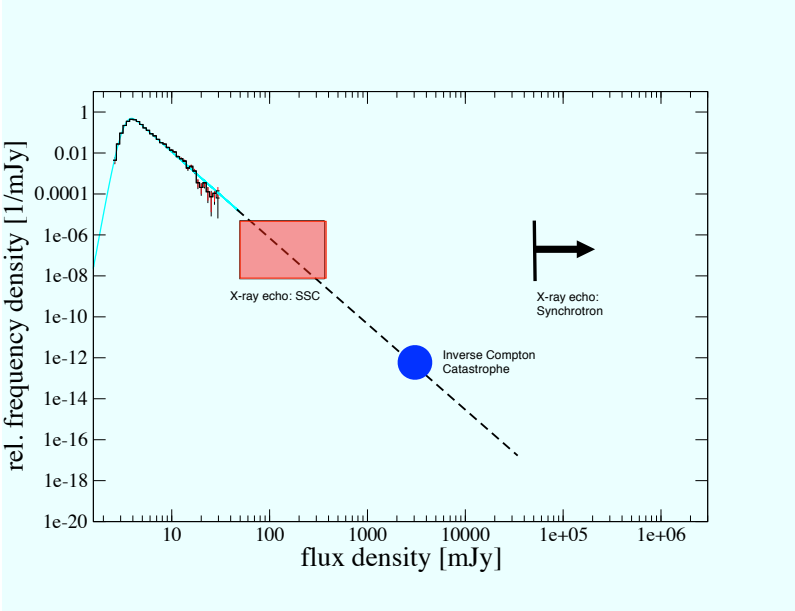

Fig. 2.22.: Illustration of the likelihood of extreme flux density excursions extrapolated from the statistics of the observed variability. The expected maximum flux density given by the inverse Compton catastrophe and an estimate of its uncertainty are shown as the blue circle, the SSC infrared flux density for a bright X-ray outburst as expected from the observed X-ray echo is depicted as the red rectangular.The lower limit for the NIR flux density in the case of a pure synchrotron model is indicated with the black arrow.

optically thick and the thin part at a frequency of ν_m (in GHz) and a flux density S_m (in Jy) with an optically thin spectral index α

$$S_\nu \propto \nu^{-\alpha}. \tag{2.47}$$

Adapting the formulae given by Marscher (1983, 2009) for the case of the Galactic Center, we then find that the SSC X-ray flux density $S_{X,SSC}$ (in μJy), is given by

$$\begin{aligned} S_{X,SSC} &= d(\alpha) \ln\left(\frac{\nu_2}{\nu_m}\right) \theta^{-2(2\alpha+3)} \nu_m^{-(3\alpha+5)} \\ &\quad \times S_m^{2(\alpha+2)} E_X^{-\alpha} \delta^{-2(\alpha+2)} \quad , \end{aligned} \tag{2.48}$$

where $d(\alpha)$ is a dimensionless parameter and E_X the X-ray photon energy in keV. Relativistic boosting, denoted by δ, may occur for anisotropic motion along a jet, or due to orbital motion close to the black hole, or due to a rapid isotropic expansion of a source component (see discussion by Eckart et al. 2012). With the $S_{X,SSC} \propto S_m^{2(\alpha+2)}$ dependency the 10^4 to 10^5 increase in X-ray luminosity can be achieved by an increase of the K-band flux density by a factor of 5 to 12. Here I used a synchrotron spectral index α of 0.7±0.3 (Hornstein et al. 2007, see also Bremer et al. 2011) and assumed that source sizes and turnover frequencies are similar to what had been obtained for

the recently observed flares. This indicates that the light echo could be produced by a 50 to 360 mJy flare that is a factor of 5×10^{-2} to 7×10^{-5} times less frequent than the recently observed brightest Ks-band flares. These are flux densities that are well below those derived for the inverse Compton limit. Assuming that the frequency of occurrence (measured in min^{-1}) of peak flux densities of rare events is proportional to the frequency of flux densities in the flux density histogram (measured in mJy^{-1}), and with a frequency of about 10^{-4} mJy^{-1} for flux densities around 30 mJy we obtain a range of 5×10^{-6} - 7×10^{-9} mJy^{-1} and 50-360 mJy in the frequency-flux density diagram. Fig. 2.22 shows that (within the uncertainties) these values are in agreement with the extrapolated probability density of the K-band flux densities as obtained over the past 7 years and does not require an extraordinary event as an explanation. Also the long light curves in Fig. 2.20 show that flares with amplitudes up to 100 mJy can be expected already for continuous light curves of $2 \cdot 10^6$ min, and for 5000 light curves with the observational time support we find typically 5-7 datasets with maximum flux densities over 250 mJy.

2.5. Summary

I summarize the results of this part of my thesis:

- The NIR flux density distribution of Sgr A* as obtained from the last seven years of observations is in convincing agreement with a pure power-law distribution, not giving any indication for a break or two-state behavior.
- I could find an upper limit of the intrinsic mean flux density of about 1.7 ± 0.15 mJy, and with a power-law extrapolation to flux densities below the detection limit a mean of 0.9 ± 0.15 mJy.
- I found an algorithm to statistically simulate light curves that show the same flux density distribution and time correlation as the observed sample. It is based on the algorithm by Timmer & Koenig (1995) to generate linearly time-correlated surrogate samples, but includes a transformation to account for the non-linear appearance of the NIR flux densities of Sgr A*. The broken power-law PSDs relevant to us are in first approximation invariant under this transformation. This statistical model (best fitting PSD, flux density distribution and the algorithm) does not provide immediate information on the physical system, but serves as a statistical "summary" of the observed variability, defining constrains for every physical model. Furthermore, it allows a straight forward power-law extrapolation to higher flux density levels, flux density levels below the detection limit, and long timescales.

- This extrapolation demonstrates that high flux density excursions as required to explain the supposed X-ray light echo in the molecular clouds surrounding Sgr A* are well within the expected statistical extreme values of the variability that we observed at much lower flux densities, and catastrophic events are not required to explain this phenomenon.

- The question if timescales comparable to the orbital timescale at the innermost stable orbit play a role for the variability is principally undecidable on the base of this data. In order to access this problem a significant amount of continuous light curves with durations longer than 1500 min would be needed. This, however, does not exclude the presence of orbital signatures in polarimetric data as reported in Zamaninasab et al. (2010), and since here I am investigating all light curves in total under the assumption of stationarity, I cannot make statements on a possible time development of the dominant timescale, or the role of shorter timescales for brighter states only.

3. Near Infrared Polarimetry

The polarization of electromagnetic radiation can be an essential piece of information to determine the nature of emission processes and the physical parameters of the environment in which the radiation is generated. In a very general sense, polarization is a tracer of asymmetry, either in the radiative process itself or in the radiative transfer processes that may influence the light along the line of sight towards us. The asymmetry that is the origin of the polarization (e.g. due to magnetic fields or asymmetric grain shape of dust particles) often is very small, and so is the fraction of polarized light. On the other hand, even if the fraction of polarized light is high, the measurement of the polarization state remains very challenging. This is true in particular for the emission from Sgr A*. The investigation of the emission from Sgr A* and the application of model calculations to the observed light curves of polarized light decisively depend on the quality of the polarization calibration. The NIR polarization data were obtained through NACO. This system is mounted at a Nasmyth focus of the altitude azimuth mounted UT4 telescope, which complicates the exact polarimetric calibration. Therefore I carried out a detailed analysis of the instrumental properties of this system, determined the systematic instrumental uncertainties and discuss their influence on the Sgr A* measurements and the consequences for the astrophysical interpretation of the light curves obtained in polarized light.

The goal of this part of my thesis is to investigate the instrumental polarization (IP) on a base of data which are the outcome of seven years of observations of Sgr A*. These data are optimized for the astrophysical time series analysis of Sgr A* with high-time resolution. They nevertheless provide enough information to tackle two aspects of the systematic instrumental effects: On one hand the description of the IP and its behavior in absolute values with an accuracy of about 1% in linear polarization degree, and on the other hand the systematic uncertainties of the time variability of the polarimetric parameters of Sgr A*.

NACOs mode for polarimetric differential imaging combines a Wollaston prism (in the following referred to as Wollaston), which allows for measuring two orthogonal angles simultaneously, and a $\lambda/2$ wave plate (HWP). It does not, however, provide information on circular polarization, and the flat-field calibration data are not optimized for polarimetric measurements. Both facts necessitate complicated procedures for calibrating the existing data. In observation periods before 2008 a wire grid mode

was available as well. To determine the instrumental polarization (IP) of this instrument I used the Stokes and Mueller calculus. This allows me to describe the influence of the optical elements on the polarization and to determine the IP as a function of the parallactic angle. It is developed following a model for the IP of the Telescopio Nazionale Galileo (TNG) presented in Giro et al. (2003). Since it is crucial for the following to have a clear definition of conventions and variables I first introduce some basic formalism.

3.1. Basics of Polarimetry

The projection of the electric field vector E of fully linearly polarized light onto a preferential direction that makes an angle ψ with the E-vector is given by

$$E_\psi = E_0 \cos(\psi) \; . \tag{3.1}$$

The energy carried by the projected electromagnetic wave and thus the intensity is proportional to E^2:

$$I \sim E_\psi^2 = E_0^2 \cos^2(\psi) \; . \tag{3.2}$$

For partially linearly polarized light - defined by $I_{\rm tot}$ the total intensity, P the degree of linear polarization, and ϕ the polarization angle - the dependency of the intensity on the angle θ of the preferential direction is given by

$$I_{P,\phi}(\theta) = \frac{I_{\rm tot}}{2} + \frac{P I_{\rm tot}}{2} \cos(2\,[\theta - \phi]) = I(\theta) \; . \tag{3.3}$$

θ is measured with respect to the polarization angle reference that defines ϕ and commonly is given by the north-south axis on the sky[1]. $I(\theta)$ is the intensity I would measure with an analyzer at the angle position θ and a transmittance of unity. See Fig. 3.1 and Fig. 3.2.

A convenient tool to describe partial polarization of incoherent light is the Stokes formalism. The normalized Stokes vector for partial (linear) polarization is defined as

$$S = \begin{pmatrix} I_{\rm tot} = 1 \\ Q \\ U \\ V \end{pmatrix} \; , \tag{3.4}$$

with

$$\begin{aligned} Q &= \frac{I(0^\circ) - I(90^\circ)}{I(0^\circ) + I(90^\circ)} \\ U &= \frac{I(135^\circ) - I(45^\circ)}{I(135^\circ) + I(45^\circ)} \; . \end{aligned} \tag{3.5}$$

[1] It is the direction of the linear polarization if $U = 0$ (see Eq. (3.5)) and also defines the orientation of the Mueller matrices below.

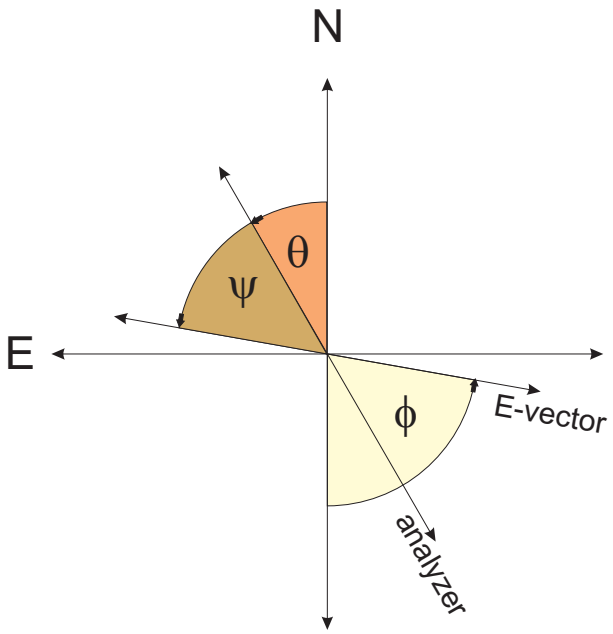

Fig. 3.1.: Orientations and angles for Eq. (3.2) and (3.3) with $\psi = \phi - \theta$.

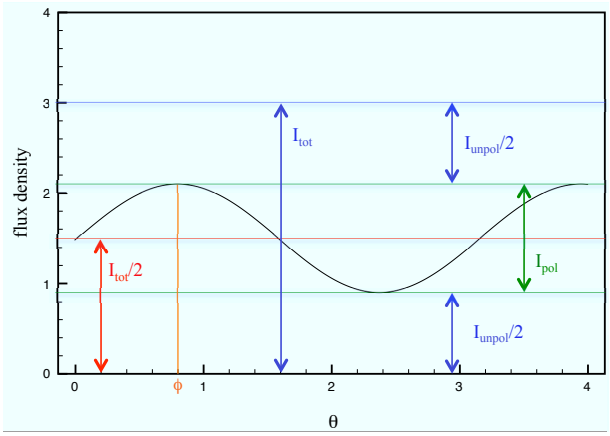

Fig. 3.2.: Intensity of partially polarized light (in arbitrary units) as a function of the orientation of the polarimetric analyzer θ for light with a linear polarization degree of 40% and a polarization angle ϕ.

Q and U represent the linear polarization and V the circular polarization (NACO does not provide a $\lambda/4$-wave plate to measure V). The parameters P and ϕ are related to Q and U by

$$\begin{aligned} P &= \sqrt{Q^2+U^2} \\ \phi &= \frac{1}{2}\arctan\left(\frac{U}{Q}\right) . \end{aligned} \tag{3.6}$$

In this formalism the influence of any optical element on the intensity and polarization can be expressed by a linear operation on the Stokes vector:

$$S' = M \times S\,, \tag{3.7}$$

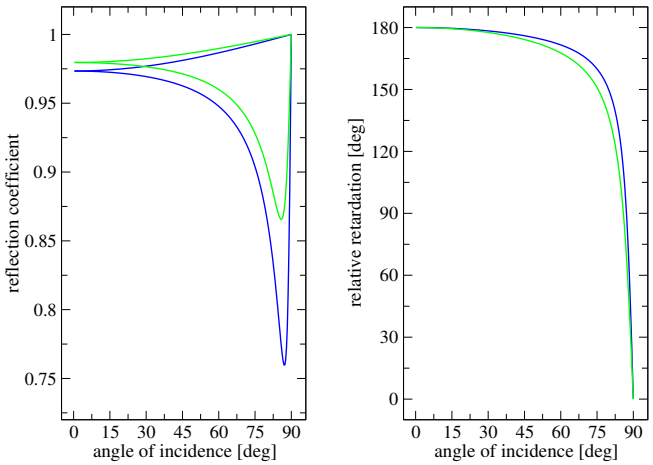

Fig. 3.3.: Reflection properties of metallic surfaces in Ks-band. The green curves represent gold, the blue aluminum.

where M is the Mueller matrix of the element, S the Stokes vector of the incoming light and S' the Stokes vector of the outgoing light. The elements of the Mueller matrix represent the linear dependency of each Stokes parameter in S' on those in S.

3.2. Metallic reflection

The optical elements considered here are mainly mirrors with metallic coatings. For these surfaces every incident electromagnetic wave can be decomposed in a component parallel to the plane of incidence and one perpendicular to this plane. As described in detail by Giro et al. (2003) and Clarke (1973), reflections at metallic surfaces have two effects: (1) a reflection introduces a linear polarization because the reflectivity for these components is different; (2) the reflection causes a circular polarized contribution by shifting the phase between the components. Both effects can be described by a Mueller matrix that combines the matrix elements for a linear polarizer and a retarder:

$$R = \begin{pmatrix} \frac{1}{2}(r_\perp + r_\parallel) & \frac{1}{2}(r_\perp - r_\parallel) & 0 & 0 \\ \frac{1}{2}(r_\perp - r_\parallel) & \frac{1}{2}(r_\perp + r_\parallel) & 0 & 0 \\ 0 & 0 & \sqrt{r_\perp r_\parallel}\cos(\delta) & -\sqrt{r_\perp r_\parallel}\sin(\delta) \\ 0 & 0 & \sqrt{r_\perp r_\parallel}\sin(\delta) & \sqrt{r_\perp r_\parallel}\cos(\delta) \end{pmatrix}, \tag{3.8}$$

with $r_\perp$ and $r_\parallel$ the reflection coefficients for the two components and δ the relative retardation between the components. With the material-dependent refractive index and extinction coefficient all three parameters can be calculated by using the Fresnel formulae.

In the left plot of Fig. 3.3 I show the reflection coefficients for p- and s-waves as a function of the angle of incidence for Ks-band. In the right plot of Fig. 3.3 I show

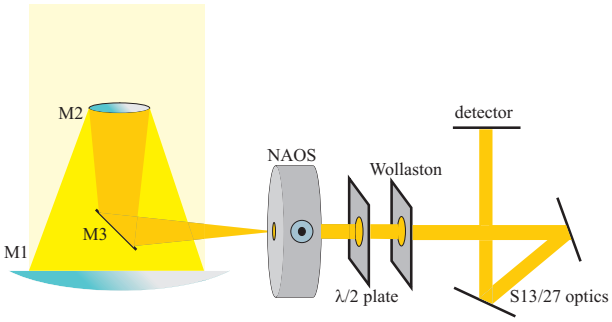

Fig. 3.4.: Optical elements of UT4, NAOS & CONICA and their relative orientation in the moment of the meridian transit.

the relative retardation between p- and s-wave. Here the retardation for 0° angle of incidence is defined to be 180° in phase, i.e. a mirror hit by a perpendicular beam is considered to have the same effect as a HWP. The material constants (Ks-band) used for these plots are listed in Table 3.5.
Eq. (3.8) defines the Mueller matrix for metallic reflection in a way that the preferential direction of the matrix (the direction of the introduced polarization, always perpendicular to the plane of incidence) is oriented parallel to the polarization angle reference (generally north-south). To change the (perpendicular) orientation of the plane of incidence with respect to the polarization angle reference by an angle γ, one has to apply the transformation

$$R' = T(-\gamma) \times R \times T(\gamma) \,, \tag{3.9}$$

with T the rotation in Stokes space, which is defined as

$$T(p) = \begin{pmatrix} 1 & 0 & 0 & 0 \\ 0 & \cos(2p) & \sin(2p) & 0 \\ 0 & -\sin(2p) & \cos(2p) & 0 \\ 0 & 0 & 0 & 1 \end{pmatrix} . \tag{3.10}$$

3.3. The optical train of NACO

NACO is mounted at the Nasmyth focus of VLT Yepun. Because of the 45° tilted folding mirror M3 (see Fig. 3.4) that sends out the beam to the Nasmyth focus, NACO has a significant instrumental polarization that is depending on the parallactic angle. In the ESO user manual the total IP is estimated to be up to 4%. NACO provides various setups for polarimetry combining different cameras (with different pixel scales) and filters with the Wollaston and the HWP. A table of available cameras and filters is shown in Ageorges et al. (2007). Here I am concentrating on the most commonly used setup: The cameras S13 and S27 with the Ks-band filter, the Wollaston, and the HWP. The field of view of S13 in combination with the Wollaston analyzer and the polarimetric mask is shown in Fig. 3.5. The upper stripe is the ordinary beam (0°) and the

lower one the extraordinary (90°). The angle positions of the HWP in the header[2] of the NACO data is counted with the same sense of rotation. Note that this sense is reverse to the sky because the number of mirrors is odd and every mirror turns it once (see Fig. 3.4 and Fig. 3.6).
Not only M3 contributes to the IP of NACO. Every significantly inclined reflective surface in the light train has to be included in a model of polarimetric instrumental systematics. All optical elements (including the analyzer) and their relative orientations are discussed below. In Fig. 3.4 I show the optical elements of UT4 and NACO. In this sketch the direction of the optical train within NAOS (defined by the connection line between the input mirror and P1 in Fig. 3.6) is perpendicular to the paper plane and indicated by the face-on arrow sign on NAOS. A sketch of NAOS is shown in more detail in Fig. 3.6.
A de-rotation of the parallactic angle rotates the optical train beginning with NAOS with respect to the mirrors M1/2/3. The elevation rotation is only affecting the hole assembly because the rotator of NACO compensates for it. It does not influence the IP. After HWP and Wollaston there are two more folding mirrors in the architecture of CONICA; the inclinations of these two mirrors are different for different cameras (see Table 3.5 and angles of incidence ε therein). The light train of NAOS in Fig. 3.6 shows that there are only two mirrors with a significant inclination: the input and output mirror (red). The parabolic mirrors P1 and P2, the tip-and-tilt mirror TTM, and the deformable DM have inclinations $\leq 5°$ and can be neglected. The specifications of the dichroic have not been accessible for me, but here the inclination of only about 12° is also very small.

3.4. A model for the instrumental polarization of NACO

3.4.1. Instrumental polarization generated by M3

M3 is coated with aluminum and inclined by 45°. To understand the position-dependent part of the IP, it is important to analyze the time-depending orientation of M3.
The common angle reference at the sky is the north-south axis. At the Nasmyth focus this direction is parallel to the plane defined by the edge of the main mirror M1 in the moment of the meridian transit of the source. In this moment the north-south axis is parallel to the preferential direction of the matrix in Eq. (3.8) (see Fig. 3.4). At all other moments it is tilted by $-p$ with respect to the preferential direction of matrix (3.8) (with p the parallactic angle).

[2]The angle position of the HWP is reported in the NACO FITS header under the keyword "INS RETA2 ROT"; the encoder position can be found under "INS ADC1 ENC".

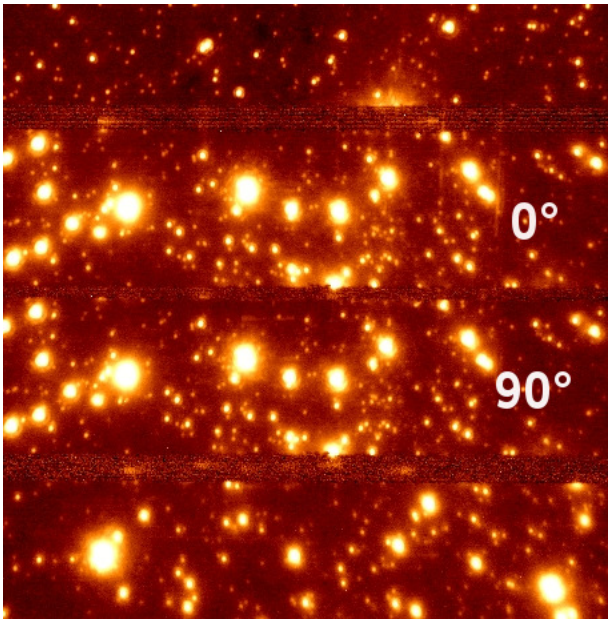

Fig. 3.5.: Polarimetric observations with the Wollaston: the picture shows a frame observed with the S13 camera. The image taken with the ordinary beam of the Wollaston is the upper stripe.

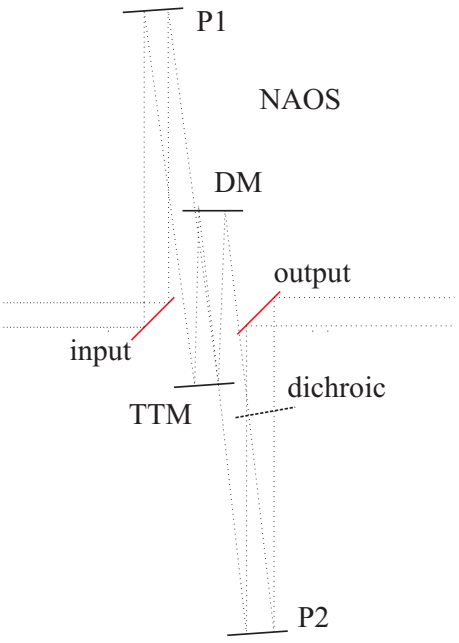

Fig. 3.6.: Light train in the adaptive optics module NAOS.

In order to transform matrix (3.8) to the north-south reference at any moment, we have to use a transform similar to Eq. (3.9). After changing the reference from the celestial system to the reference system of M3 and applying R for the metallic reflection, we have to transform to the detector reference. The detector is de-rotated, it follows the elevation rotation of the Nasmyth focus and the parallactic rotation of the source[3]. After the reflection this parallactic rotation has the reverse sense, thus the position depending part of the IP can be expressed as

$$M_{\mathrm{M3}} = T(p) \times R_{\mathrm{alu}} \times T(p) \,, \tag{3.11}$$

where R_{alu} is the reflection matrix for bare aluminum with the values listed in Table 3.5.

3.4.2. The IP of the adaptive optics module NAOS

The two 45° inclined Silflex coated folding mirrors in the adaptive optics module NAOS are described by the square of matrix (3.8):

$$M_{\mathrm{NAOS}} = R_{\mathrm{sil}} \times R_{\mathrm{sil}} \,. \tag{3.12}$$

The material constants for Silflex have been provided by the producer Balzers Optics and can be found in Table 3.5.

3.4.3. The retarder plate

The polarimetric analyzer is part of the camera CONICA. It mainly consists of the HWP, the Wollaston, and the detector. The HWP turns the angle of the linearly polarized part of the light by the double of its position angle. The position angle is the angle between the fast axis (or slow axis, the degeneracy is 90°) and the polarimetric angle reference. The formula (see Table 3.4.3) given in the ESO manual for the dependency of the position angle (angle with respect to the north-south axis) on the encoder steps has to be modified. The plot in Fig. 3.7 shows the un-calibrated polarization of IRS21 in a dataset taken in 2005 with the Wollaston. The dataset exhibits an offset in polarization angle of about 14° in comparison with Ott et al. (1999). A maintenance of NACO in autumn 2009 revealed the actual position angle reference. The true offset is $(13.2 \pm 0.3)°$ (see Table 3.4.3), a value that agrees very well with the value of 14° that I predicted from the observational data before the intervention. The previously reported angular offset of 34° (Trippe et al. 2007) could not be verified. This value may result from the offset I found combined with the fact that Trippe et al. (2007) use a sine- rather than a cosine-function to describe the 2θ-dependency of the polarized channel

[3] i.e. the angle between main mirror and detector orientation only depends on the parallactic rotation.

flux. This causes a 45°-shift in the opposite direction to the HWP offset, resulting in a total of 32°.

The HWP was installed on 2003 August 8, and I assume that the offset is constant for all epochs since then.

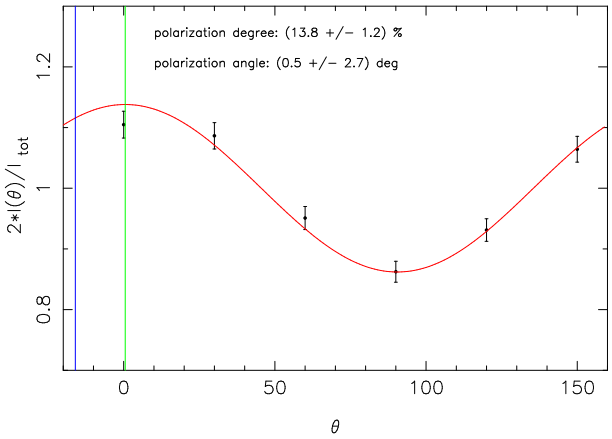

Fig. 3.7.: IRS21 in 2005 (Wollaston). The plot shows the intensity divided by $I_{\mathrm{tot}}/2$ as a function of angle θ (as defined in Eq. (3.3)). The data are obtained from mosaics. No calibration was applied. The green line marks the measured polarization angle, the blue the published angle (9.8%@14°) from Ott et al. (1999). In this plot the angle is counted in the instrument sense (negative with respect to sky).

Encoder steps	Angle [deg]
Manual :	
x	$\alpha = (x+205)*0.08789$
$-205 \sim 3891$	0
51	22.5°
0	$205*0.08789 = 18.02$
Revision :	
0	(11.4 ± 0.2)
Difference :	
	(-6.6 ± 0.2)

Table 3.1.: Encoder positions of the HWP. The table shows that the actual reference system for the HWP is offset by $(-6.6 \pm 0.2)°$ with respect to the reference system assumed in the manual. This results in a positive angle offset of 13.2° for the polarization channels (in the instrumental sense of rotation). One turn of the plate corresponds to 4096 encoder steps. An angle of 0° actually corresponds to an encoder position of 3966.

3.4.4. The entire instrumental polarization of NACO

Because the plane of incidence of the NAOS light train is perpendicular to the plane of incidence of M3, we have to transform M_{NAOS} according to Eq. (3.9) with $\gamma = 90^\circ$. We also have to add a rotation matrix for the rotator adapter that de-rotates the instrument and can change the orientation of the field of view (from north-south on the y-axis of the detector to any angle). The discussed matrices and orientations finally result in a total Mueller matrix:

$$\begin{aligned} M_{\mathrm{NACO}} &= (\mathrm{Tr}\times)\,\mathrm{T}(-\beta)\times\mathrm{T}(90^\circ)\times\mathrm{M}_{\mathrm{NAOS}} \\ &\quad \times T(-90^\circ)\times T(\alpha)\times M_{\mathrm{M3}} \\ &= (\mathrm{Tr}\times)\,\mathrm{T}(-\beta)\times\mathrm{T}(90^\circ)\times\mathrm{R}_{\mathrm{sil}}\times\mathrm{R}_{\mathrm{sil}}\times\mathrm{T}(-90^\circ) \\ &\quad \times T(\alpha)\times T(p)\times R_{\mathrm{alu}}\times T(p)\,, \end{aligned} \tag{3.13}$$

with $-\alpha$ the angle of rotator adapter as reported in the ESO FITS header keyword "ADA POSANG" and $\beta = 13.2^\circ$ the offset of the HWP. The matrix Tr represents the effects of the analyzer and its transmission. It is included here for the sake of completeness. A more detailed discussion of these effects and their correction will follow in section 3.6.

3.5. The instrumental polarization in numbers

In this section I investigate the behavior of the introduced model. All material-dependent parameters of this model are summarized in Table 3.5. These parameters are mainly literature values for the materials. In section 3.8 the model is compared with standard stars and light curves of bright GC stars, which exhibit the variations of the IP with the parallactic angle. To match the observations the material constants k for aluminum and δ for the Silflex coating had to be slightly changed as described in the captions of Table 3.5. Here I already discuss the final version of the model that is gauged with the calibration sources. In section 3.8 I will then justify the model and the chosen parameters.

I am now able to evaluate the contributions of the different optical elements quantitatively. First I numerically express the matrices of Eq. (3.13). For the given material parameters and a parallactic angle of 0° I find M_{M3} to be

$$M_{\mathrm{M3}} = \begin{pmatrix} 0.972 & 0.009 & 0 & 0 \\ 0.009 & 0.972 & 0 & 0 \\ 0 & 0 & -0.969 & -0.067 \\ 0 & 0 & 0.067 & -0.969 \end{pmatrix}, \tag{3.14}$$

Coating	Mirror	n	k	ε [deg]	$r_{\parallel}$	$r_{\perp}$	δ [deg]
Alu.	M3	2.75	20.0	45°	0.96262	0.98113	176.03
Silflex	NAOS I&II	–	–	45.00	0.98272	0.98872	165.00
Gold	S13 I	0.99	13.8	42.05	0.97266	0.98484	175.02
	S13 II			2.95	0.97959	0.97964	179.98
	S27 I			27.65	0.97701	0.98193	177.99
	S27 II			17.35	0.97865	0.98054	179.23

Table 3.2.: Material constants of coatings. Refractive index n, extinction coefficient k, reflection coefficients, and relative retardation for the coatings of NACO at 2.2μ. ε is the angle of incidence for which the reflection coefficients and relative retardation was computed. The material constants can be found on www.RefractiveIndex.info. The default k value for aluminum is 22.3, and δ for Silflex is 166.6 according to Balzers Optics specifications. Both values have been changed to match the position dependency of measured Stokes parameters (see section 3.8.2).

and for a parallactic angle of 45°

$$M_{\mathrm{M3}} = \begin{pmatrix} 0.972 & 0 & 0.009 & 0 \\ 0 & 0.969 & 0 & -0.067 \\ -0.009 & 0 & -0.972 & 0 \\ 0 & -0.067 & 0 & -0.969 \end{pmatrix} . \tag{3.15}$$

Obviously the main effect of the tertiary mirror is an $I \rightarrow Q/U$[4] cross talk of about 1% of the total intensity. The cross talks between linear and circular polarization can be on the order of 7% of Q/U or V respectively. For weakly polarized sources this is a minor effect. The transformed M_{NAOS} is given by

$$T(90^\circ) \times M_{\mathrm{NAOS}} \times T(-90^\circ) = \begin{pmatrix} 0.972 & -0.006 & 0 & 0 \\ -0.006 & 0.972 & 0 & 0 \\ 0 & 0 & 0.841 & -0.486 \\ 0 & 0 & 0.486 & 0.841 \end{pmatrix} . \tag{3.16}$$

Here Q is affected by about 0.6% of I and the $U \leftrightarrow V$ cross talks are on the order of 50% of the corresponding values U or V respectively. With these numerical matrices, Eq. (3.13), and the parameter α set to zero, we can write matrix M_{NACO} as

$$M_{\mathrm{NACO}} = \begin{pmatrix} 0.944 & 0.009c_p - 0.006 \\ -0.005 + 0.008c_p + 0.003s_p & 0.843 - 0.015s_p \\ -0.003 + 0.004c_p - 0.007s_p & 0.422 + 0.029s_p \\ -0.004s_p & -0.057s_p \end{pmatrix} \cdots$$
$$\cdots \begin{pmatrix} 0.009s_p - 0.001 & 0.000 \\ 0.366 + 0.015c_p & -0.211 - 0.059s_p + 0.025c_p \\ -0.731 - 0.029c_p & 0.421 - 0.029s_p - 0.051c_p \\ -0.472 + 0.057c_p & -0.816 - 0.033c_p \end{pmatrix} , \tag{3.17}$$

[4] Depending on the parallactic angle, this cross talk is affecting Q ($p = 0^\circ/90^\circ$), U ($p = 45^\circ/135^\circ$), or both of them.

with $c_p = \cos(2p)$ and $s_p = \sin(2p)$ describing the dependency on the parallactic angle. Tr was not included. This last expression gives all necessary information on the cross talks and their dependence on the parallactic angle. The cross talks from I to the linear polarization is on the order of $0.5\% - 1\%$ of the total intensity. There are also strong interactions between Q and U (on the order of 40% of the corresponding value Q or U respectively), between U and V (also on the order of 40%) and from V to Q (on the order of 20%). For not very strongly polarized sources the position-dependent variability of the linear polarization is dominated by the $I \leftrightarrow Q/U$ cross talks.
As an example for the telescope position-dependent behavior of the IP I plot in Fig. 3.8 Q, U, V, the linear and total polarization degree, and the polarization angle as functions of hour angle for an unpolarized source at the position of the GC (May, alt = 85.6° for meridian transit; solid lines in the plots). The IP of NACO reaches about 1.6% at maximum. Around hour angle zero the IP changes most rapidly, as is expected. Here the polarization degree reaches its minimum and the polarization angle swings to its other extreme. The curves are asymmetrical around zero because of the HWP offset.

3.6. CONICA and the polarimetric analyzer

Up to this point I discussed the influence of the optical elements that are located in front of the analyzer. In this section I consider the analyzer itself and its systematic effects on polarimetric measurements.
The main element of the analyzer is a polarizer. After the polarizer the only quantity of interest is intensity, because (for a polarizer with an efficiency sufficiently close to 100%) the polarization is known to be 100% in the direction of the polarizer (see Eq. (3.5)). Thus, the polarizer and the optical elements within the analyzer after the polarizer have to be investigated with respect to their relative attenuation of the different channels.
After the Wollaston the optics of CONICA include two more folding mirrors. These mirrors have gold coatings and show different inclinations for S13 and S27. Because after the Wollaston only the intensity of the two channels is important, it is not useful to work with matrix (3.8), which would describe the change in polarization inside the analyzer. We are interested instead in how the measurement of the Stokes vector of the light in front of the analyzer is affected by the different attenuation of the intensities of both channels inside the analyzer.
For CONICA the relative attenuation factors for the orthogonal channels of the Wollaston are the same for the measurement of Q and U, because the arrangement of the optical elements after the Wollaston does not depend on the position of the HWP. It is possible to find a Mueller matrix for this influence.

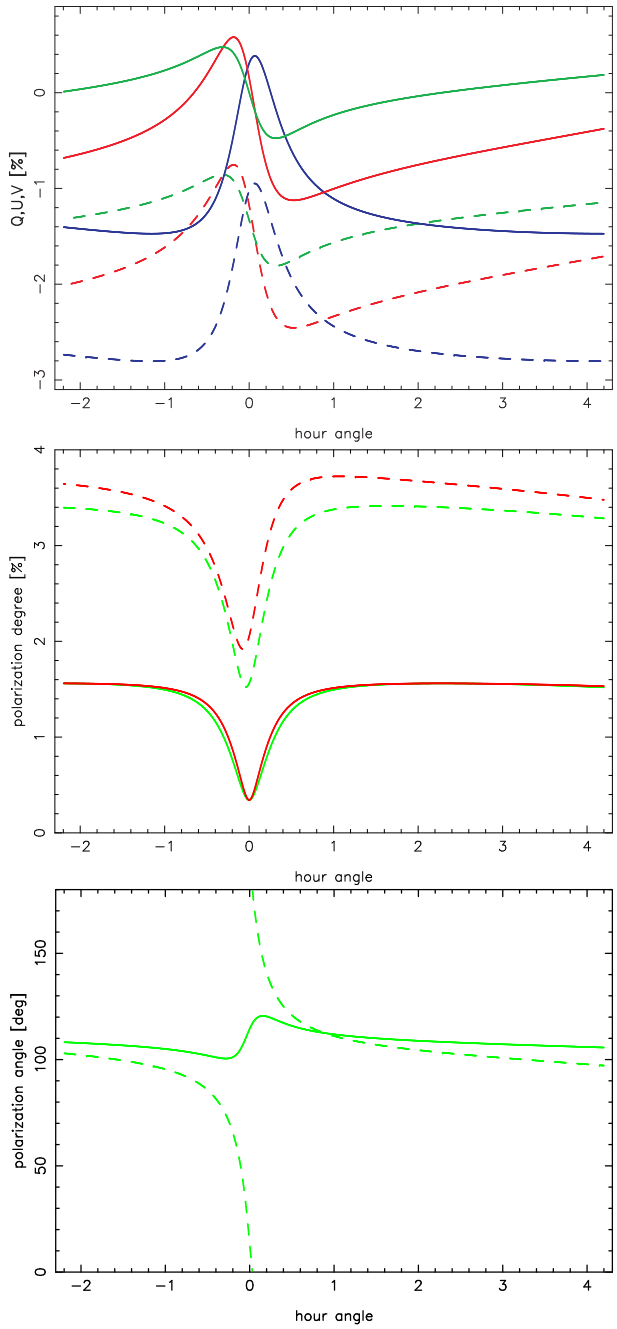

Fig. 3.8.: Upper panel: Instrumental polarization predicted by the model for an unpolarized source corresponding to matrix (3.17) (solid line) and including the systematic effects of the analyzer (see section 3.6 and Fig. 3.9 therein, dashed line). The curves show the Stokes parameters Q (blue), U (red), and V (green) as a function of hour angle. Here I considered the most common instrumental setup with Wollaston, HWP, and S13 optics. Middle: Linear (green) and total (red) polarization degree corresponding to the upper Stokes values. Lower panel: Polarization angle.

3.6.1. Müller-matrix for transmittance differences

The matrix to correct for a transmittance difference of the two orthogonal polarimetric channels after the Wollaston can be deduced in the following way: Let be I_1 and I_2 the intensity of the ordinary and the extraordinary beam, respectively. The folding mirrors after the Wollaston attenuate these intensities:

$$\begin{aligned} I_1' &= r_1 I_1 \\ I_2' &= r_2 I_2 \,, \end{aligned} \tag{3.18}$$

with $r_1 < 1$ and $r_2 < 1$ the attenuation factors of the ordinary and the extraordinary beam, respectively. Thus, the measured not normalized Q (other stokes parameters U and V analog) will be

$$\begin{aligned} Q' &= I_1' - I_2' \\ I' &= I_1' + I_2' \,. \end{aligned} \tag{3.19}$$

The correction matrix applied to the measured Stokes vector S' has to give the vector S, which results from the intensities I_1 and I_2. Because each of the Stokes parameters Q, U, and V is determined from a pair of orthogonal Wollaston channels, all of them are affected in the same way, and we can expect e.g. Q to depend on I' and Q' only (analog for U and V):

$$Q = xI' + yQ' \,. \tag{3.20}$$

This leads to the equation

$$I_1' \left(\frac{1}{r_1} - x - y \right) - I_2' \left(\frac{1}{r_2} + x - y \right) = 0 \,, \tag{3.21}$$

which has the solution

$$\begin{aligned} x &= \frac{r_2 - r_1}{2 r_1 r_2} \\ y &= \frac{r_2 + r_1}{2 r_1 r_2} \,. \end{aligned} \tag{3.22}$$

In a similar way we find the matrix elements for I. The resulting matrix is the inverse matrix of the transmission matrix Tr of Eq. (3.13) and can be written as

$$\mathrm{Tr}^{-1} = \frac{1}{2 \mathrm{r}_1 \mathrm{r}_2} \begin{pmatrix} T_+ & T_- & 0 & 0 \\ T_- & T_+ & 0 & 0 \\ T_- & 0 & T_+ & 0 \\ T_- & 0 & 0 & T_+ \end{pmatrix} \,, \tag{3.23}$$

with $T_\pm = r_2 \pm r_1$, and by inversion we find

$$\mathrm{Tr} = 2\mathrm{r}_1\mathrm{r}_2 \begin{pmatrix} \frac{T_+}{T_+^2-T_-^2} & -\frac{T_-}{T_+^2-T_-^2} & 0 & 0 \\ -\frac{T_-}{T_+^2-T_-^2} & \frac{T_+}{T_+^2-T_-^2} & 0 & 0 \\ -\frac{T_-}{T_+^2-T_-^2} & \frac{T_-^2}{T_+\left(T_+^2-T_-^2\right)} & \frac{1}{T_+} & 0 \\ -\frac{T_-}{T_+^2-T_-^2} & \frac{T_-^2}{T_+\left(T_+^2-T_-^2\right)} & 0 & \frac{1}{T_+} \end{pmatrix} . \tag{3.24}$$

For the Wollaston (polarization of the ordinary beam orthogonal to the plane of incidence at the first CONICA mirror) the attenuation factors r_1 and r_2 can be computed[5] from the reflection coefficients for gold for the corresponding angles of incidence (for values see Table 3.5)

$$\begin{aligned} r_1 &= \frac{1}{2}\left(r_\parallel^{\mathrm{gold,I}} r_\parallel^{\mathrm{gold,II}} + r_\perp^{\mathrm{gold,I}} r_\perp^{\mathrm{gold,II}}\right) \\ r_2 &= r_\perp^{\mathrm{gold,I}} r_\perp^{\mathrm{gold,II}} . \end{aligned} \tag{3.25}$$

3.6.2. Flat-field correction

Unfortunately the information on the attenuation caused by the two mirrors is not sufficient for a correction of the IP of CONICA. The characteristics of the Wollaston, in particular a possibly different transmission of the two beams, are not taken into account. These specifications have not been accessible for me, but information on the Wollaston and its transmission is carried by the flat-field that is taken routinely with mask and polarizer. To correct for these transmission differences the relative weighting of the orthogonal channels in the flat-field has to be conserved while normalizing the flat-field. This relative weighting also contains information on the attenuation of the CONICA mirrors after the Wollaston and additionally on the polarization of the calibration lamp that should be zero, but in reality does contribute. The calibration lamp consists of a halogen bulb within a slot of an Ulbricht sphere, which effectively depolarizes the light ($\sim 10^{-3}$% remaining). This light is then coupled in by a 45°-tilted gold mirror. This results in a maximum linear polarization of ~ 1% of the calibration light.

A comparison between a typical imaging and a Wollaston flat-field is shown in Fig. 3.9. Obviously the flat-field with the polarizer shows a significantly different distribution for the detector areas of the two channels, while a flat-field without polarizer exhibits a comparatively homogeneous response in these areas. The ratio of the mean values of the areas that correspond to the extraordinary and the ordinary beam respectively

[5] Under the assumption of 100% efficiency of the Wollaston as a polarizer and with the polarization of the ordinary beam perpendicular to the plane of incidence (first gold mirror of CONICA).

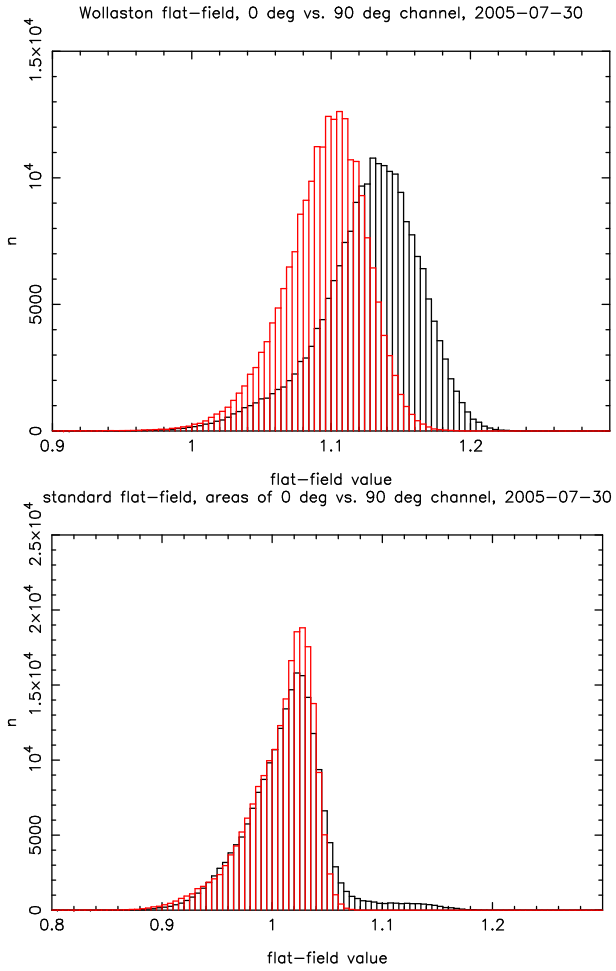

Fig. 3.9.: Histogram of flat-field pixel values in the regions of the orthogonal channels for the S13 polarimetric mask. The upper plot shows the histogram for a detector illuminated by the calibration lamp through the polarizer, the lower one for a simple imaging twilight flat.

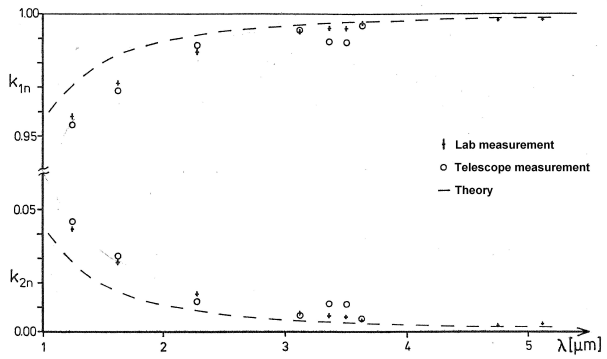

Fig. 3.10.: Normalized transmission for polarized light parallel (k_{2n}) and orthogonal (k_{1n}) to the wires of the grid (Fig. from Hodapp 1984). Grid period 0.25 μm, equally spaced on a CaF_2 substrate.

is 1.027 for the flat-field of 2005 (shown in Fig. 3.9), whereas the ratio of r_2 and r_1 obtained with Eq. (3.25) is only 1.006. Thus, I recommend the correction by the Wollaston flat-field because the influence of the transmission of the Wollaston (which is also different within the field of view of the individual channels) to the polarization can be on the order of 2% in polarization degree. The dashed lines in Fig. 3.8 show the same model as given by the solid lines, but now including the effects of the analyzer (simulated using Eq. (3.13) including Tr with $r_2/r_1 = 1.027$). The general behavior of the curves is the same, but the maximum of the IP is now as high as 4% and the angle flips over by full 180°.

I point out here that the polarization of the flat-field calibration light is on the same order as the remaining systematic error of the model described here and probably is the major contribution to the deviation from the standard stars (see section 3.8.2).

By using matrix (3.24) I assumed that the attenuation factors are the same for the measurement of Q as for the measurement of U, which is the case for the Wollaston, but not for the wire grid mode. The transmission correction for wire grids is even more complex. For NACO four wire grids were available for observations until and including 2007. The position angles of these grids can be found under the header keyword "INS OPTI4 NAME", which indicates the direction of the wires, thus for the polarization direction that is transmitted, 90° have to be added. For this mode one has to consider the more general case of a polarizer with an efficiency $\eta < 1$. Fig. 3.10 shows the efficiency as a function of the wavelength. Let η_1 be the efficiency of the polarization direction perpendicular to the wires and η_2 the efficiency parallel to the wires. Then the expressions for x and y in (3.22) are still valid if we replace r_1 and r_2 with r_1' and r_2', where

$$\begin{aligned} r_1' &= \eta_1 r_1 - \eta_2 r_2 \\ r_2' &= \eta_1 r_2 - \eta_2 r_1 \,. \end{aligned} \tag{3.26}$$

Here the attenuation factors are not the same for the measurements of the Stokes parameters Q and U: r_1 and r_2 have to be calculated separately for the two position angle pairs ($0°/90°$ and $45°/135°$) of the wire grids according to their the orientation with respect to the mirrors within CONICA. Because in this mode the flat-fields have also to be taken separately, they cannot be used easily to infer information on the relative transmission. The "boot strapping" method described in section 3.9.2 circumvents these problems.

3.7. Correcting the data for the instrumental systematics

To obtain the true polarization of a source we can apply the inverse of the Mueller matrix to the measured Stokes vector:

$$S = C_{\mathrm{NACO}} \times S' = M_{\mathrm{NACO}}^{-1} \times S' \,. \tag{3.27}$$

This is possible because every matrix in Eq. (3.13) is invertable and therefore M_{NACO} as well. An analytic solution for C_{NACO} can be found in appendix D. With NACO we cannot gain information on the circular polarization, and I have to assume $V' = 0$. However, because in the NIR the circular polarization for most sources can be neglected ($V = 0$) and the instrumental circular polarization of NACO can be on the order of 1%, the assumption of $V' = 0$ introduces an error of this range to the other Stokes parameters when applying the correction matrix C_{NACO}. To overcome this problem, an iterative algorithm has to be implemented with the following steps:

1. Compute the normalized parameters Q' and U' from NACO data; complete the Stokes vector S' with $I' = 1$ (because the Stokes parameters are normalized by intensity) and set $V' = 0$.

2. Apply C_{NACO} (as shown in appendix D) and obtain a first guess on the corrected Stokes vector: $S_{i=0} = C_{\mathrm{NACO}} \times S'$.

3. To initiate the i-th step define $\hat{S} = (\hat{I}, \hat{Q}, \hat{U}, \hat{V})$ by setting $\hat{I} = I_{i-1}$, $\hat{Q} = Q_{i-1}$, $\hat{U} = U_{i-1}$, $\hat{V} = 0$.

4. Compute the numerical inverse of C_{NACO} ($C_{\mathrm{NACO}}^{-1} = M_{\mathrm{NACO}}$) and apply it to $\hat{S}$: $\hat{S}' = C_{\mathrm{NACO}}^{-1} \times \hat{S}$.

5. Replace $V' = 0$ in S' (defined in step 1) with $\hat{V}' \neq 0$ (computed in step 4) and get $S_i = C_{\mathrm{NACO}} \times S'$.

6. For the next iteration step start from 3.

This algorithm quickly converges to a stable set of Stokes parameters. After 10 iterations the differences in the obtained solutions approach the computational uncertainties. It replaces $V' = 0$ by a value that guarantees V to be zero.
The algorithm has to be applied for every single frame and its corresponding parallactic angle and rotator position. Often it is necessary to work with mosaics that are obtained by averaging over a number of frames. Since the differences of the elements of the correction matrices for individual frames are often small within a dataset, it can be a suitable approximation to use the average of the matrices to correct polarimetric data that are obtained from mosaics.

3.8. Observations

In this section I now justify the presented model. The comparison with calibration star data shows that we can indeed describe the parallactic angle-dependent IP as it is observed. It also reveals to which accuracy I am able to compensate the systematic effects with my model.
In principle it would be possible to determine the instrumental polarization of an optical train by calibration measurements only: sufficiently bright sources with zero polarization, with linear polarization at 0° ($U = 0$), with linear polarization of an angle close to 45° ($U \neq 0$), and with significant circular polarization (or simply four linearly independent Stokes space elements) would provide the necessary information to solve the equations for the matrix elements. In practice it is not feasible to measure four sources for every parallactic angle, rotator position, and both optics, and in particular it is not possible to measure the Stokes parameter V. However, the results of the presented model can be compared with the small number of available and suited standard observations in the ESO archive. In this way it is much easier to obtain a calibration of the IP.

3.8.1. The data

In order to gauge the model for the instrumental polarization I have to test the predictions of the model against standard star observations. In the data archive of ESO plenty of standard star observations are available, mainly of unpolarized standards. Most of these data are difficult to handle because of bad weather conditions, insufficient brightness, or the small number of frames that have been observed. Furthermore polarimetric measurements at different angles have been obtained for these standards by turning the whole instrument instead of the HWP, which changed the IP. Thus, in these cases Q and U have been measured with different instrumental setups. However, three unpolarized stars turned out to be suited to be compared with the prediction of my model.

A fourth, the standard RCra88, was even observed with the same observing strategy as Sgr A*. This star has been studied by Whittet et al. (1992), and it shows a K-band polarization of $(1.8 \pm 0.1)\%$ at $(95 \pm 1)^\circ$.

The available polarimetric standard star data in the archive do not include longer light curves, which would allow us to investigate the position dependency of the instrumental polarization. For this purpose I used bright stars in the IRS16 cluster of the Galactic Center that were observed with a time sampling of about 4 min for Stokes parameters I, Q, and U.

In order to finally test the systematic effects of different calibration methods on the polarimetric light curves of Sgr A*, I investigated three of the brightest polarized flares in the framework of the new method. All data sets used for this thesis were taken in the Ks-band and are listed in Table E.

For the GC observations the infrared wavefront sensor of NAOS was used to lock the AO loop on the NIR bright (K-band magnitude ~ 6.5) supergiant IRS 7, located about $5.6''$ north of Sgr A*. For the standard RCra88 the AO was locked on the target itself. For all other standards the AO loop was open.

During the observations the atmospheric conditions (and consequently the AO correction when the loop was closed) were stable enough for high angular resolution photometry and polarimetry (typical coherence time > 2ms). The exposures were jittered by a few arcseconds. All frames were sky-subtracted, flat-fielded, corrected for bad pixels, and aligned with sub-pixel accuracy by a cross-correlation method (Devillard 1999). For the GC observations point spread functions (PSFs) were extracted from the individual frames with StarFinder (Diolaiti et al. 2000), the images were de-convolved with the Lucy-Richardson (LR) algorithm (which is necessary to counter source confusion and crowding), and a beam restoration was carried out with a Gaussian beam of a FWHM corresponding to the resolution at $2.2\mu m$ (~ 60 mas).

As a preparation for the differential measurements, all channels were aligned to each other on subpixel-scale. Flux densities were measured by aperture photometry. The radius of the apertures for the de-convolved GC data was about 40 mas (3 pixels, S13), about 270 mas (20 pixels, S13) for the isolated RCra88 and about 600 mas (22 pixels, S27) for all other standards. Because of the channel alignment the positions of the apertures were the same for all channels. As a correction for background flux I subtracted the flux measured in apertures where no apparent source is located for each channel. Total intensity for the light curves was obtained by adding the flux of the orthogonal channel and applying a flux density calibration as described in Zamaninasab et al. (2010). The polarimetric parameters Q and U were then obtained according to Eq. (3.5).

Source	P [%]	ϕ [deg]	$\lvert\text{model} - \text{data}\rvert$ [%]
RCra88	1.8	95	(0.2 ± 0.2) $(Q\&U)$
WD1344	0	–	(0.3 ± 0.2) (Q)
WD2039 – 202	0	–	(0.3 ± 0.2) (Q)
HD109055	0	–	(0.3 ± 0.2) (Q)

Table 3.3.: Standard stars. Reference polarizations of the standard stars and systematic deviation of the data from the model. For RCra88 the data allowed me to compare both parameters Q and U. For all other standards only the differential flux of the orthogonal channels (equivalent to Q) for different instrumental setups could be tested.

3.8.2. Gauging the model: standards and IRS16 stars

The GC observations and the measurement of RCra88 used the Wollaston-HWP setup, whereas for all standard-star observations NACO itself was rotated for the different angles. In the former case it was possible to compare the data (after correcting for the IP of CONICA by the flat-field as described in 3.6.2 and for the offset of the HWP) in Q and U with the predictions of the model. In the latter case the IP was different for the different angles of the instrument rotation. Thus, a measurement of Q and U under the same circumstances is not available. In these cases I computed the expected difference between the fluxes of both channels for each frame and its instrumental setup and compared it with the data (i.e. I considered each frame as a measurement of Q with a different instrumental setup). For all polarimetric standards the model agrees with the observations with an accuracy of below 0.5 % (in Q and $Q\&U$ respectively). The standard stars, their reference polarizations (degree and angle), and the systematic deviation of the model from the differential fluxes in the observations are given in Table 3.8.2. The uncertainty of this systematic error was determined taking the median deviation of the data, i.e. the statistical error of the measurements.

The description of the position-dependent part of the IP can be tested with the long light curves of bright IRS16 sources from 2009. Here a comparison revealed that k^{alu} and δ^{sil} had to be slightly adjusted to match the shape of the observed light curves in Q and U as described in the captions of Fig. 3.5. This excursion from the default material constants is within the typical tolerances and can probably be explained with an aging of the aluminum coating. The time-dependency of the model and the data for Stokes Q and U excellently agree with each other. Since the apparent[6] polarization of sources at the GC is not known with the accuracy of standards, the apparent polarization parameters of these sources are considered to be the free parameters of the fits.

[6]By "apparent" polarization here and below I mean the polarization that an ideal instrument would measure. The polarization of the stars discussed here is dominated by the interstellar medium.

Fig. 3.11 shows model and data for IRS16C (In Figures E.1 I show the same model vs. data comparison for IRS16NW, IRS16CC, and S67). In this figure Q (blue) and U (green) parameters are shown as a function of hour angle. The solid line is the best χ^2-fit of the model to the 2009 data that is already corrected for the HWP offset (upper panel). The lower panel shows the data corrected for the full instrumental polarization. The solid line here describes Q and U corresponding to the apparent polarization of the source. The big difference between the measured and the corrected U parameter results mainly from the opposite sense of rotation of the HWP with respect to the sky. The larger deviation of the model from the data points at the beginning of the night are due to the weather conditions and the AO performance, which were not as stable as later. The fitting of the model is weighted toward the end of the night.

For all four fitted sources the errors of the single data points are about 0.3% for Q and U and $\chi^2/\mathrm{dof} = 1.1$, where p and ϕ (apparent polarization), and k^{alu} and δ^{sil} (material constants, see Table 3.5) are considered to be the free parameters. The apparent polarizations as best χ^2 fitting results are listed in Table 3.8.2 for all four IRS16 sources obtained from 2009 data. In this table the error of the polarization degree is about 0.8%, the error of the angle about 3°. For comparison I list the results of Ott et al. (1999). Here p has in average an error of 2%, and the angle uncertainty is about 18°. Additionally I give the average polarization of the central arcsecond around Sgr A* for stars with $m_{\mathrm{Ks}} \geq 13$. Stars of this brightness in the near surrounding of Sgr A* have commonly be used as calibration stars for the "boot strapping" calibration described in section 3.9.2. I emphasize that to my knowledge the results presented here are the first polarimetric measurements of sources within the central pc of the GC since Knacke & Capps (1977) that are independently calibrated with a method that goes beyond "boot strapping" procedures (see section 3.9.2). The polarization of the sources in Table 3.8.2 compares well with the polarization found by Knacke & Capps (1977) for the central region of the GC and can therefore be explained by the galactic foreground polarization as discussed in Knacke & Capps (1977) and Ott et al. (1999).

The presented model enables us to correct the IP with an accuracy better than 1% in polarization degree and better than 5° in polarization angle for polarization degrees $\geq 4\%$. These errors are deduced from the light curves of the IRS16 sources that exhibit comparably small statistical errors for Q and U, and the systematical deviation of Q and U of 0.4% for the standard stars (see Table 3.8.2). The time variability (i.e. the relative behavior) of the IP in polarization degree can be described with an accuracy of a few tenths of a percent. Thus, after correction of the IP, remaining variability with amplitudes of 1% or more in linear polarization is caused by intrinsic variability and statistical errors and is not a feature of the IP.

Source	This thesis		Ott et al. (1999)		m_{Ks}
	P [%]	ϕ [deg]	P [%]	ϕ [deg]	
IRS 16C (S96)	4.6	17.8	4.0	35	9.55
IRS16CC	5.4	15.5	6.1	54	10.15
IRS 16NW (S95)	5.9	12.0	4.6	24	9.86
S67	5.2	17.8	–	–	12.10
central arcsec	5.3	27			

Table 3.4.: Apparent polarization of sources at the GC. K-band magnitudes are taken from Ott et al. (1999) and Gillessen et al. (2009).

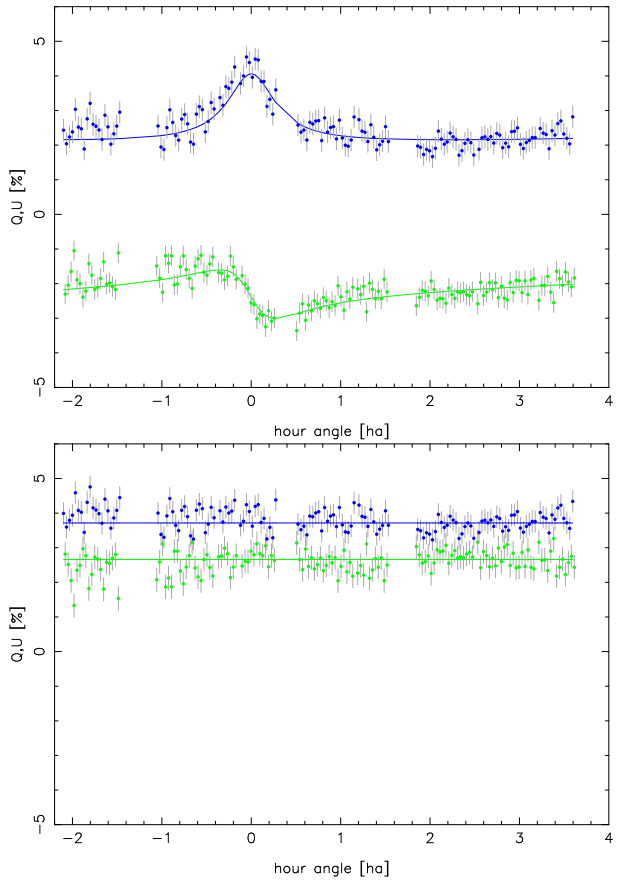

Fig. 3.11.: Q (blue) and U (green) parameters as a function of time for IRS16C. The lower panel shows the data corrected for the full instrumental polarization.

3.9. Comparison of different calibration methods

In this section I describe two other common calibration methods. I investigate their ability to correct the IP of NACO. Both calibration methods have shortcomings, and I give a quantitative analysis of the remaining systematic errors. I investigate the influence of the "boot strapping" method that was commonly used for calibrating light curves of Sgr A* on the evaluation of time series of the polarimetric parameters. But first I discuss the "channel switch" method, which enables me to propose an observing strategy that aims at high-accuracy polarimetry, but not at high-time resolution.

3.9.1. The "channel switch" method

A common method to treat instrumental polarization is to observe orthogonal channels at $0°/90°, 45°/135°, 90°/0°, 135°/45°$. I assume that the IP affects each of the orthogonal channels factorially, and that the particular factor does not change if the instrument is turned by 90°:

$$Q_{0°} = \lambda I(0°) - \sigma I(90°) \text{ and } \mathrm{Q}_{90°} = \lambda \mathrm{I}(90°) - \sigma \mathrm{I}(0°)\,, \tag{3.28}$$

with λ and σ the factors introduced by the IP (for U analog equations). The true Stokes parameters then can be obtained from the difference of the Stokes parameters derived from the corresponding images $0°/90°$ and $90°/0°$, and $45°/135°$ and $135°/45°$ respectively, and with Eq. (3.5) we get

$$Q_{\mathrm{corr}} = \frac{Q_{0°} - Q_{90°}}{I_{\mathrm{tot},0} + I_{\mathrm{tot},90}} = \frac{(\lambda+\sigma)(I(0°) - I(90°))}{(\lambda+\sigma)(I(0°) + I(90°))} = Q \tag{3.29}$$

(for U analog).
The assumption of equal factors in Eq. (3.28) is not appropriate for every case. Obviously the influence of a transmission matrix like Tr of Eq. (3.24) can be fully corrected by "channel switching", whereas for the matrices (3.8) and (3.10) systematical errors remain. To quantify the remaining effects for a given Mueller matrix M I calculated the Stokes vectors

$$S'_{0°} = M \times S \textit{ and } S'_{90°} = M \times T(90°) \times S \tag{3.30}$$

with S the Stokes vector of the incoming light and $S'_{0°}$ and $S'_{90°}$ the measured Stokes vectors of the image pairs $0°/90°, 45°/135°$ and $90°/0°, 135°/45°$ respectively. For matrix (3.8) we find

$$Q_{\mathrm{corr}} = Q \text{ and } \mathrm{U}_{\mathrm{corr}} = \frac{\sqrt{\mathrm{r}_\perp \mathrm{r}_\parallel}\cos(\delta)}{2(\mathrm{r}_\perp + \mathrm{r}_\parallel)}\mathrm{U}\,, \tag{3.31}$$

with Q and U the proper Stokes parameters of the incoming light. For matrix (3.10) we find

$$\begin{aligned} Q_{\rm corr} &= \cos(2p)Q + \sin(2p)U \text{ and} \\ U_{\rm corr} &= \cos(2p)U - \sin(2p)Q\,. \end{aligned} \tag{3.32}$$

That is, a rotation of the angle reference as the one caused by the HWP offset cannot be corrected at all, while for a metallic reflection U is still affected by a factor that depends on the material constants.
Furthermore this method can only correct instrumental effects for the part of the instrument that is rotated by 90°. Because in our case the rotated part is the analyzer (a rotation of the HWP is equivalent to a rotation of the analyzer), this procedure only corrects for the IP of the light train after the HWP. Another possibility is to rotate NACO with the rotation adapter as a whole, as was done for a number of observations in the ESO archive. In both cases the IP of M3 remains uncorrected. Nevertheless, using the "channel switch" method, the effects of the analyzer and the flat-fielding, which are difficult to quantify as described in section 3.6, and even parts of the IP of NAOS can be eliminated. I propose the following strategy.
To archive the best attainable accuracy I propose to realize the 45°-switching between Q and U with the HWP, and the 90°-switching with a rotation of the entire instrument (NACO). I now consider only the effects after M3, i.e. the system $\mathrm{Tr} \times \mathrm{T}(-\beta) \times \mathrm{T}(90°) \times \mathrm{M_{NAOS}} \times \mathrm{T}(-90°)$. Then the numerical analysis shows that Eq. (3.29) gives

$$\begin{aligned} Q_{\rm corr} &= 0.894Q - 0.387U \\ U_{\rm corr} &= 0.447Q + 0.775U\,. \end{aligned} \tag{3.33}$$

The situation gets much easier if we measure at offset corrected angles (without HWP offset, the angles can be obtained from Table 3.4.3). Then we get

$$\begin{aligned} Q_{\rm corr} &= Q \\ U_{\rm corr} &= 0.865U\,. \end{aligned} \tag{3.34}$$

Here we just have to additionally correct for the factor in U and the IP of M3, which reduces the number of free parameters of the model to 3. The effects of all the parts after M3 can be reduced like this to one factor.
This method in particular eliminates the mentioned uncertainties of the parameters of the analyzer. Since the description of the parallactic angle-dependent part caused by M3 proved to be very accurate (a few tenth of a percent in polarization degree) in comparison to the remaining systematic deviations between model and standards (about 1% in polarization degree), I expect that the proposed method will allow us

to improve the accuracy by about a factor ten. I want to investigate this in future calibration runs. I emphasize here that the "channel switch" method needs more than twice the time to obtain one set of Stokes parameters and is not suited for Sgr A* and its fast variability with time scales down to a few minutes. Another disadvantage is the restriction of the field-of-view, which is caused by the rotation of NACO with the rotation adapter.

3.9.2. The "boot strapping" method

For time-resolved measurements in the crowded Galactic Center field we have commonly used a "boot strapping" method to calibrate the polarization data (e.g. Eckart et al. 2006a,c, Zamaninasab et al. 2010). This method has also been successfully applied to wire-grid data (e.g. Eckart et al. 1995, Ott et al. 1999). In the presence of crowded fields with many weakly and only a few strongly polarized sources, it has the advantage of being applicable without the availability of extensive data on calibrator sources. Below I describe this method and investigate its uncertainties in detail.
For the polarimetric "boot strapping" calibration of the light curves of Sgr A*, each channel is flux-density-calibrated with reference stars in a region of 2 arcseconds diameter surrounding Sgr A* assuming total intensity brightness for each star. The sums of the orthogonal channels for 0° and 45° are averaged and taken as total intensity. With this total intensity and the galactic foreground polarization of $4\%@25^\circ$ (Knacke & Capps 1977) one obtains with Eq. (3.3) the expected flux densities for each star and channel. These flux densities are then compared with the time-averaged fluxes of the light curves of each star and channel, and a correction factor for each channel is obtained by averaging over all stars. Following this procedure the stars in the near surrounding of the GC show in average the foreground polarization and every source with similar polarization is calibrated. The value of $4\%@25^\circ$ is an average for the sources toward the central arcsecond that has been measured by Knacke & Capps (1977) with arcsecond resolution. I could confirm this measurement by my independent calibration, which results in an average of $5.3\%@27^\circ$ for the central arcsecond (Table 3.8.2), which is equivalent within the errors.
By using this calibration procedure one assumes that the IP affects the measurement by introducing different weighting factors to the flux measurements of the four polarimetric channels, very similar to the assumption in Eq. (3.28). Here these factors are considered to be independent of the polarization of the considered source (whereas the factors for the "channel switching" are assumed to be independent of an instrument rotation). In particular it cannot correct for an angular offset like the one caused by the HWP if the calibrator's polarization angle is significantly different from the polarization angle of the source one aims to calibrate (this offset corresponds to a $Q \leftrightarrow U$ cross

talk, and the correction factors for each channel in this case depend on the direction of the linear polarization). I intend to answer the question of how this systematic error of the "boot strapping" calibration influences the variability of the polarimetric light curves of Sgr A*.

First I investigate the systematic errors for a theoretical light curve pattern as deduced in Zamaninasab et al. (2010) for a polarized orbiting hot spot in an accretion disk around Sgr A*. In Fig. 37 of Zamaninasab et al. (2010) an apparent view of a hot spot in a Keplerian orbit at the innermost stable circular orbit (ISCO) of a spinning black hole (with spin parameter of 0.5) is shown. The model predicts that the observer witnesses a magnification in flux according to lensing and boosting effects. The polarization angle on the observer's sky sweeps shortly before the total flux reaches its maximum, while the degree of polarization follows this maximum (Fig. 3.12). The existence this a pattern is an indicator for the strong gravitational regime and can be used as a tool for measuring the spin of a black hole (Zamaninasab et al. 2010). While this model predicts the described pattern as a function of the normalized orbital time scale, I here set the orbital time scale to 30 min (as observations of Sgr A* suggest) and the center of the pattern (here at t=15 min) to hour angle zero, where the variability of the IP is strongest. I compute the Stokes vector for a source that shows the apparent polarization through the foreground of 5.3%@27° (see Table 3.8.2), apply the Mueller matrix for NACO to this vector, and deduce the normalized flux in each channel. These fluxes are then compared with the expected fluxes for a source of 4%@25° (without IP) as assumed in previous publications (e.g. Zamaninasab et al. 2010, Meyer et al. 2006b). For each time the obtained correction factors are applied to the channel fluxes that have been calculated from the theoretical polarization pattern; this pattern had to be transformed before with M_{NACO} to describe the actual measurement at the detector as predicted by my IP model.

The resulting light curves are shown in Fig. 3.12. The peak values of the polarization degree are systematically underestimated by about 10% at an expected peak of 70%. Typical deviations are on the order of $<5\%$ for the degree of polarization and $\leq 13°$ for the polarization angle. However, the angle mainly shows the expected HWP offset of about 13°, while other polarization effects of the instrument have much smaller influences. Indeed, the resulting light curves look very much the same if the simulation only takes the HWP offset into account. For very low polarization degrees the angle is ill defined. At these states real data with white noise contribution do not allow for detecting significant polarized flux, and therefore the interpretation of the polarization angle is not possible in either way. The overall behavior of the variability is conserved. A compensation for the HWP offset during observations would eliminate almost all the effects introduced by this calibration method.

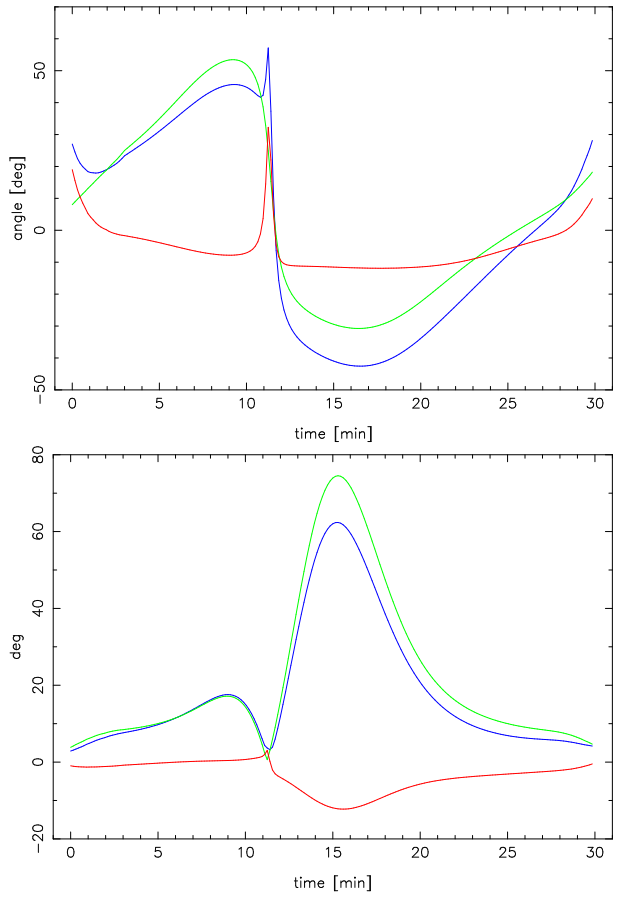

Fig. 3.12.: Simulation of systematic calibration artefacts in light curves. The green curves show a typical pattern for polarization degree and angle as a function of time (Zamaninasab et al. 2010). The blue curves show the same data calibrated by the described “boot strapping” method. The difference between both is displayed in red.

3.9.3. Effects on time-resolved polarimetric measurements of Sgr A*

As a final step I investigate the difference of the calibration methods with respect to the observed polarimetric data of Sgr A*. For comparison a proper error estimate of the individual data points is needed. For the common "boot strapping" method the error was deduced from (1) the statistical variations of a comparison star near Sgr A* for each channel after flux density calibration, and (2) the standard deviation of the correction factors for the calibration stars. This was performed by Gaussian error propagation for p and ϕ. Since the new calibration does not include a flux density calibration, one has to estimate the statistical error of the photometry from the ADU (analog to digital conversion units) counts of a comparison star. Here it is important to first eliminate the correlated fluctuations of both orthogonal channels. This is achieved by subtracting one channel from the other after scaling the subtracted channel in a way that the averages of both channels are the same[7]. The standard deviation of this difference is a good error estimate for the difference in flux between both channels (and the total flux as well), and can be propagated again.
As a result I obtain Figures 3.13, E.2, and E.3. In general both calibration methods show very similar results within the statistical uncertainties of the measurements. The new calibration shows a trend toward smaller polarization degrees, and the polarization angle shows a small systematic offset as discussed. Generally, the polarization angle is not well defined for small degrees of polarization. The comparisons in Figures 3.13, E.2, and E.3 show that for total Ks-band intensities above 4 mJy and polarized fluxes above 1 mJy the results of both polarization calibration methods are virtually identical. Only states of Sgr A* that agree with these conditions have been interpreted in the framework of a relativistic modeling (Zamaninasab et al. 2010, Eckart et al. 2006c, Meyer et al. 2006b,a).

3.10. Summary

I summarize the results of this second part of my thesis:

- I presented a detailed analysis of the polarization calibration of the ESO VLT NAOS/CONICA system in the Ks-band. Using the Stokes/Mueller formalism for metallic reflections I introduced a polarization model of the camera/telescope system that excellently agrees with the measurements obtained on calibrator sources and sources in the Galactic Center. I can qualitatively and quantitatively reproduce the instrumental polarization and show that a polarization angle offset

[7]For comparison stars of low polarization the scaling is not crucial.

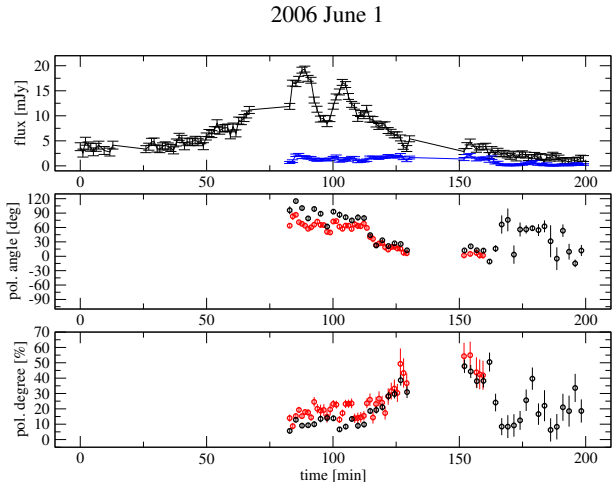

Fig. 3.13.: Total intensity (upper panel), polarization angle (middle panel), and polarization degree (lower panel) of Sgr A* as a function of time (2006 June 1). The black data points are the result of the new calibration method, the red points are obtained by the previously used "boot strapping" method as published in Zamaninasab et al. (2010). The blue points show polarized flux ($p \times I$). The meridian transit occurred at 32.4 min, 50.4 min before the polarimetric measurements started.

of $(13.2 \pm 0.3)^\circ$ has to be taken into account for NACO data observed before autumn 2009. The IP in Ks-band amounts to a maximum of 4%.

- The model presented here enables us to correct for the instrumental polarization of NACO. My investigation shows that for sources with statistical errors in Q and U significantly smaller than 0.5 % the polarization can be measured with an accuracy of better than 1% in polarization degree. The accuracy of the polarization angle in these cases is $\leq 5^\circ$ for polarization degrees $\geq 4\%$. For weaker sources like Sgr A* the accuracy of the polarization measurements is dominated by the statistical errors.

- I showed that the "boot strapping" method, which can efficiently be used in the crowded Galactic Center field, yields the same results within the statistical uncertainties (in bright flare phases with flux densities above 4 mJy) when compared to the more exact and elaborate polarization model.

- My approach allows us to extend the description of the IP to other wavelengths easily. It can also be applied to other telescopes and Nasmyth focus instruments. Additional calibration observations may allow for an even better accuracy, and I proposed a calibration strategy that probably will reach an accuracy of a few tenths of a percent in the future.

4. Conclusions and perspectives

In this thesis I have investigated the flux density variability of the Galactic Center source Sgr A* in the near-infrared Ks-band. I concentrated both on the instrumental prerequisites for an analysis of the source intrinsic properties and on a phenomenological, statistical description of the flaring activity. While for the total intensity measurements I found no indication for the two state variability model proposed by Dodds-Eden et al. (2011), my analyses of the instrumental polarization of NACO and of the calibration methods for polarimetric data strengthen the evidence for a signature of strong gravity in the polarimetric light curves of Sgr A*. The statistical simulations of total intensity light curves clearly show that it is indeed possible to explain the existence of rare, bright outbursts and the variability at low flux densities with the same random process. With this model predictions for very high flux states as statistical extreme values and for the long term behavior of the fluctuations can be made, and a bright flare as required to explain the X-ray emission from the surrounding molecular clouds as a light echo is well within the expectations.

The idea that extremely bright flares occur as extreme values of a statistically relaxed process can be seen as an alternative to the explanation by extraordinary feeding events of the black hole that would cause a change of the source properties and the variability statistics, in particular of the stationarity of the random process. However, such events may occur: Freitag (2003) found that for Milky Way type galaxies the probability of an interaction between a super massive black hole and a main-sequence star, a white dwarf and a neutron-star or stellar black hole is of the order of 10^{-5}, 10^{-7} and 10^{-8} events per year, respectively. The orbital decay and a possibly significant mass transfer may last for several months or even years before the actual merger (e.g. Capozziello et al. 2009), such that as a consequence significantly enhanced accretion rates and flashes are likely to be observed. It is also speculated that these merger events actually contribute significantly to the mass content of SMBH accretion disks. The flux densities associated with these merger events are appreciable (two cases for which this phenomenon has recently been discussed are Swift J2058.4+0516 at $z = 1.2$, Cenko et al. 2011; Krolik & Piran 2011; and Swift J1644+57 at $z = 0.3$, Metzger et al. 2012). It can also not be excluded that an increase in the accretion rate and therefore an increase in luminosity can be caused by encounters with members of the central stellar cluster as proposed by Gillessen et al. (2012). The authors report an encounter of a

gas cloud toward Sgr A*, which possibly will start to fall into the accretion zone of the black hole in the next few months.

Within my statistical model the concept of a "quiescent state" and the differentiation between continuous variability and "off" states (as investigated by Dodds-Eden et al. 2011) turn out to be problematic: Sgr A* in the description of my statistical model is always variable and the probability to find a flux density level of exactly zero is actually zero. But any flux density interval starting with zero is represented with a higher probability than any other interval of the same length, allowing for arbitrarily faint flux density states. So from an observational point of view, this model predicts "off" states due to the instrument dependent limited resolution and sensitivity.

Bright flaring states are not always highly polarized, I found counter examples: e.g. observations from May 2009 show a bright Ks-band flare with low, non-variable polarization. It needs to be statistically investigated, how polarization states and especially the mentioned strong gravity patterns are correlated with flux density. This work is in progress. It is of further interest, how the observed statistics can be used to infer statistical models of the fluctuations at other wavelengths according to the proposed radiation mechanisms and to compare the results to statistical investigations of the observations at these wavelengths. This, however, does not exclude the interpretation of the variability in the framework of relativistic effects within an accretion disc. On the contrary, it appears very fruitful to use relativistic models to create polarimetric random processes by randomization of the input parameters. For this randomization the presented statistics represent constraints, and it needs to be investigated, in what sense this method can provide possibilities to constrain physical properties of the black hole and its accretion and emission processes.

Observations as they have been carried out so far are not well suited to investigate the power spectral density at timescales below 100 min. This, as I have shown, is mainly the result of the night-day interruption of the NIR observations. It is necessary to principally change the experimental approach. In this context the next generation of interferometric instrumentation like GRAVITY will play a key role. Its increased resolution may allow for an astrometrical evidence of moving structures in the accretion disc, making indirect methods based on timing analysis obsolete.

A. Data quality

Here I give an overview about the observation conditions. All plots show the data after quality cut.

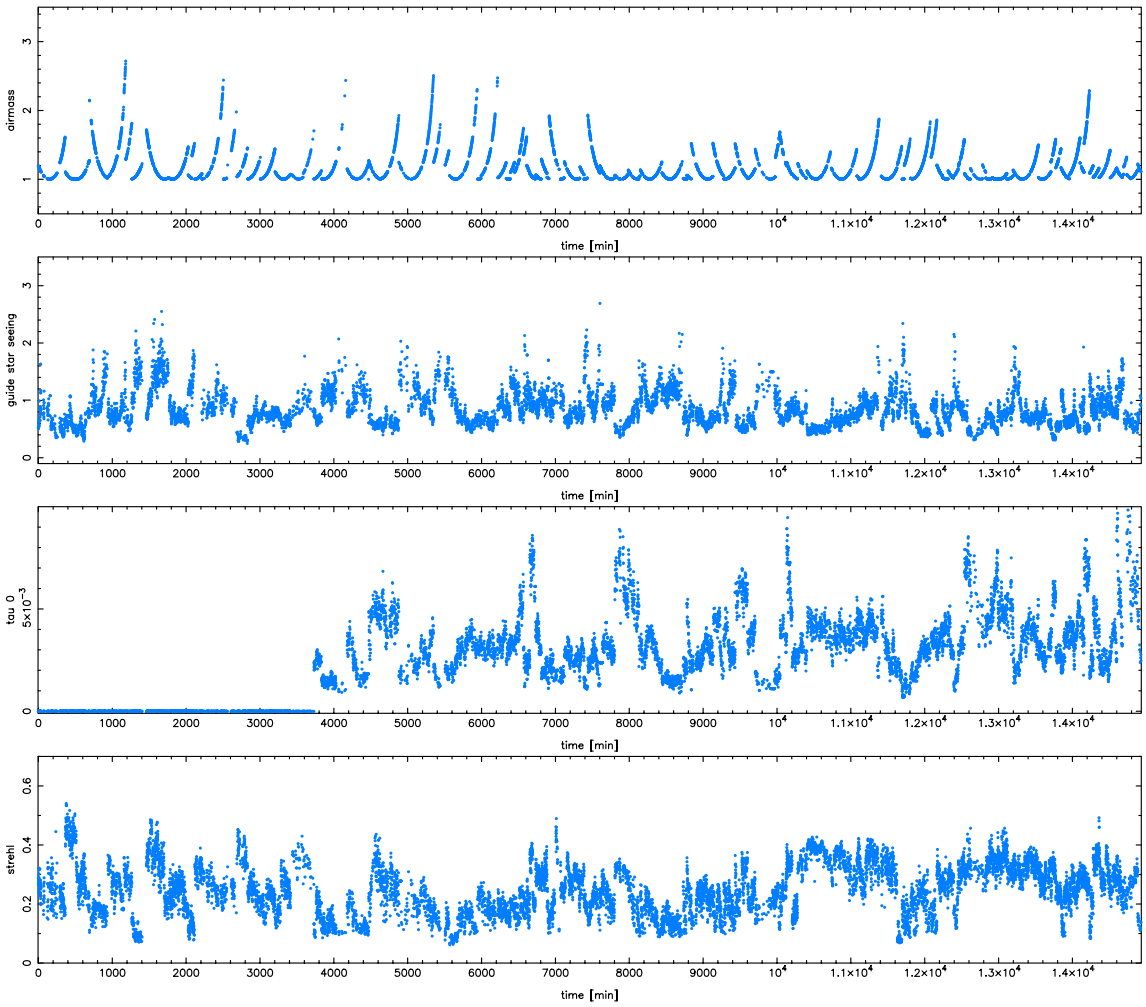

Fig. A.1.: Time series of quality parameters. I show the airmass during observation, the seeing values obtained by a measurement on the active optics guide star, the atmosphere coherence τ_0 (not available for all frames), and the Strehl ratio obtained from the extracted PSF. For a histogram representation see Fig. A.2.

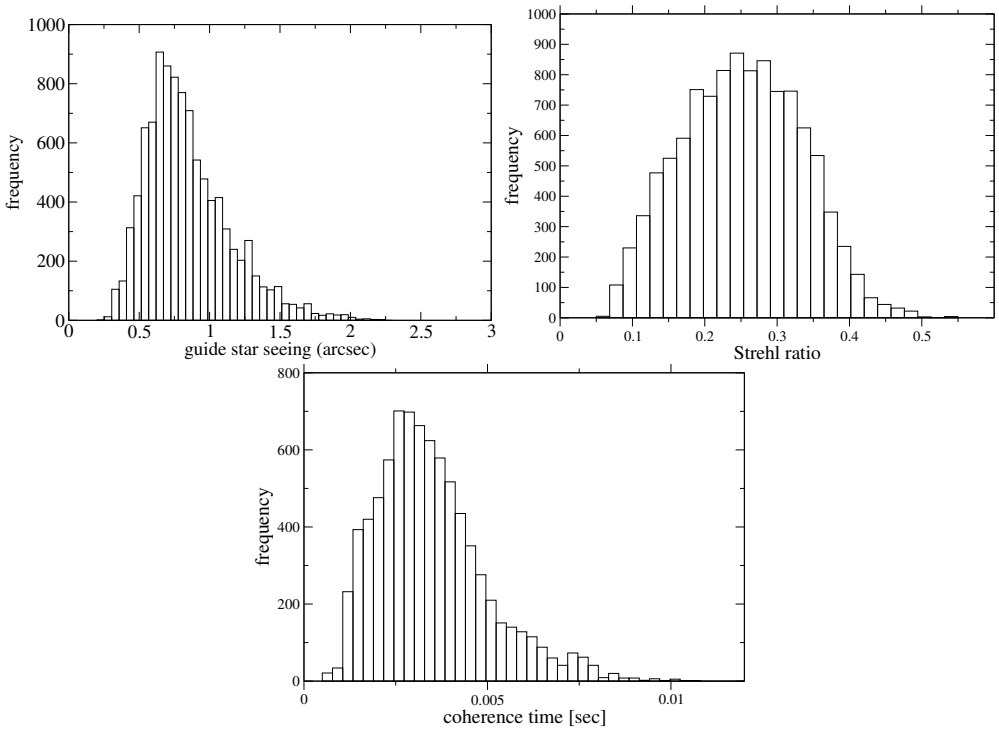

Fig. A.2.: Histograms of the guide star seeing, the Strehl ratio, and the atmospheric coherence time.

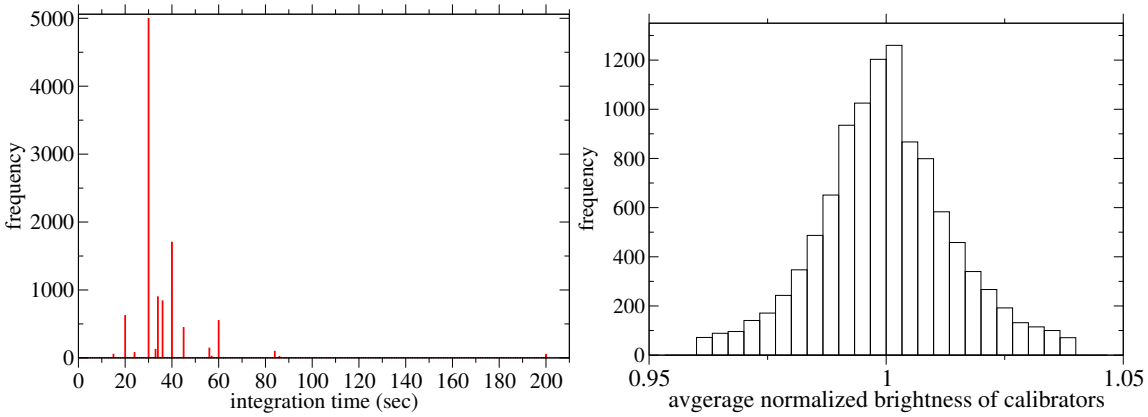

Fig. A.3.: The left panel shows the integration times used for my data sample,the right a histogram of the average calibrator flux densities (see description in section 2.1.2).

B. Light curves

Here I show a more detailed presentation of the data of Fig. 2.2 (blue points). Each box represents a continuous data piece without interruption longer then 30 min. Additionally to the data of Sgr A* I show the light curves of the calibrator S7 (green), of the average calibrator flux density (red), and the average background apertures (b-apertures in Fig. 2.1, grey). Please note that the x-axis is scaled differently, and in the case of the very bright flare of August 5th 2008 the y-axis as well. The missing points of S7 are caused by the rejection algorithm described in section 2.1.2. Since it is very difficult to estimate a reliable error for the individual point due to the changing correction conditions of the AO system and its interplay with the extended background, the confusion and the deconvolution algorithm, I did not include error bars. The point to point scatter of the comparison star and the calibration can serve as an estimate for the individual dataset. The overall error statistics are described in section 2.2.2, and in average I find a Gaussian error of about $\sigma = 0.3$ mJy. Furthermore, I present a Table (Tab. B.1) of all datasets included in this analysis with all important information, including average sampling, length of dataset, and maximum flux density.

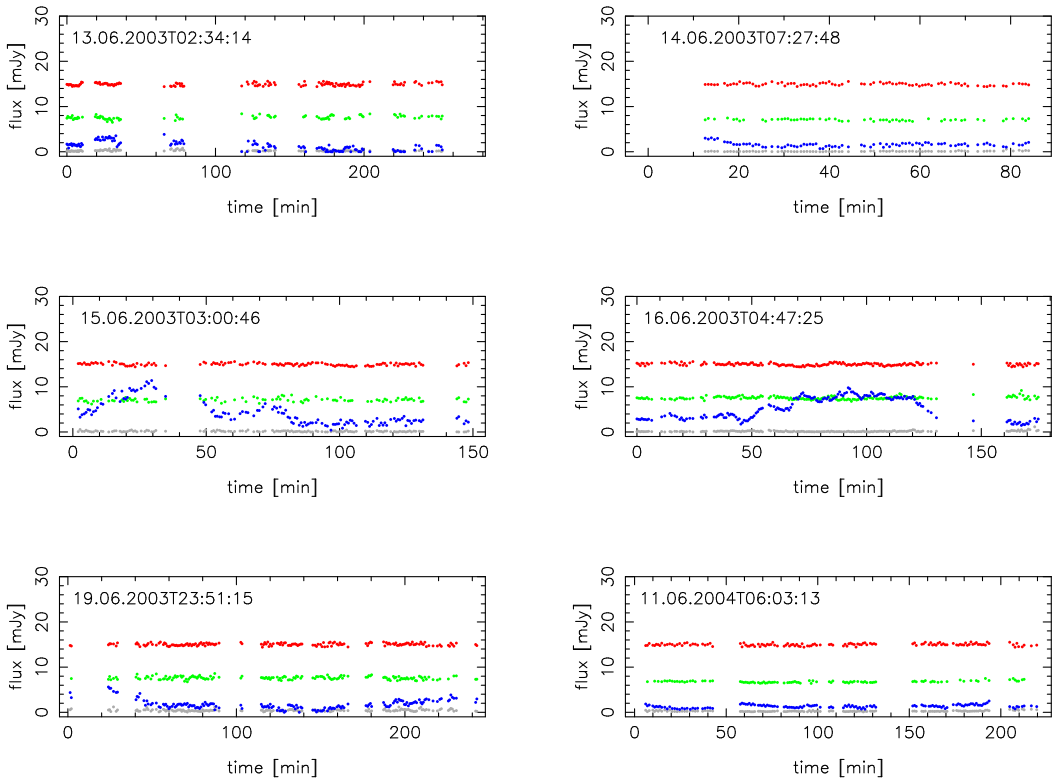
13.06.2003T02:34:14
14.06.2003T07:27:48
15.06.2003T03:00:46
16.06.2003T04:47:25
19.06.2003T23:51:15
11.06.2004T06:03:13
flux [mJy]
time [min]

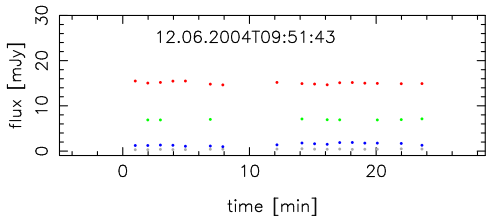
12.06.2004T09:51:43
flux [mJy]
time [min]

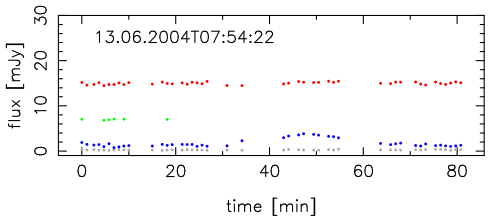
13.06.2004T07:54:22
flux [mJy]
time [min]

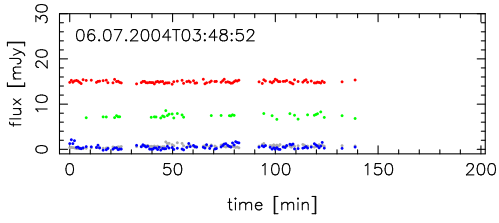
06.07.2004T03:48:52
flux [mJy]
time [min]

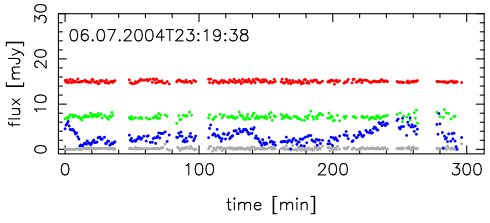
06.07.2004T23:19:38
flux [mJy]
time [min]

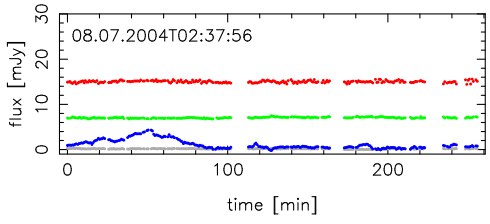
08.07.2004T02:37:56
flux [mJy]
time [min]

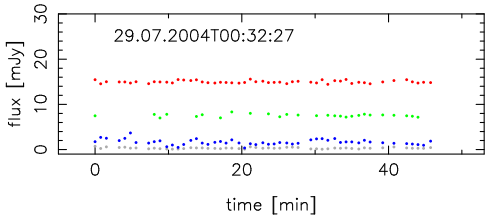
29.07.2004T00:32:27
flux [mJy]
time [min]

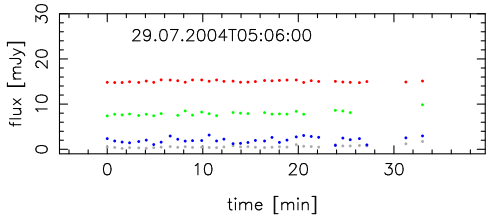
29.07.2004T05:06:00
flux [mJy]
time [min]

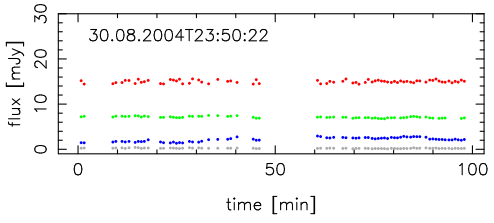
30.08.2004T23:50:22
flux [mJy]
time [min]

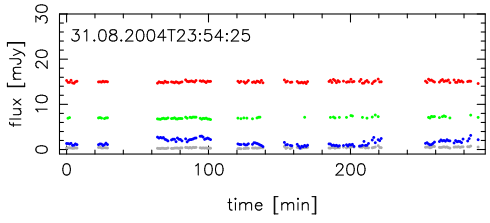
31.08.2004T23:54:25
flux [mJy]
time [min]

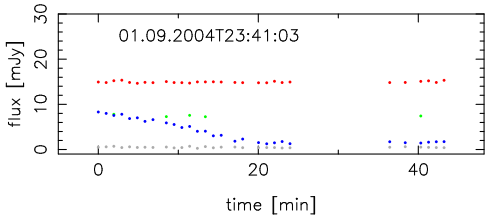
01.09.2004T23:41:03
flux [mJy]
time [min]

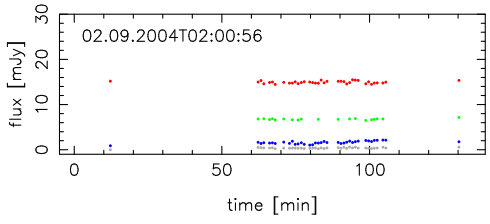
02.09.2004T02:00:56
flux [mJy]
time [min]

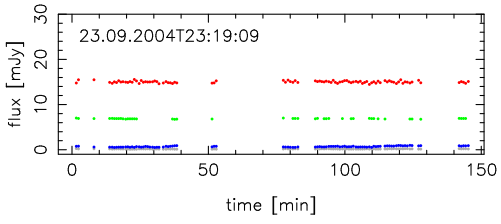
23.09.2004T23:19:09
flux [mJy]
time [min]

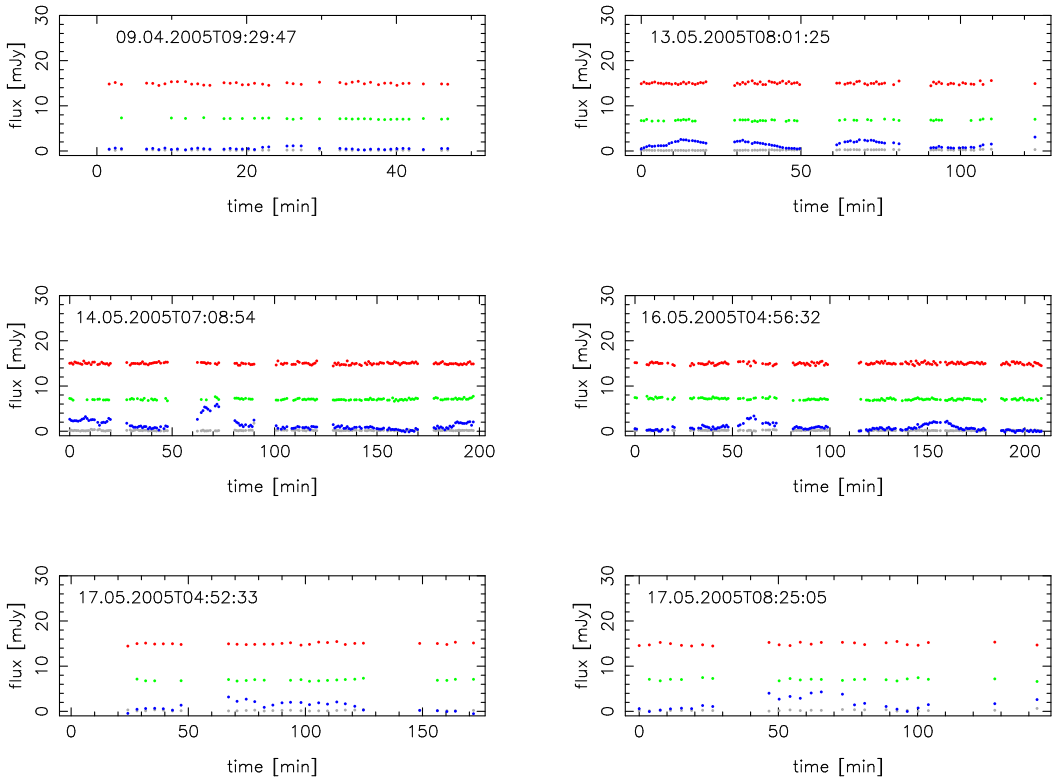
09.04.2005T09:29:47
13.05.2005T08:01:25
14.05.2005T07:08:54
16.05.2005T04:56:32
17.05.2005T04:52:33
17.05.2005T08:25:05
flux [mJy]
time [min]

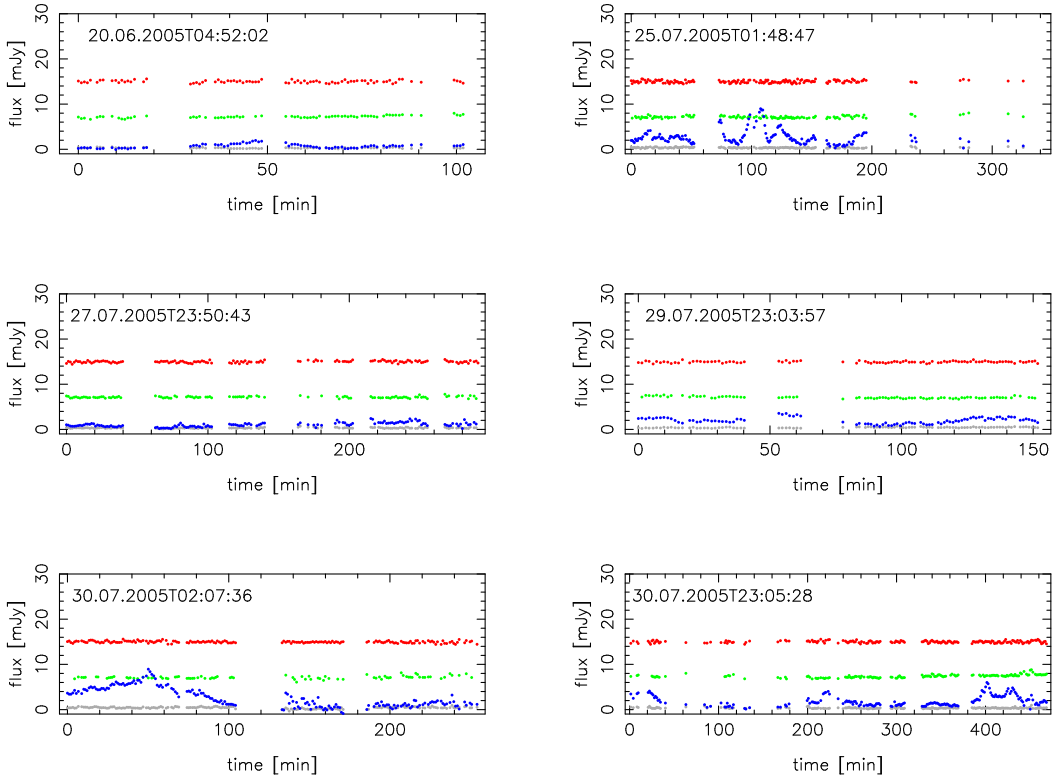
20.06.2005T04:52:02
25.07.2005T01:48:47
27.07.2005T23:50:43
29.07.2005T23:03:57
30.07.2005T02:07:36
30.07.2005T23:05:28
flux [mJy]
time [min]

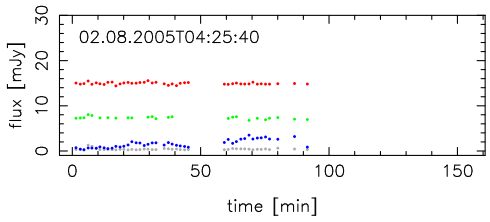
02.08.2005T04:25:40
flux [mJy]
time [min]

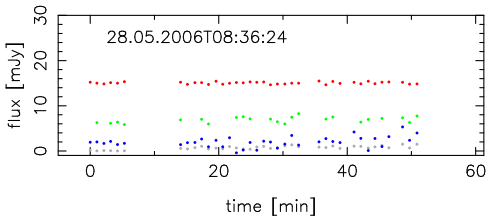
28.05.2006T08:36:24
flux [mJy]
time [min]

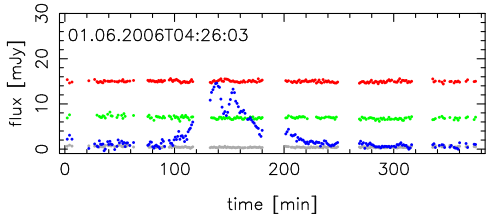
01.06.2006T04:26:03
flux [mJy]
time [min]

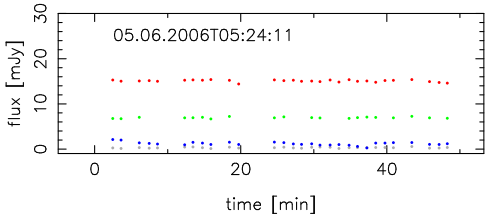
05.06.2006T05:24:11
flux [mJy]
time [min]

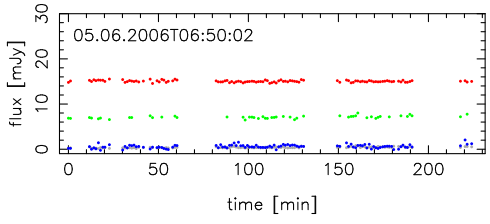
05.06.2006T06:50:02
flux [mJy]
time [min]

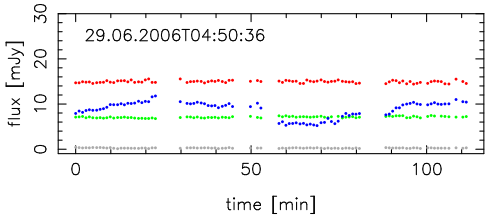
29.06.2006T04:50:36
flux [mJy]
time [min]

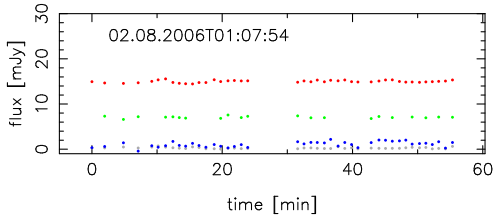
02.08.2006T01:07:54
flux [mJy]
time [min]

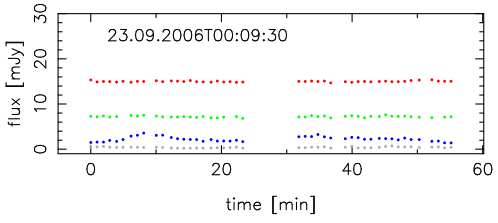
23.09.2006T00:09:30
flux [mJy]
time [min]

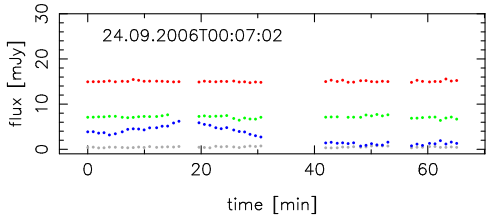
24.09.2006T00:07:02
flux [mJy]
time [min]

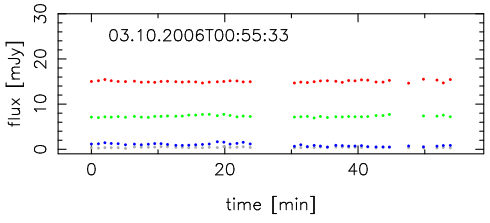
03.10.2006T00:55:33
flux [mJy]
time [min]

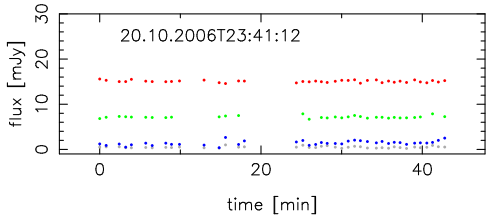
20.10.2006T23:41:12
flux [mJy]
time [min]

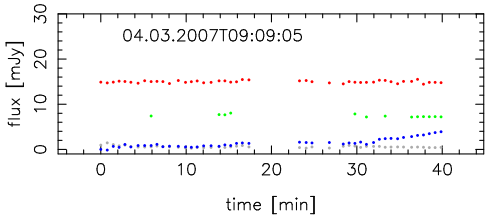
04.03.2007T09:09:05
flux [mJy]
time [min]

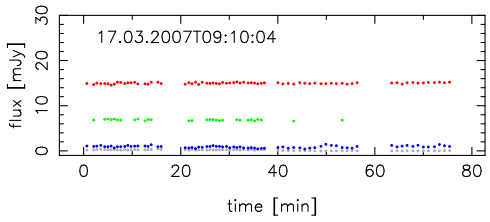
17.03.2007T09:10:04
flux [mJy]
time [min]

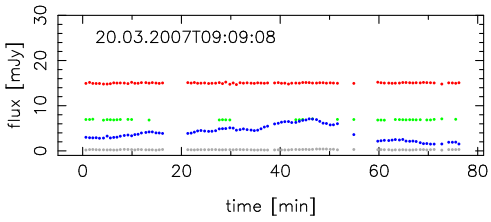
20.03.2007T09:09:08
flux [mJy]
time [min]

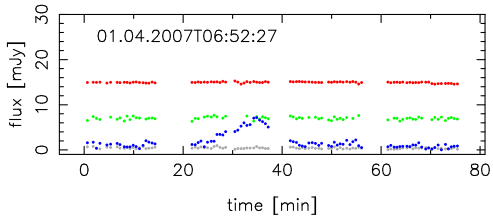
01.04.2007T06:52:27
flux [mJy]
time [min]

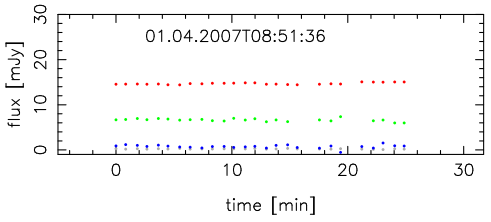
01.04.2007T08:51:36
flux [mJy]
time [min]

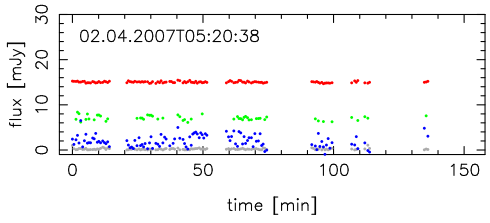
02.04.2007T05:20:38
flux [mJy]
time [min]

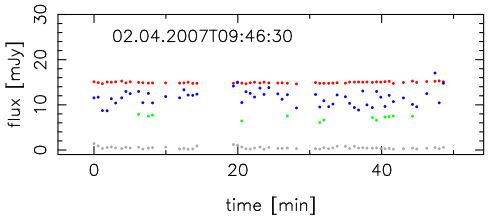
02.04.2007T09:46:30
flux [mJy]
time [min]

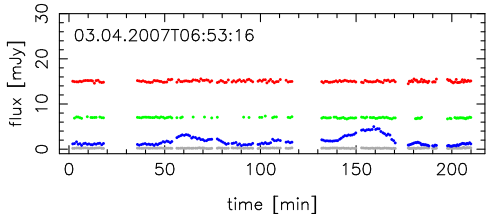
03.04.2007T06:53:16
flux [mJy]
time [min]

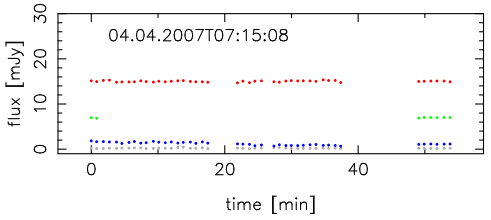
04.04.2007T07:15:08
flux [mJy]
time [min]

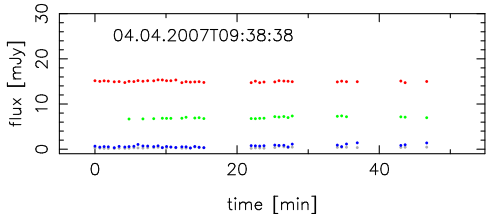
04.04.2007T09:38:38
flux [mJy]
time [min]

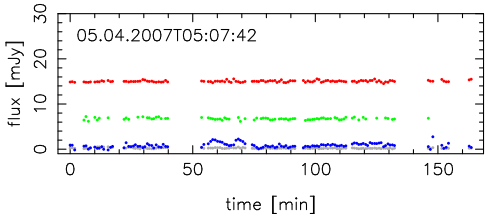
05.04.2007T05:07:42
flux [mJy]
time [min]

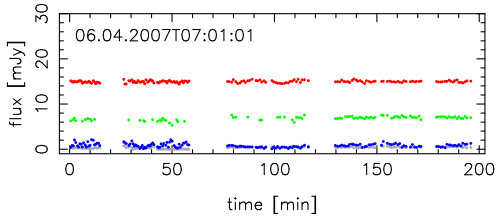
06.04.2007T07:01:01
flux [mJy]
time [min]

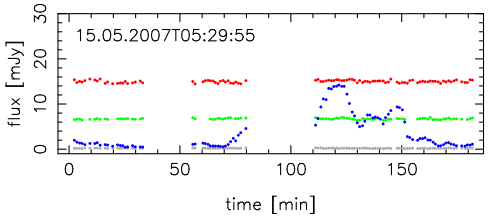
15.05.2007T05:29:55
flux [mJy]
time [min]

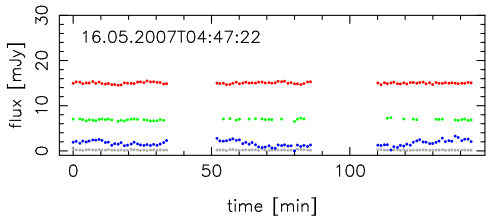
16.05.2007T04:47:22
flux [mJy]
time [min]

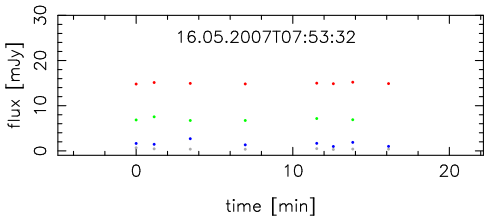
16.05.2007T07:53:32
flux [mJy]
time [min]

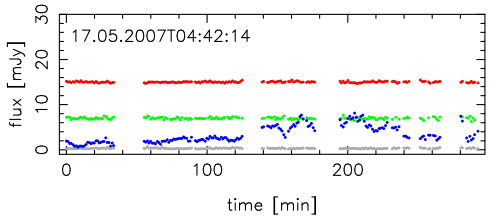
17.05.2007T04:42:14
flux [mJy]
time [min]

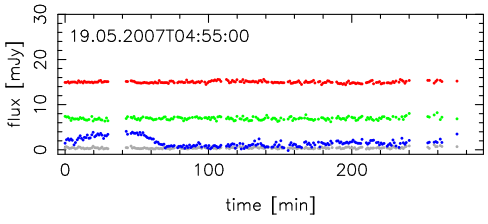
19.05.2007T04:55:00
flux [mJy]
time [min]

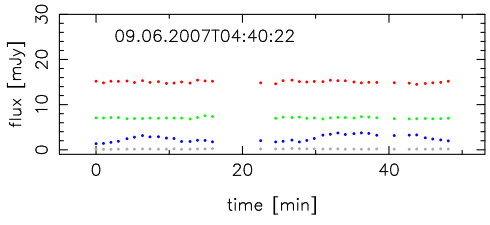
09.06.2007T04:40:22
flux [mJy]
time [min]

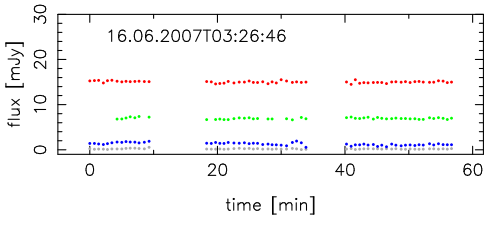
16.06.2007T03:26:46
flux [mJy]
time [min]

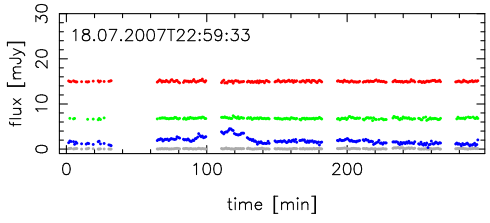
18.07.2007T22:59:33
flux [mJy]
time [min]

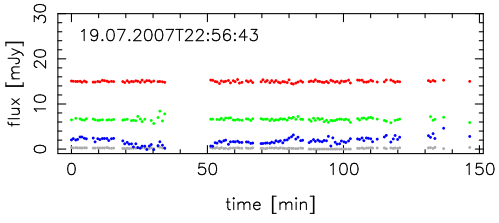
19.07.2007T22:56:43
flux [mJy]
time [min]

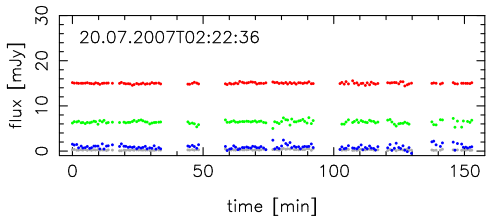
20.07.2007T02:22:36
flux [mJy]
time [min]

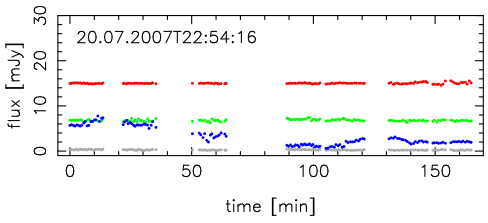
20.07.2007T22:54:16
flux [mJy]
time [min]

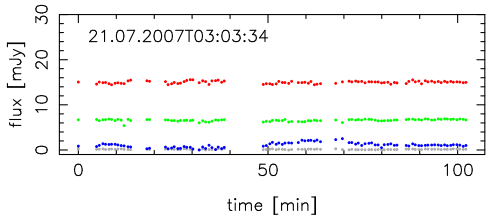
21.07.2007T03:03:34
flux [mJy]
time [min]

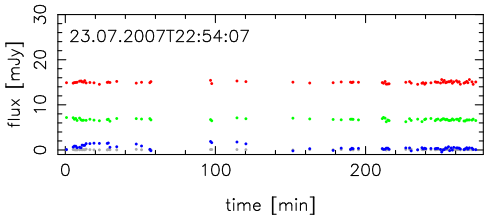
23.07.2007T22:54:07
flux [mJy]
time [min]

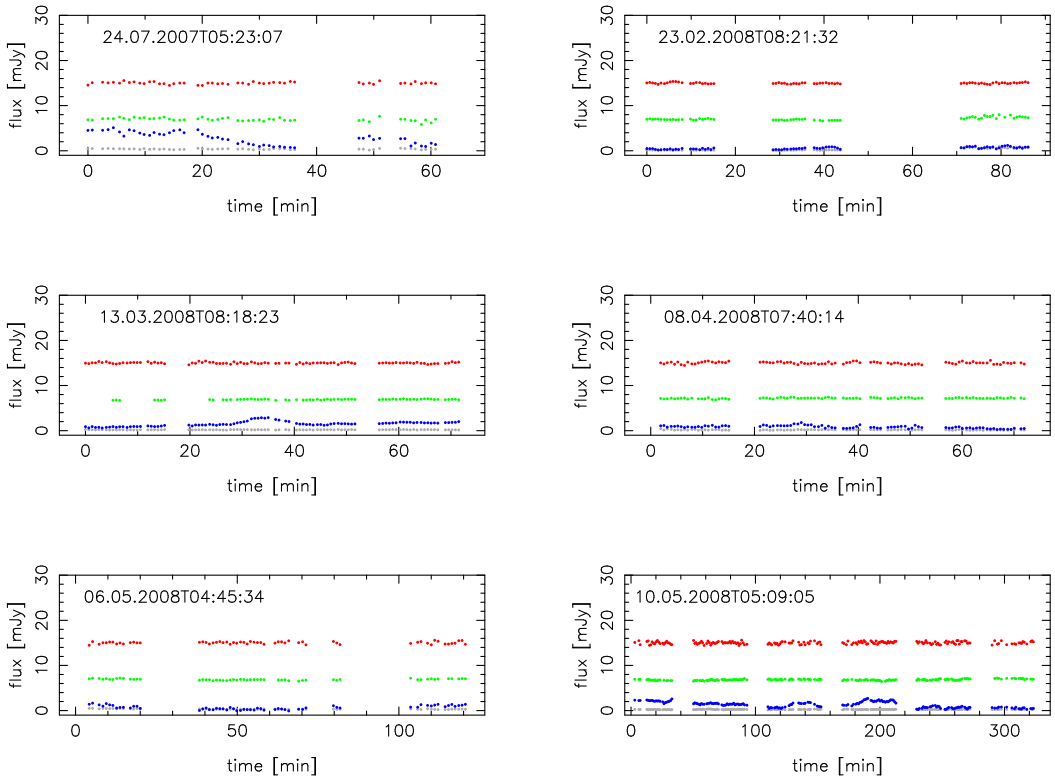
24.07.2007T05:23:07
23.02.2008T08:21:32
13.03.2008T08:18:23
08.04.2008T07:40:14
06.05.2008T04:45:34
10.05.2008T05:09:05
flux [mJy]
time [min]

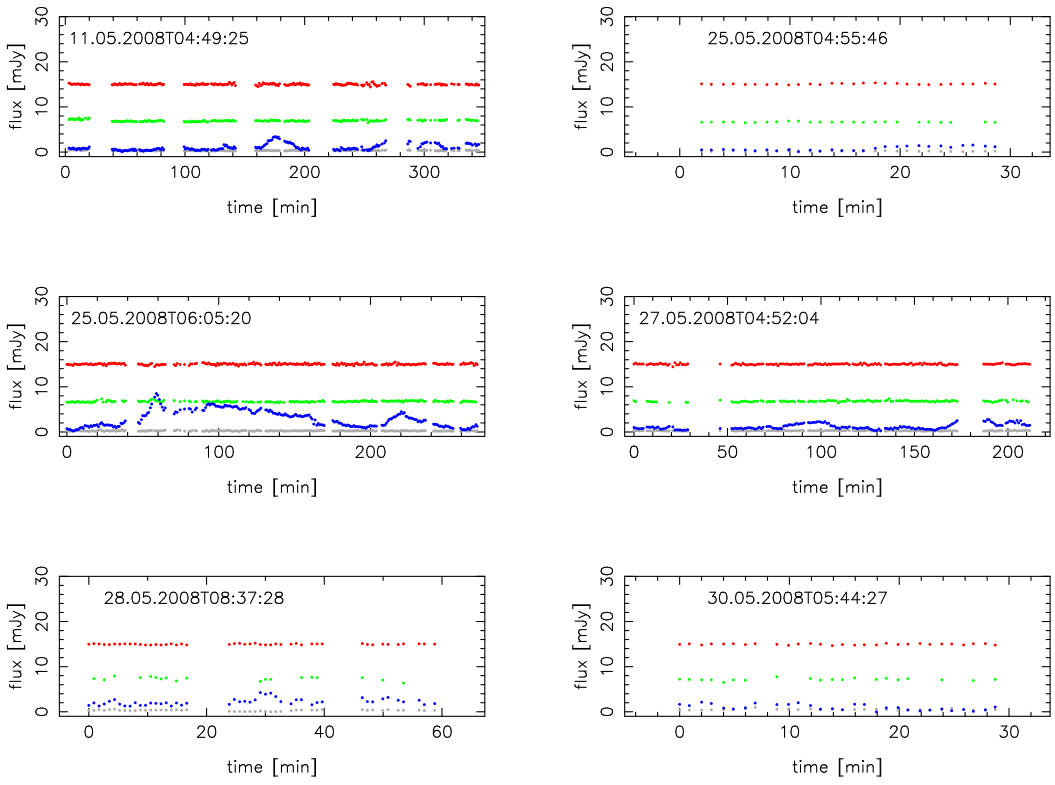
11.05.2008T04:49:25
25.05.2008T04:55:46
25.05.2008T06:05:20
27.05.2008T04:52:04
28.05.2008T08:37:28
30.05.2008T05:44:27
flux [mJy]
time [min]

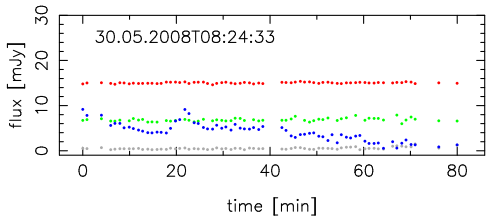
30.05.2008T08:24:33
flux [mJy]
time [min]

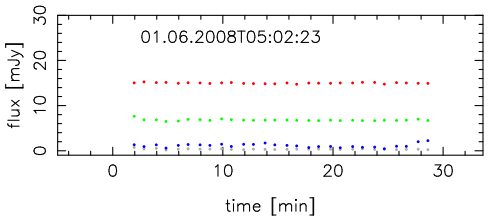
01.06.2008T05:02:23
flux [mJy]
time [min]

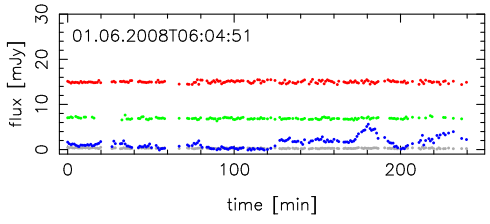
01.06.2008T06:04:51
flux [mJy]
time [min]

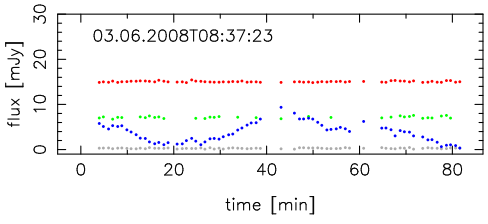
03.06.2008T08:37:23
flux [mJy]
time [min]

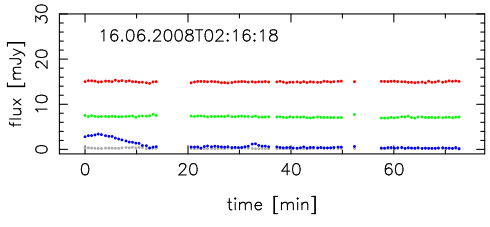
16.06.2008T02:16:18
flux [mJy]
time [min]

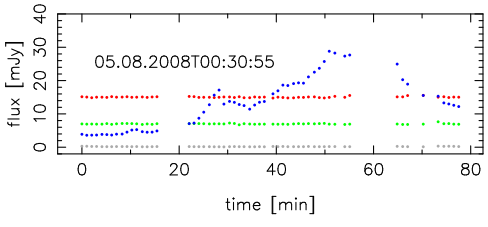
05.08.2008T00:30:55
flux [mJy]
time [min]

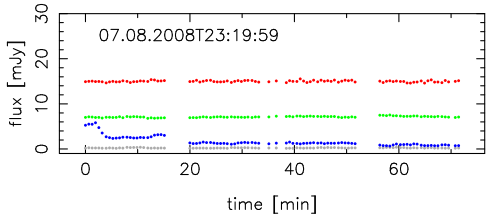
07.08.2008T23:19:59
flux [mJy]
time [min]

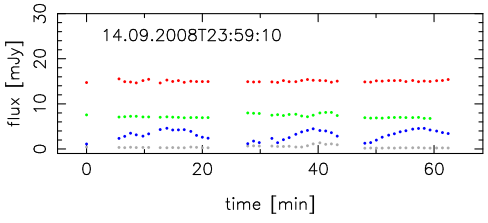
14.09.2008T23:59:10
flux [mJy]
time [min]

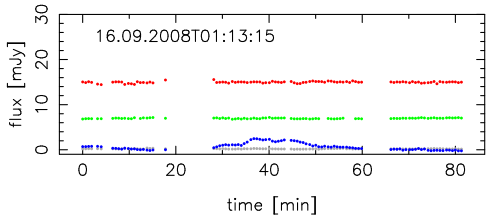
16.09.2008T01:13:15
flux [mJy]
time [min]

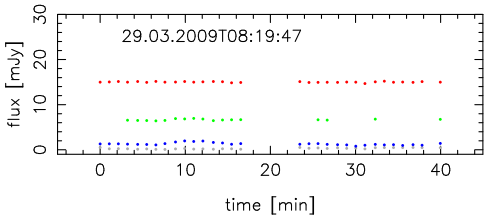
29.03.2009T08:19:47
flux [mJy]
time [min]

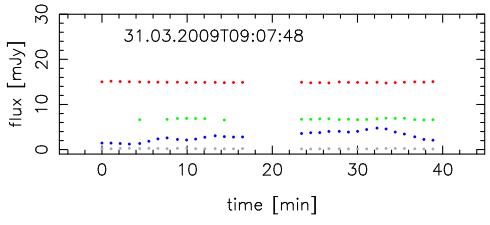
31.03.2009T09:07:48
flux [mJy]
time [min]

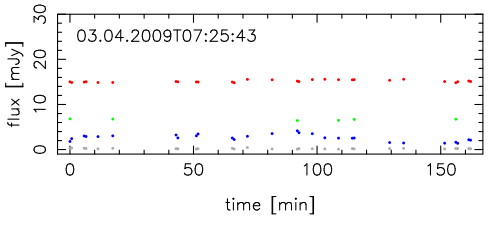
03.04.2009T07:25:43
flux [mJy]
time [min]

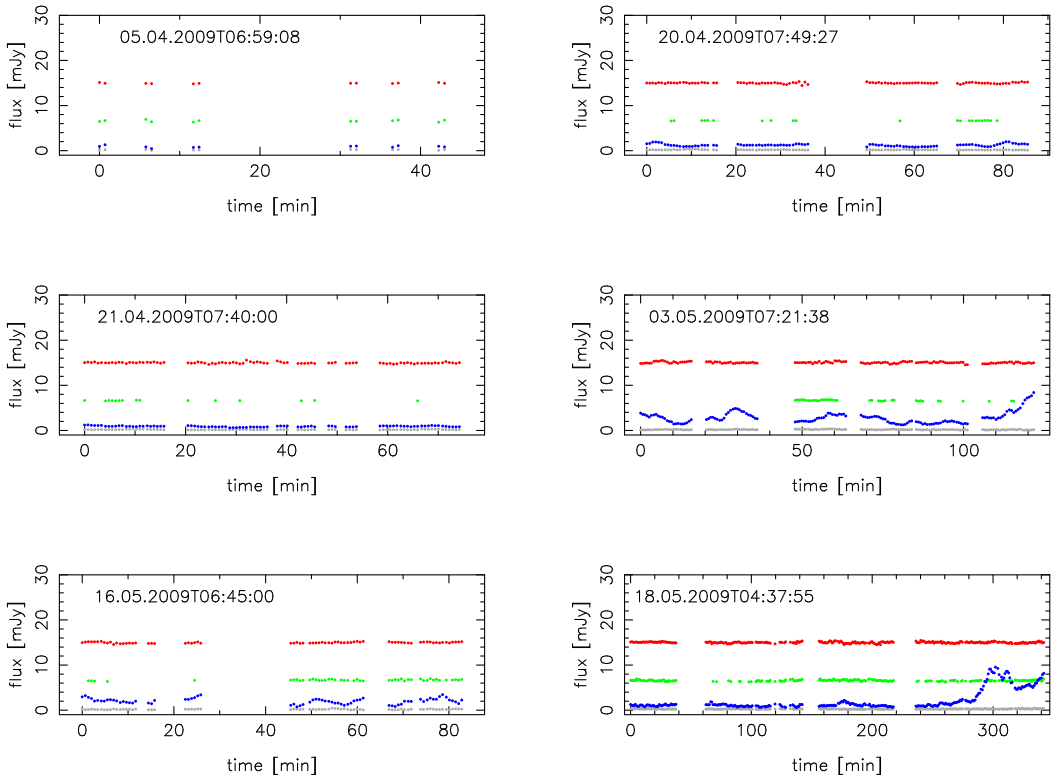
05.04.2009T06:59:08
20.04.2009T07:49:27
21.04.2009T07:40:00
03.05.2009T07:21:38
16.05.2009T06:45:00
18.05.2009T04:37:55
flux [mJy]
time [min]

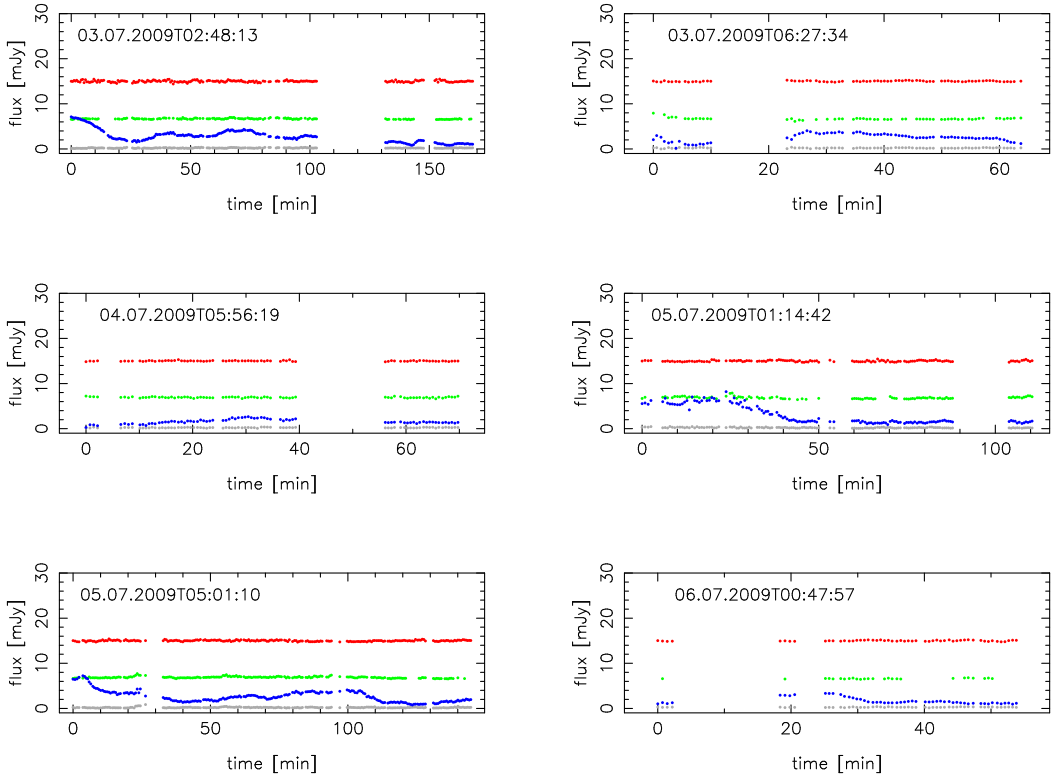
03.07.2009T02:48:13
03.07.2009T06:27:34
04.07.2009T05:56:19
05.07.2009T01:14:42
05.07.2009T05:01:10
06.07.2009T00:47:57
flux [mJy]
time [min]

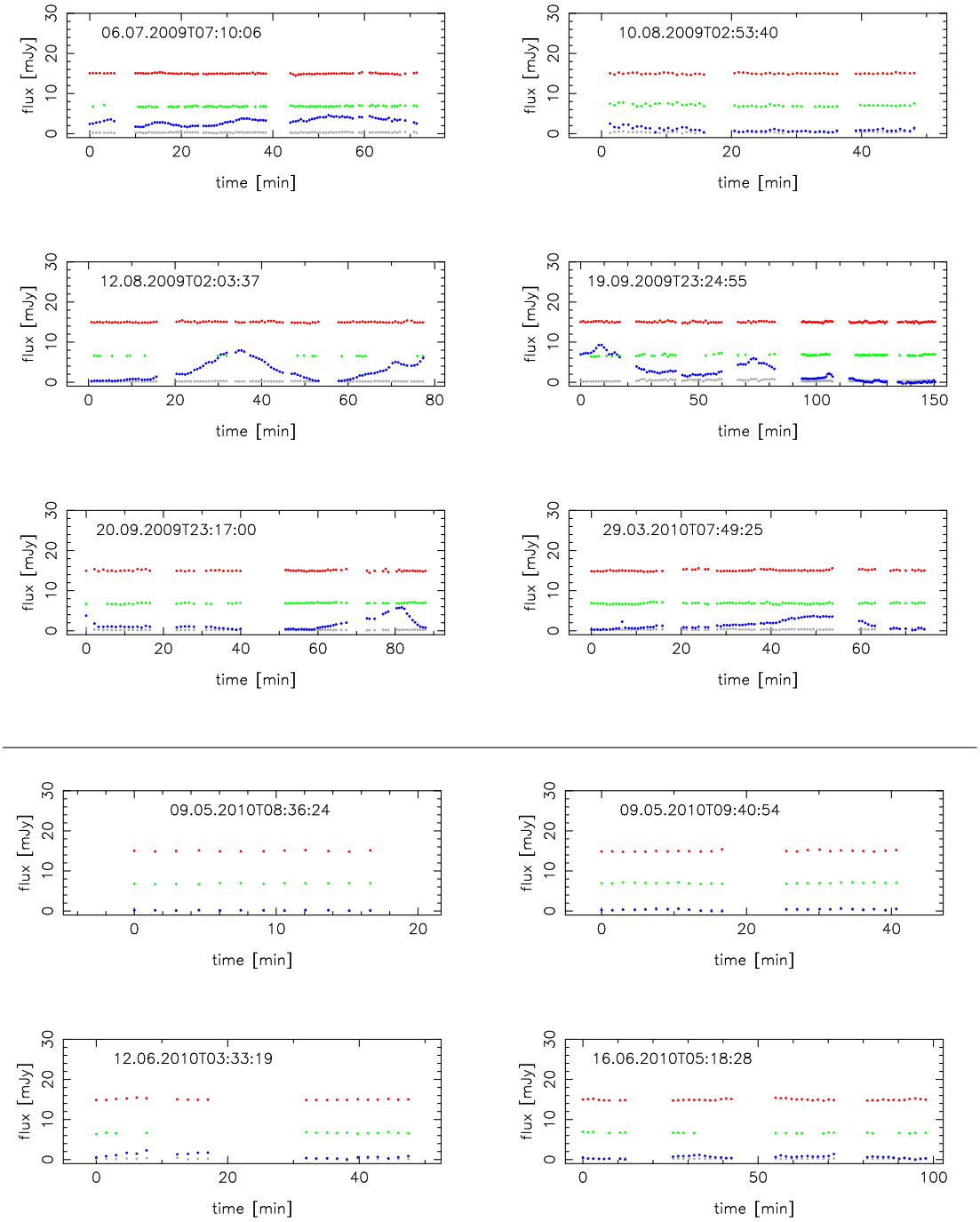

Fig. B.1.: Light curves of Sgr A* (blue), S7 (green), average calibrator flux density (red), and background.

Observations of Sgr A* in Ks-band.

start (UT)	stop (UT)	length [min]	# frames	max. flux density [mJy]	average sampl. [min]	integr. time [sec]	mode	camera	project ID
13.06.2003 02:34:14.23	13.06.2003 07:10:52.51	277	253	3.84	1.097	15/20	I/P	S13	713-0078(A)
14.06.2003 07:27:48.75	14.06.2003 08:51:47.09	84	120	3.07	0.705	20	I	S13	713-0078(A)
15.06.2003 03:00:46.50	15.06.2003 05:30:23.90	150	181	11.38	0.831	20	I	S13	713-0078(A)
16.06.2003 04:47:25.19	16.06.2003 07:42:52.46	175	208	9.80	0.847	20	I	S13	713-0078(A)
19.06.2003 23:51:15.31	20.06.2003 03:53:58.14	243	219	5.60	1.113	20	I	S13	271.B-5019(A)
11.06.2004 06:03:13.30	11.06.2004 09:45:46.88	223	154	2.50	1.454	20	P	S13	073.B-0084(A)
12.06.2004 09:51:43.42	12.06.2004 10:15:20.04	24	22	1.89	1.124	20	P	S13	073.B-0084(A)
13.06.2004 07:54:22.95	13.06.2004 09:15:08.79	81	70	3.84	1.170	20	P	S13	073.B-0084(A)
06.07.2004 03:48:52.53	06.07.2004 07:05:59.31	197	217	2.11	0.912	30	I	S27	073.B-0775(A)
06.07.2004 23:19:38.98	07.07.2004 04:27:41.56	308	344	7.92	0.898	30	I	S13	073.B-0775(A)
08.07.2004 02:37:56.76	08.07.2004 06:53:45.70	256	285	4.33	0.900	30	I	S13	073.B-0775(A)
29.07.2004 00:32:27.25	29.07.2004 01:20:29.53	48	60	3.68	0.814	30	I	S13	273.B.5023(C)
29.07.2004 05:06:00.25	29.07.2004 05:40:33.66	35	43	3.16	0.822	30	I	S13	273.B.5023(C)
30.08.2004 23:50:22.82	31.08.2004 01:28:19.90	98	100	2.93	0.989	30	I	S13	073.B-0775(A)
31.08.2004 23:54:25.97	01.09.2004 04:44:21.31	290	150	3.13	1.945	30	I(P)	S13	073.B-0085(C)
01.09.2004 23:41:03.92	02.09.2004 00:24:17.26	43	32	8.32	1.394	30	P	S13	073.B-0775(B)
02.09.2004 02:00:56.18	02.09.2004 04:15:06.65	134	102	2.15	1.328	30	I/P	S13	073.B-0775(B)
23.09.2004 23:19:09.64	24.09.2004 01:45:11.86	146	115	1.00	1.281	30	I	S13	073.B-0085(C)
09.04.2005 09:29:47.38	09.04.2005 10:16:38.57	47	53	1.14	0.901	30	I	S13	073.B-0085(I)
13.05.2005 08:01:25.07	13.05.2005 10:04:44.69	123	108	3.09	1.152	30	I	S27	073.B-0085(E)
14.05.2005 07:08:54.21	14.05.2005 10:26:43.81	198	176	5.97	1.130	30	I	S13	073.B-0085(D)
16.05.2005 04:56:32.18	16.05.2005 08:24:54.94	208	191	3.36	1.096	30	I	S13	073.B-0085(D)
17.05.2005 04:52:33.23	17.05.2005 07:44:17.20	172	34	3.19	5.204	200	I	S13	073.B-0085(D)
17.05.2005 08:25:05.68	17.05.2005 10:48:01.76	143	30	4.31	4.928	200	I	S13	073.B-0085(D)
20.06.2005 04:52:02.95	20.06.2005 06:34:37.16	103	100	1.94	1.036	30	I	S27	073.B-0085(F)
25.07.2005 01:48:47.44	25.07.2005 07:32:33.24	344	330	8.98	1.044	30	I	S13	271.B-5019(A)
27.07.2005 23:50:43.95	28.07.2005 04:41:49.31	291	158	2.41	1.854	60	I	S13	075.B-0093(C)
29.07.2005 23:03:57.80	30.07.2005 01:35:41.92	152	101	3.55	1.517	30/60	I/P	S13	075.B-0093(C)
30.07.2005 02:07:36.13	30.07.2005 06:21:40.41	254	187	8.94	1.365	30	P	S13	075.B-0093(C)
30.07.2005 23:05:28.75	31.07.2005 06:53:58.74	469	266	6.01	1.767	60	I	S13	075.B-0093(C)

to be continued on next page

continued from previous page

start	stop	length [min]	# frames	max. flux density [mJy]	average sampl. [min]	integr. time [sec]	mode	camera	project ID
02.08.2005 04:25:40.21	02.08.2005 07:01:26.26	156	80	3.49	1.971	60	I	S13	075.B-0093(C)
28.05.2006 08:36:24.43	28.05.2006 09:32:40.35	56	46	5.32	1.250	30	I	S27	077.B-0552(A)
01.06.2006 04:26:03.16	01.06.2006 10:44:27.63	378	244	14.60	1.557	30	I/P	S13/S27	077.B-0552(A)
05.06.2006 05:24:11.62	05.06.2006 06:12:28.06	48	40	2.12	1.237	30	P	S13	077.B-0552(A)
05.06.2006 06:50:02.57	05.06.2006 10:36:32.66	227	126	2.05	1.812	30	P	S13	077.B-0552(A)
29.06.2006 04:50:36.43	29.06.2006 06:41:55.29	111	96	11.79	1.171	33.4	I	S13	077.B-0014(C)
02.08.2006 01:07:54.32	02.08.2006 02:03:15.71	55	48	2.17	1.177	33.6	I	S13	077.B-0014(D)
23.09.2006 00:09:30.22	23.09.2006 01:04:39.36	55	48	3.56	1.173	33.4	I	S13	077.B-0014(F)
24.09.2006 00:07:02.00	24.09.2006 01:12:07.83	65	53	6.20	1.251	33.4	I	S13	077.B-0014(F)
03.10.2006 00:55:33.17	03.10.2006 01:49:23.80	54	48	1.67	1.145	33.4	I	S13	077.B-0014(F)
20.10.2006 23:41:12.70	21.10.2006 00:24:00.13	43	47	2.64	0.930	33.6	I	S13	078.B-0136(A)
04.03.2007 09:09:05.79	04.03.2007 09:48:57.48	40	48	3.91	0.848	36	I	S13	078.B-0136(B)
17.03.2007 09:10:04.97	17.03.2007 10:27:46.76	78	78	1.45	1.009	33.6/56	I	S27	078.B-0136(B)
20.03.2007 09:09:08.59	20.03.2007 10:25:19.74	76	96	7.10	0.801	34.4	I	S13	078.B-0136(B)
01.04.2007 06:52:27.86	01.04.2007 08:08:27.40	76	96	7.16	0.799	30	I	S27	179.B-0261(A)
01.04.2007 08:51:36.27	01.04.2007 09:18:19.08	27	30	1.55	0.921	30	P	S13	179.B-0261(A)
02.04.2007 05:20:38.21	02.04.2007 07:53:36.91	153	150	6.52	1.026	30	I	S13/S27	179.B-0261(A)
02.04.2007 09:46:30.23	02.04.2007 10:35:40.93	49	72	17.03	0.692	30	I	S27	179.B-0261(A)
03.04.2007 06:53:16.77	03.04.2007 10:25:34.11	212	188	4.98	1.135	30	I/P	S13	179.B-0261(A)
04.04.2007 07:15:08.41	04.04.2007 08:08:55.54	54	46	1.84	1.195	30	P	S13	179.B-0261(A)
04.04.2007 09:38:38.23	04.04.2007 10:28:30.48	50	63	1.41	0.804	30	I	S13	179.B-0261(A)
05.04.2007 05:07:42.08	05.04.2007 07:51:16.52	164	140	2.74	1.176	30	P	S13	179.B-0261(A)
06.04.2007 07:01:01.93	06.04.2007 10:18:49.13	198	175	2.10	1.136	30	I/P	S13/S27	179.B-0261(A)
15.05.2007 05:29:55.42	15.05.2007 08:31:48.45	182	116	14.20	1.581	40	I	S13	079.B-0018(A)
16.05.2007 04:47:22.50	16.05.2007 07:11:11.68	144	90	3.27	1.615	40	P	S13	079.B-0018(A)
16.05.2007 07:53:32.58	16.05.2007 08:10:43.02	17	16	2.69	1.144	40	P	S13	079.B-0018(A)
17.05.2007 04:42:14.84	17.05.2007 09:34:40.15	292	192	8.11	1.531	40	P	S13	079.B-0018(A)
19.05.2007 04:55:00.53	19.05.2007 09:41:46.46	287	244	4.10	1.180	40	P	S13	079.B-0018(A)
09.06.2007 04:40:22.39	09.06.2007 05:28:28.78	48	40	3.75	1.233	56	I	S27	179.B-0261(H)
16.06.2007 03:26:46.45	16.06.2007 04:23:27.76	57	62	1.93	0.929	34.4	I	S13	179.B-0261(H)
18.07.2007 22:59:33.75	19.07.2007 03:52:43.66	293	260	4.52	1.131	30	P	S13	179.B-0261(D)
19.07.2007 22:56:43.85	20.07.2007 01:23:08.82	146	138	4.61	1.068	30	P	S13	179.B-0261(D)
20.07.2007 02:22:36.82	20.07.2007 04:55:26.07	153	140	2.44	1.099	30	P	S13	179.B-0261(D)
20.07.2007 22:54:16.15	21.07.2007 01:39:04.00	165	140	7.75	1.185	24/30	P	S13	179.B-0261(D)
21.07.2007 03:03:34.27	21.07.2007 04:45:44.95	102	102	2.50	1.011	30	P	S13	179.B-0261(D)

to be continued on next page

continued from previous page

start	stop	length [min]	# frames	max. flux density [mJy]	average sampl. [min]	integr. time [sec]	mode	camera	project ID
23.07.2007 22:54:07.39	24.07.2007 03:27:34.93	273	248	1.90	1.107	30	P	S13	179.B-0261(D)
24.07.2007 05:23:07.91	24.07.2007 06:27:33.88	64	60	5.12	1.092	30	P	S13	179.B-0261(D)
23.02.2008 08:21:32.28	23.02.2008 09:47:38.65	86	72	1.19	1.212	34.4	I	S13	179.B-0261(L)
13.03.2008 08:18:23.01	13.03.2008 09:29:52.25	71	96	2.89	0.752	34.4	I	S13	179.B-0261(L)
08.04.2008 07:40:14.17	08.04.2008 08:52:12.72	72	96	1.79	0.757	34	I	S13	179.B-0261(M)
06.05.2008 04:45:34.40	06.05.2008 06:47:08.09	122	80	1.64	1.538	45	P	S13	179.B-0261(P)
10.05.2008 05:09:05.13	10.05.2008 10:40:50.62	332	224	2.71	1.487	45	P	S13	179.B-0261(P)
11.05.2008 04:49:25.76	11.05.2008 10:35:01.18	346	232	3.39	1.496	45	P	S13	179.B-0261(P)
25.05.2008 04:55:46.22	25.05.2008 05:24:22.93	29	30	1.54	0.986	40	P	S13	081.B-0648(A)
25.05.2008 06:05:20.32	25.05.2008 10:35:38.65	270	250	8.51	1.085	40	P	S13	081.B-0648(A)
26.05.2008 04:53:25.66	26.05.2008 05:21:58.26	29	30	0.00	0.984	40	P	S13	081.B-0648(A)
27.05.2008 04:52:04.92	27.05.2008 08:29:38.07	218	184	2.74	1.188	40	P	S13	081.B-0648(A)
28.05.2008 08:37:28.23	28.05.2008 09:39:43.95	62	58	4.26	1.092	40	I	S27	081.B-0648(A)
30.05.2008 05:44:27.73	30.05.2008 06:13:11.96	29	30	2.12	0.990	40	P	S13	081.B-0648(A)
30.05.2008 08:24:33.51	30.05.2008 09:45:25.69	81	80	9.18	1.023	40	P	S13	081.B-0648(A)
01.06.2008 05:02:23.63	01.06.2008 05:31:01.00	29	30	2.24	0.986	40	P	S13	081.B-0648(A)
01.06.2008 06:04:51.56	01.06.2008 10:10:26.78	246	240	5.62	1.027	40	P	S13	081.B-0648(A)
03.06.2008 08:37:23.56	03.06.2008 09:58:58.85	82	80	9.36	1.032	40	P	S13	081.B-0648(A)
16.06.2008 02:16:18.38	16.06.2008 03:28:57.79	73	96	3.39	0.764	34.4	I	S13	179.B-0261(T)
05.08.2008 00:30:55.22	05.08.2008 01:48:26.93	78	64	28.82	1.230	56/57	I	S27	179.B-0261(N)
07.08.2008 23:19:59.48	08.08.2008 00:31:25.59	71	96	5.81	0.751	34.4	I	S13	179.B-0261(N)
14.09.2008 23:59:10.24	15.09.2008 01:02:36.99	63	49	4.59	1.321	56	I	S27	179.B-0261(U)
16.09.2008 01:13:15.06	16.09.2008 02:34:32.07	81	103	2.47	0.796	57/34	I	S13	179.B-0261(U)
29.03.2009 08:19:47.54	29.03.2009 08:59:45.50	40	32	1.96	1.289	60	I	S27	179.B-0261(X)
31.03.2009 09:07:48.95	31.03.2009 09:47:44.71	40	32	4.77	1.288	60	I	S27	179.B-0261(X)
03.04.2009 07:25:43.81	03.04.2009 10:07:48.85	162	42	4.16	3.953	30	I	S27	082.B-0952(A)
05.04.2009 06:59:08.13	05.04.2009 07:42:07.38	43	12	1.33	3.907	30	I	S27	082.B-0952(A)
20.04.2009 07:49:27.08	20.04.2009 09:14:51.76	85	96	1.99	0.899	36	I	S13	178.B-0261(W)
21.04.2009 07:40:00.63	21.04.2009 08:54:11.99	74	96	1.25	0.780	36	I	S13	178.B-0261(W)
03.05.2009 07:21:38.94	03.05.2009 09:23:23.02	122	144	8.41	0.851	36	I	S13	183.B-0100(G)
16.05.2009 06:45:00.27	16.05.2009 08:07:48.12	83	78	3.46	1.075	36	I	S13	183.B-0100(G)
18.05.2009 04:37:55.08	18.05.2009 10:19:54.10	342	286	9.54	1.199	40	P	S13	083.B-0331(A)
03.07.2009 02:48:13.57	03.07.2009 05:36:24.08	168	216	7.13	0.782	30/36	I	S13	183.B-0100(D)
03.07.2009 06:27:34.75	03.07.2009 07:31:17.42	64	80	4.04	0.806	30	I	S13	183.B-0100(D)
04.07.2009 05:56:19.24	04.07.2009 07:06:02.72	70	80	2.66	0.882	30	I	S13	183.B-0100(D)

to be continued on next page

continued from previous page

start	stop	length [min]	# frames	max. flux density [mJy]	average sampl. [min]	integr. time [sec]	mode	camera	project ID
05.07.2009 01:14:42.14	05.07.2009 03:05:06.21	110	139	8.20	0.800	30	I	S13	183.B-0100(D)
05.07.2009 05:01:10.12	05.07.2009 07:25:56.07	145	224	7.22	0.649	30	I	S13	183.B-0100(D)
06.07.2009 00:47:57.05	06.07.2009 01:41:45.51	54	56	3.35	0.978	30	I	S13	183.B-0100(D)
06.07.2009 07:10:06.50	06.07.2009 08:22:39.60	73	104	4.59	0.704	30	I	S13	183.B-0100(D)
10.08.2009 02:53:40.41	10.08.2009 03:41:47.05	48	62	2.51	0.788	36	I	S13	183.B-0100(I)
12.08.2009 02:03:37.66	12.08.2009 03:20:56.96	77	101	7.92	0.773	36	I	S13	183.B-0100(I)
19.09.2009 23:24:55.71	20.09.2009 01:55:16.81	150	132	9.30	1.147	60	I	S13/S27	183.B-0100(J)
20.09.2009 23:17:00.08	21.09.2009 00:44:50.73	88	80	5.83	1.111	60	I	S13/S27	183.B-0100(J)
29.03.2010 07:49:25.57	29.03.2010 09:03:33.59	74	96	3.70	0.780	36	I	S13	183.B-0100(L)
09.05.2010 08:36:24.16	09.05.2010 08:53:01.83	17	12	0.23	1.511	63	I	S13	183.B-0100(T)
09.05.2010 09:40:54.93	09.05.2010 10:23:02.79	42	24	0.68	1.831	84	I	S13	183.B-0100(T)
12.06.2010 03:33:19.65	12.06.2010 04:20:46.86	47	24	2.30	2.063	86	I	S13	183.B-0100(T)
16.06.2010 05:18:28.69	16.06.2010 06:56:15.44	98	48	1.38	2.080	84	I	S13	183.B-0100(U)

Table B.1.: This table shows basic information for each dataset shown in the Figures before: start-stop times, length of the data set, number of frames, maximum flux density occurring in the set, average time sampling over the set, the used integration time, the observational mode (imaging or polarimetric), the camera (S13 with 13” FOV or S27 with 27”), and the project ID of the observations. Note that start-stop times, frame numbers and length average are given for the datasets before applying the quality cut, average sampling and maximum flux density after the cut.

C. Flux density statistics

In this Appendix I present supplement information for the statistical analysis described in section 2.2.1. I present histograms of the Ks-Band flux densities of Sgr A* with different than the optimal binning, showing that the linear behavior of the histogram is not binning dependent, and the CDFs of independently drawn power-law distributed surrogate data in comparison to the observed CDF (see section 2.2.2).

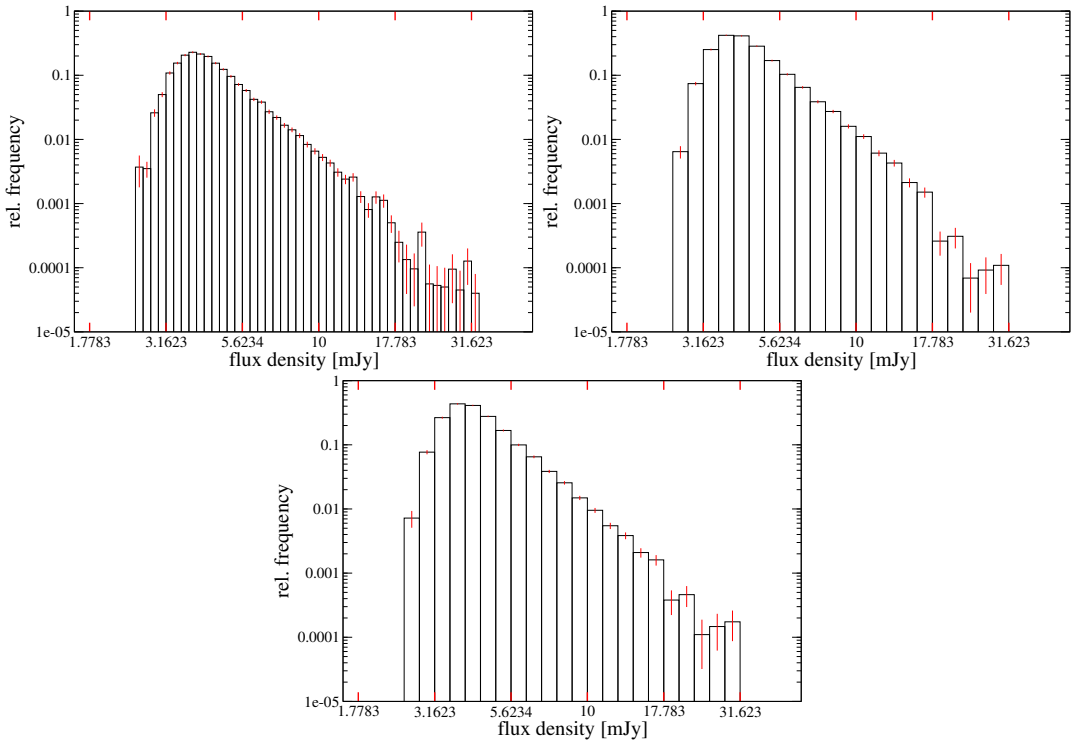

Fig. C.1.: The observed flux densities in histograms with bin numbers higher (upper left, 45 bins) and lower (upper right, 22, compare Dodds-Eden et al. 2011) than optimal (32). The latter I also show in a integration time weighted version (as conducted by Dodds-Eden et al. 2011), finding now significant difference (lower plot).

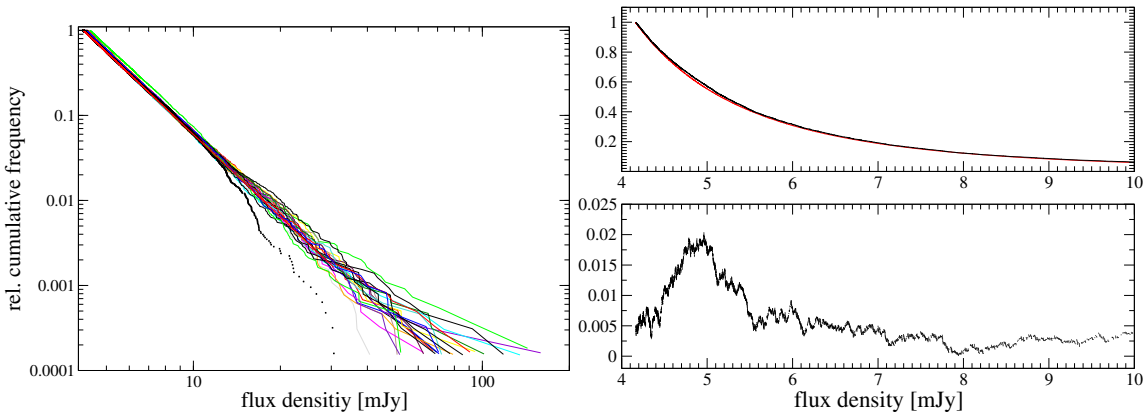

Fig. C.2.: Comparison of the observed CDF with surrogate data drawn independently from a power-law according to Eq. (2.20) (section 2.2.2). Although the most obvious differences seem to be at highest flux densities, this impression is caused by the logarithmic presentation (left). The KS statistics used for determining the best x_{min} and the plausibility of a power-law model in section 2.2.2 is dominated by differences at lower flux densities as demonstrated in the plots on the right, showing the comparison of the observed CDF and a surrogate CDF with a worse Kolmogorov-value than the observed data (upper right: CDFs in linear plotting, lower right: difference of the CDFs).

D. Correction matrices for the optical components of NACO

In this appendix I give an analytic solution for the correction matrix C_{NACO} in a way that makes it easy to program it. This solution was obtained by the inverse of the matrices in Eq. (3.13), which I also give here. The inverse of the rotation matrix in Stokes space (see Eq. (3.10)) can be obtained by changing the sign of the parameter p. The inverse of the Mueller matrix for metallic reflection (3.8) is given by

$$R^{-1} = \begin{pmatrix} r_+ & r_- & 0 & 0 \\ r_- & r_+ & 0 & 0 \\ 0 & 0 & \Delta_c & \Delta_s \\ 0 & 0 & -\Delta_s & \Delta_C \end{pmatrix} , \tag{D.1}$$

with variables analog to D.7. With the inverted Mueller matrices we are able to give an analytic correction matrix that transforms the measured Stokes vector into the Stokes vector on the sky (with the orientation east of north)

$$S = C_{\mathrm{NACO}} \times S' = M_{\mathrm{var}}^{-1} \times M_{\mathrm{con}}^{-1} \times S' , \tag{D.2}$$

with M_{var} the position depending and M_{con} the constant part of the Mueller matrix for NACO

$$M_{\mathrm{var}}^{-1} = \begin{pmatrix} r_+^{\mathrm{alu}} & -ac_p - bs_p & as_p - bc_p & 0 \\ r_-^{\mathrm{alu}} c_p & ec_p^2 + fs_p c_p + t & fc_p^2 - es_p c_p + u & -\Delta_s^{\mathrm{alu}} s_p \\ r_-^{\mathrm{alu}} s_p & es_p c_p - fc_p^2 + v & ec_p^2 + fs_p c_p - w & \Delta_s^{\mathrm{alu}} c_p \\ 0 & dc_p - gs_p & -ds_p - gc_p & \Delta_c^{\mathrm{alu}} \end{pmatrix} , \tag{D.3}$$

with

$$\begin{aligned} s_p &= \sin(2p) \\ c_p &= \cos(2p) \\ s_\beta &= \sin(2\beta) \\ c_\beta &= \cos(2\beta) \\ a &= -r_-^{\mathrm{alu}} \cos(2\alpha) \\ b &= r_-^{\mathrm{alu}} \sin(2\alpha) \\ d &= -\Delta_s^{\mathrm{alu}} \sin(2\alpha) \\ g &= \Delta_s^{\mathrm{alu}} \cos(2\alpha) \end{aligned} \qquad \begin{aligned} v &= -r_+^{\mathrm{alu}} \sin(2\alpha) \\ w &= r_+^{\mathrm{alu}} \cos(2\alpha) \\ t &= -\Delta_c^{\mathrm{alu}} \cos(2\alpha) \\ u &= \Delta_c^{\mathrm{alu}} \sin(2\alpha) \\ e &= \left(r_+^{\mathrm{alu}} + \Delta_c^{\mathrm{alu}}\right) \cos(2\alpha) \\ f &= -\left(r_+^{\mathrm{alu}} + \Delta_c^{\mathrm{alu}}\right) \sin(2\alpha) \end{aligned} \tag{D.4}$$

and

$$M_{\mathrm{con}}^{-1} = \begin{pmatrix} T_+k - T_-l\left(c_\beta + s_\beta\right) & T_-k - T_+lc_\beta & -T_+ls_\beta & 0 \\ -T_+l + T_-k\left(c_\beta + s_\beta\right) & -T_-l + T_+kc_\beta & T_+ks_\beta & 0 \\ T_-\left[m\left(c_\beta - s_\beta\right) - n\right] & -T_+ms_\beta & T_+mc_\beta & -T_+n \\ T_-\left[n\left(c_\beta - s_\beta\right) + m\right] & -T_+ns_\beta & T_+nc_\beta & T_+m \end{pmatrix} \tag{D.5}$$

with

$$\begin{aligned} k &= \left(r_+^{\mathrm{sil}}\right)^2 + \left(r_-^{\mathrm{sil}}\right)^2 \\ l &= 2r_+^{\mathrm{sil}}r_-^{\mathrm{sil}} \qquad\qquad n = 2\Delta_c^{\mathrm{sil}}\Delta_s^{\mathrm{sil}} \\ m &= \left(\Delta_c^{\mathrm{sil}}\right)^2 - \left(\Delta_s^{\mathrm{sil}}\right)^2 \qquad T_\pm = r_2 \pm r_1 \end{aligned} \tag{D.6}$$

and with

$$\begin{aligned} r_\pm^{\mathrm{alu}} &= \frac{1}{2}\frac{r_\parallel^{\mathrm{alu}} \pm r_\perp^{\mathrm{alu}}}{r_\parallel^{\mathrm{alu}} r_\perp^{\mathrm{alu}}} \qquad r_\pm^{\mathrm{sil}} = \frac{1}{2}\frac{r_\parallel^{\mathrm{sil}} \pm r_\perp^{\mathrm{sil}}}{r_\parallel^{\mathrm{sil}} r_\perp^{\mathrm{sil}}} \\ \Delta_c^{\mathrm{alu}} &= \frac{\cos(\delta^{\mathrm{alu}})}{\sqrt{r_\parallel^{\mathrm{alu}} r_\perp^{\mathrm{alu}}}} \qquad \Delta_c^{\mathrm{sil}} = \frac{\cos(\delta^{\mathrm{sil}})}{\sqrt{r_\parallel^{\mathrm{sil}} r_\perp^{\mathrm{sil}}}} \\ \Delta_s^{\mathrm{alu}} &= \frac{\sin(\delta^{\mathrm{alu}})}{\sqrt{r_\parallel^{\mathrm{alu}} r_\perp^{\mathrm{alu}}}} \qquad \Delta_s^{\mathrm{sil}} = \frac{\sin(\delta^{\mathrm{sil}})}{\sqrt{r_\parallel^{\mathrm{sil}} r_\perp^{\mathrm{sil}}}} \end{aligned}$$

$$\begin{aligned} r_1 &= \frac{1}{2}\left(r_\parallel^{\mathrm{gold,I}} r_\parallel^{\mathrm{gold,II}} + r_\perp^{\mathrm{gold,I}} r_\perp^{\mathrm{gold,II}}\right) \\ r_2 &= r_\perp^{\mathrm{gold,I}} r_\perp^{\mathrm{gold,II}} \,. \end{aligned} \tag{D.7}$$

The parameters are

$$
\begin{aligned}
p &= \text{parallactic angle} \\
\alpha &= \text{rotator angle} \\
\beta &= 13.2^\circ \\
r_{\parallel}^{\text{alu}} &= 0.962622 \\
r_{\perp}^{\text{alu}} &= 0.981133 \\
\delta^{\text{alu}} &= 176.028^\circ \\
r_{\parallel}^{\text{sil}} &= 0.98272 \\
r_{\perp}^{\text{sil}} &= 0.98872 \\
\delta^{\text{sil}} &= 165^\circ \\
r_{\parallel}^{\text{gold,I}} &= 0.972664/0.977011 \ \ (\text{S13}/27) \\
r_{\perp}^{\text{gold,I}} &= 0.98484/0.981932 \ \ (\text{S13}/27) \\
r_{\parallel}^{\text{gold,II}} &= 0.979588/0.97865 \ \ (\text{S13}/27) \\
r_{\perp}^{\text{gold,II}} &= 0.979642/0.980538 \ \ (\text{S13}/27)\,. \qquad \text{(D.8)}
\end{aligned}
$$

These matrices are not normalized, because it would make them more difficult to read. This just effects total intensity, the normalized Stokes parameters remain unaffected. To switch off matrix Tr^{-1} after a flat-field correction as described in 3.6 set $r_1 = r_2$.

E. Supplement information for the polarimetric calibration of NACO

In Fig. E.1 I show the confirmation of my model through Stokes-fits for IRS16NW, IRS16CC, and S67. In Fig. E.3 I show two more Sgr A* light curves analyzed with the more exact and elaborate method presented here and the 'boot strapping' method used before. The data used for this thesis are summarized in Table E.

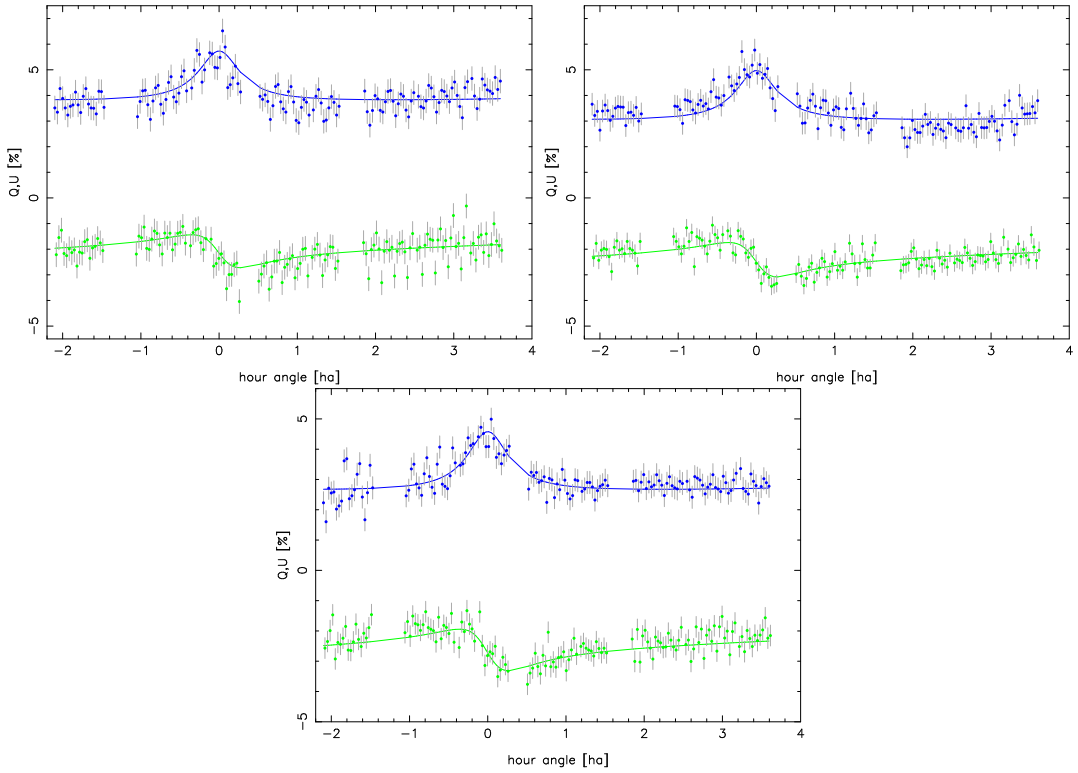

Fig. E.1.: Stokes-fits (Q blue, U green) for IRS16NW (upper panel), IRS16CC (middle), and S67 (lower panel). See Fig. 3.11 and Table 3.8.2.

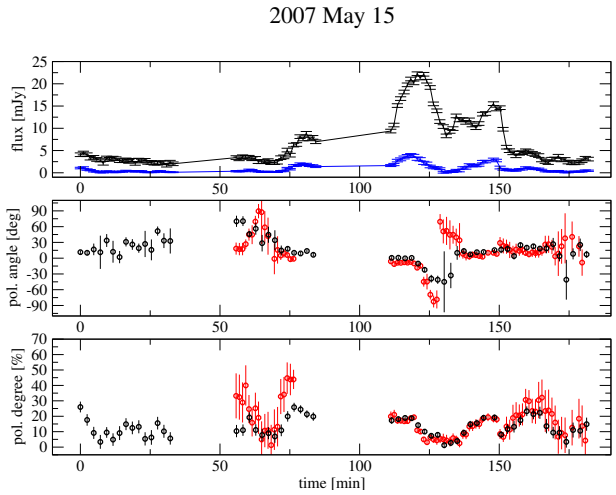

Fig. E.2.: Polarimetric light curve from 2007 May 15. Plots analog to Fig. 3.13. The meridian transit occurred at 86.5 min.

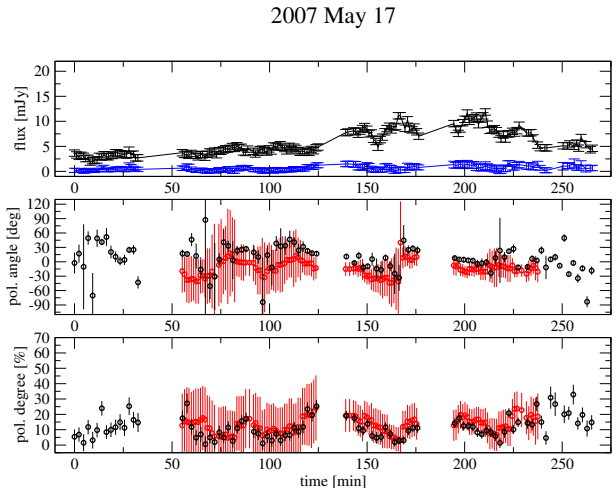

Fig. E.3.: Polarimetric light curve from 2007 May 17. Plots analog to Fig. 3.13. The meridian transit occurred at 126.4 min.

Source	Date	# Frames	Time Interval (UT)	Project ID	PI	Setup
GC & Sgr A*	2006 June 1	156	06:38:39 - 10:44:27	077.B-0552(A)	Eckart	Woll. & HWP (0°/45°), S13
	2007 May 15	116	05:29:55 - 08:31:48	079.B-0084(A)	Eckart	Woll. & HWP (0°/45°), S13
	2007 May 17	192	04:42:14 - 09:34:40	079.B-0084(A)	Eckart	Woll. & HWP (0°/45°, S13)
GC & IRS16	2009 May 18	286	04:37:55 - 10:19:54	083.B-0031(A)	Eckart	Woll. & HWP (0°/45°), S13
IRS21	2005 July 30	18	06:44:50 - 07:01:32	075.B-0093(B)	Eckart	Woll. & HWP (0°/30°/60°), S13
RCra88	2004 June 11	10	10:15:49 - 10:25:49	073.B-0084(A)	Genzel	Woll. & HWP (0°/45°), S13
WD1344	2007 April 08 / 09	10		079.D-0441(B)	Israel	Woll. & rotator (0°/45°), S27
WD2039-202	2007 August 18 / September 21	15		079.D-0444(A)	Israel	Woll. & rotator (0°/45°), S27
HD109055	2009 March 10 / 14	38		082.D-0137(B)	Israel	Woll. & rotator (0°/45°), S27

Table E.1.: Polarimatric observations in the Ks-band, used for the polarimetric calibration of NACO. The column “setup” shows the facilities used and at which angles the data were obtained.

Abbreviations

ADU	Analog-to-Digital Unit
AO	Adaptive Optics
BH	Black Hole
BHXRB	Black Hole X-Ray Binary system
CDF	Cumulative Distribution Function
DFT	Discrete Fourier Transform
DIT	Detector Integration Time
DM	Deformable Mirror
ESO	European Southern Observatory
FITS	Flexible Image Transport System
FWHM	Full Width Half Maximum
GC	Galactic Center
HWP	Half Wave Plate
IDL	Interactive Data Language
IP	Instrumental Polarization
IRS	InfraRed Source
ISCO	Innermost Stable Circular Orbit
KS	Kolmogorov-Smirnov Statistics
LR	Lucy-Richardson Deconvolution
M 1/2/3	Mirror 1/2/3
MC	Monte Carlo Simulation
NACO	Nasmyth Adaptive Optics System/Coude Near Infrared Camera
NDIT	number of subintegrations
NIR	Near-InfraRed
PI	Principle Investigator
PSD	Power Spectral Density
PSF	Point Spread Function
QPO	Qasi Periodic Oscillation
RLP	Relative Logarithmic Posterior probability
RMS	Root Mean Square
SED	Spectral Energie Distribution
SgrA*	Sagittarius A Star
SMA	Submillimeter Array
SMBH	Super Massive Blach Hole
SSC	Synchrotron Self-Compton

TNG	Telescopio Nazionale Galileo
TTM	Tip and Tilt Mirror
UT	Universal Time
VLBI	Very Long Baseline Interferometry
VLT	Very Large Telescope
UT4	Unit Telescope 4

Bibliography

Abramowicz, M. A., Bao, G., Lanza, A., & Zhang, X. 1991, *X-ray variability power spectra of active galactic nuclei*, A&A, 245, 454

Ageorges, N., Lidman, C., Kaufer, A., & Hainaut, O. 2007, *NAOS-CONICA User Manual*, manual, ESO

Backer, D. C. & Sramek, R. A. 1999, *Proper Motion of the Compact, Nonthermal Radio Source in the Galactic Center, Sagittarius A**, ApJ, 524, 805

Baganoff, F. K., Bautz, M. W., Brandt, W. N., Chartas, G., Feigelson, E. D., Garmire, G. P., Maeda, Y., Morris, M., Ricker, G. R., Townsley, L. K., & Walter, F. 2001, *Rapid X-ray flaring from the direction of the supermassive black hole at the Galactic Centre*, Nature, 413, 45

Baganoff, F. K., Maeda, Y., Morris, M., Bautz, M. W., Brandt, W. N., Cui, W., Doty, J. P., Feigelson, E. D., Garmire, G. P., Pravdo, S. H., Ricker, G. R., & Townsley, L. K. 2003, *Chandra X-Ray Spectroscopic Imaging of Sagittarius A* and the Central Parsec of the Galaxy*, ApJ, 591, 891

Balick, B. & Brown, R. L. 1974, *Intense sub-arcsecond structure in the galactic center*, ApJ, 194, 265

Bertram, T. 2007, *Cophasing LINC-NIRVANA and Molecular gas in low-luminosity QSO host and cluster galaxies*, PhD thesis, Universität Köln

Bremer, M., Witzel, G., Eckart, A., Zamaninasab, M., Buchholz, R. M., Schödel, R., Straubmeier, C., García-Marín, M., & Duschl, W. 2011, *The near-infrared spectral index of Sagittarius A* derived from Ks- and H-band flare statistics*, A&A, 532, A26

Cenko, S. B., Krimm, H. A., Horesh, A., Rau, A., Frail, D. A., Kennea, J. A., Levan, A. J., Holland, S. T., Butler, N. R., Quimby, R. M., Bloom, J. S., Filippenko, A. V., Gal-Yam, A., Greiner, J., Kulkarni, S. R., Ofek, E. O., Olivares E., F., Schady, P., Silverman, J. M., Tanvir, N., & Xu, D. 2011, *Swift J2058.4+0516: Discovery of a Possible Second Relativistic Tidal Disruption Flare*, ArXiv e-prints, arXiv:1107.5307

Clarke, D. 1973, *Effects of Polarization on the Transmission of Coude-Spectrometer Systems*, A&A, 24, 165

Clauset, A., Rohilla Shalizi, C., & Newman, M. E. J. 2007, *Power-law distributions in empirical data*, ArXiv e-prints, arXiv:0706.1062

Cunningham, J. M. & Bardeen, C. T. 1973, *The Optical Appearance of a Star Orbiting an Extreme Kerr Black Hole*, ApJ, 183, 237

Devillard, N. 1999, *Infrared Jitter Imaging Data Reduction: Algorithms and Implementation*, in Astronomical Society of the Pacific Conference Series, Vol. 172, Astronomical Data Analysis Software and Systems VIII, ed. D. M. Mehringer, R. L. Plante, & D. A. Roberts, 333

Diolaiti, E., Bendinelli, O., Bonaccini, D., Close, L. M., Currie, D. G., & Parmeggiani, G. 2000, *StarFinder: an IDL GUI-based code to analyze crowded fields with isoplanatic correcting PSF fitting*, in Presented at the Society of Photo-Optical Instrumentation Engineers (SPIE) Conference, Vol. 4007, Proc. SPIE Vol. 4007, p. 879-888, Adaptive Optical Systems Technology, Peter L. Wizinowich; Ed., ed. P. L. Wizinowich, 879–888

Do, T., Ghez, A. M., Morris, M. R., Yelda, S., Meyer, L., Lu, J. R., Hornstein, S. D., & Matthews, K. 2009, *A Near-Infrared Variability Study of the Galactic Black Hole: A Red Noise Source with NO Detected Periodicity*, ApJ, 691, 1021

Dodds-Eden, K., Gillessen, S., Fritz, T. K., Eisenhauer, F., Trippe, S., Genzel, R., Ott, T., Bartko, H., Pfuhl, O., Bower, G., Goldwurm, A., Porquet, D., Trap, G., & Yusef-Zadeh, F. 2011, *The Two States of Sgr A* in the Near-infrared: Bright Episodic Flares on Top of Low-level Continuous Variability*, ApJ, 728, 37

Dodds-Eden, K., Porquet, D., Trap, G., Quataert, E., Haubois, X., Gillessen, S., Grosso, N., Pantin, E., Falcke, H., Rouan, D., Genzel, R., Hasinger, G., Goldwurm, A., Yusef-Zadeh, F., Clenet, Y., Trippe, S., Lagage, P., Bartko, H., Eisenhauer, F., Ott, T., Paumard, T., Perrin, G., Yuan, F., Fritz, T. K., & Mascetti, L. 2009, *Evidence for X-Ray Synchrotron Emission from Simultaneous Mid-Infrared to X-Ray Observations of a Strong Sgr A* Flare*, ApJ, 698, 676

Doeleman, S. S., Weintroub, J., Rogers, A. E. E., Plambeck, R., Freund, R., Tilanus, R. P. J., Friberg, P., Ziurys, L. M., Moran, J. M., Corey, B., Young, K. H., Smythe, D. L., Titus, M., Marrone, D. P., Cappallo, R. J., Bock, D. C.-J., Bower, G. C., Chamberlin, R., Davis, G. R., Krichbaum, T. P., Lamb, J., Maness, H., Niell, A. E.,

Roy, A., Strittmatter, P., Werthimer, D., Whitney, A. R., & Woody, D. 2008, *Event-horizon-scale structure in the supermassive black hole candidate at the Galactic Centre*, Nature, 455, 78

Dovčiak, M., Karas, V., Matt, G., & Goosmann, R. W. 2008, *Variation in the primary and reprocessed radiation from an orbiting spot around a black hole*, MNRAS, 384, 361

Dovčiak, M., Karas, V., & Yaqoob, T. 2004, *An Extended Scheme for Fitting X-Ray Data with Accretion Disk Spectra in the Strong Gravity Regime*, ApJS, 153, 205

Eckart, A., Baganoff, F. K., Morris, M., Bautz, M. W., Brandt, W. N., Garmire, G. P., Genzel, R., Ott, T., Ricker, G. R., Straubmeier, C., Viehmann, T., Schödel, R., Bower, G. C., & Goldston, J. E. 2004, *First simultaneous NIR/X-ray detection of a flare from Sgr A**, A&A, 427, 1

Eckart, A., Baganoff, F. K., Schödel, R., Morris, M., Genzel, R., Bower, G. C., Marrone, D., Moran, J. M., Viehmann, T., Bautz, M. W., Brandt, W. N., Garmire, G. P., Ott, T., Trippe, S., Ricker, G. R., Straubmeier, C., Roberts, D. A., Yusef-Zadeh, F., Zhao, J. H., & Rao, R. 2006a, *The flare activity of Sagittarius A*. New coordinated mm to X-ray observations*, A&A, 450, 535

Eckart, A., Baganoff, F. K., Zamaninasab, M., Morris, M. R., Schödel, R., Meyer, L., Muzic, K., Bautz, M. W., Brandt, W. N., Garmire, G. P., Ricker, G. R., Kunneriath, D., Straubmeier, C., Duschl, W., Dovciak, M., Karas, V., Markoff, S., Najarro, F., Mauerhan, J., Moultaka, J., & Zensus, A. 2008a, *Polarized NIR and X-ray flares from Sagittarius A**, A&A, 479, 625

Eckart, A., García-Marín, M., Vogel, S. N., Teuben, P., Morris, M. R., Baganoff, F., Dexter, J., Schödel, R., Witzel, G., Valencia-S., M., Karas, V., Kunneriath, D., Straubmeier, C., Moser, L., Sabha, N., Buchholz, R., Zamaninasab, M., Mužić, K., Moultaka, J., & Zensus, J. A. 2012, *Millimeter to X-ray flares from Sagittarius A**, A&A, 537, A52

Eckart, A. & Genzel, R. 1996, *Observations of stellar proper motions near the Galactic Centre*, Nature, 383, 415

—. 1997, *Stellar proper motions in the central 0.1 PC of the Galaxy*, MNRAS, 284, 576

Eckart, A., Genzel, R., Hofmann, R., Sams, B. J., & Tacconi-Garman, L. E. 1995, *High angular resolution spectroscopic and polarimetric imaging of the galactic center in the near-infrared*, ApJ, 445, L23

Eckart, A., Genzel, R., Ott, T., & Schödel, R. 2002, *Stellar orbits near Sagittarius A**, MNRAS, 331, 917

Eckart, A., Schödel, R., Baganoff, F. K., Morris, M., Bertram, T., Dovciak, M., Dowries, D., Duschl, W. J., Karas, V., König, S., Krichbaum, T., Krips, M., Kunneriath, D., Lu, R., Markoff, S., Mauerhan, J., Meyer, L., Moultaka, J., Muzic, K., Najarro, F., Schuster, K., Sjouwerman, L., Straubmeier, C., Thum, C., Vogel, S., Wiesemeyer, H., Witzel, G., Zamaninasab, M., & Zensus, A. 2008b, *Coordinated multi-wavelength observations of Sgr A**, Journal of Physics Conference Series, 131, 012002

Eckart, A., Schödel, R., García-Marín, M., Witzel, G., Weiss, A., Baganoff, F. K., Morris, M. R., Bertram, T., Dovčiak, M., Duschl, W. J., Karas, V., König, S., Krichbaum, T. P., Krips, M., Kunneriath, D., Lu, R., Markoff, S., Mauerhan, J., Meyer, L., Moultaka, J., Mužić, K., Najarro, F., Pott, J., Schuster, K. F., Sjouwerman, L. O., Straubmeier, C., Thum, C., Vogel, S. N., Wiesemeyer, H., Zamaninasab, M., & Zensus, J. A. 2008c, *Simultaneous NIR/sub-mm observation of flare emission from Sagittarius A**, A&A, 492, 337

Eckart, A., Schödel, R., Meyer, L., Müzić, K., Pott, J., Moultaka, J., Straubmeier, C., Dovciak, M., Karas, V., Genzel, R., Ott, T., Trippe, S., Najarro, F., Morris, M., & Baganoff, F. 2006b, *The Galactic Centre: The Flare Activity of SgrA* and High-Resolution Explorations of Dusty Stars*, The Messenger, 125, 2

Eckart, A., Schödel, R., Meyer, L., Trippe, S., Ott, T., & Genzel, R. 2006c, *Polarimetry of near-infrared flares from Sagittarius A**, A&A, 455, 1

Eckart, A., Schödel, R., & Straubmeier, C. 2005, The black hole at the center of the Milky Way, 1st edn. (The black hole at the center of the Milky Way / Andreas Eckart, Rainer Schödel, Christian Straubmeier. London: Imperial College Press ; Hackensack, NJ : Distributed by World Scientific Pub. Co., c2005.)

Eisenhauer, F., Schödel, R., Genzel, R., Ott, T., Tecza, M., Abuter, R., Eckart, A., & Alexander, T. 2003, *A Geometric Determination of the Distance to the Galactic Center*, ApJ, 597, L121

Emmanoulopoulos, D., McHardy, I. M., & Uttley, P. 2010, *On the use of structure functions to study blazar variability: caveats and problems*, MNRAS, 404, 931

Falcke, H. & Markoff, S. 2000, *The jet model for Sgr A*: Radio and X-ray spectrum*, A&A, 362, 113

Freitag, M. 2003, *Captures of stars by a massive black hole: Investigations in numerical stellar dynamics*, in American Institute of Physics Conference Series, Vol. 686, The Astrophysics of Gravitational Wave Sources, ed. J. M. Centrella, 109–114

Fritz, T., Gillessen, S., Trippe, S., Ott, T., Bartko, H., Pfuhl, O., Dodds-Eden, K., Davies, R., Eisenhauer, F., & Genzel, R. 2010, *What is limiting near-infrared astrometry in the Galactic Centre?*, MNRAS, 401, 1177

Genzel, R., Eisenhauer, F., & Gillessen, S. 2010, *The Galactic Center massive black hole and nuclear star cluster*, Reviews of Modern Physics, 82, 3121

Genzel, R., Schödel, R., Ott, T., Eckart, A., Alexander, T., Lacombe, F., Rouan, D., & Aschenbach, B. 2003, *Near-infrared flares from accreting gas around the supermassive black hole at the Galactic Centre*, Nature, 425, 934

Ghez, A. M., Morris, M., Becklin, E. E., Tanner, A., & Kremenek, T. 2000, *The accelerations of stars orbiting the Milky Way's central black hole*, Nature, 407, 349

Ghez, A. M., Salim, S., Hornstein, S. D., Tanner, A., Lu, J. R., Morris, M., Becklin, E. E., & Duchêne, G. 2005, *Stellar Orbits around the Galactic Center Black Hole*, ApJ, 620, 744

Ghez, A. M., Salim, S., Weinberg, N. N., Lu, J. R., Do, T., Dunn, J. K., Matthews, K., Morris, M. R., Yelda, S., Becklin, E. E., Kremenek, T., Milosavljevic, M., & Naiman, J. 2008, *Measuring Distance and Properties of the Milky Way's Central Supermassive Black Hole with Stellar Orbits*, ApJ, 689, 1044

Gillessen, S., Eisenhauer, F., Trippe, S., Alexander, T., Genzel, R., Martins, F., & Ott, T. 2009, *Monitoring Stellar Orbits Around the Massive Black Hole in the Galactic Center*, ApJ, 692, 1075

Gillessen, S., Genzel, R., Fritz, T. K., Quataert, E., Alig, C., Burkert, A., Cuadra, J., Eisenhauer, F., Pfuhl, O., Dodds-Eden, K., Gammie, C. F., & Ott, T. 2012, *A gas cloud on its way towards the supermassive black hole at the Galactic Centre*, Nature, 481, 51

Giro, E., Bonoli, C., Leone, F., Molinari, E., Pernechele, C., & Zacchei, A. 2003, *Polarization properties at the Nasmyth focus of the alt-azimuth TNG telescope*, in Society of Photo-Optical Instrumentation Engineers (SPIE) Conference Series, Vol. 4843, Society of Photo-Optical Instrumentation Engineers (SPIE) Conference Series, ed. S. Fineschi, 456–464

Hodapp, K.-W. 1984, Diploma thesis, Universität Heidelberg

Hollywood, J. M., Melia, F., Close, L. M., McCarthy, Jr., D. W., & Dekeyser, T. A. 1995, *General Relativistic Flux Modulations in the Galactic Center Black Hole Candidate Sagittarius A**, ApJ, 448, L21

Hornstein, S. D., Matthews, K., Ghez, A. M., Lu, J. R., Morris, M., Becklin, E. E., Rafelski, M., & Baganoff, F. K. 2007, *A Constant Spectral Index for Sagittarius A* during Infrared/X-Ray Intensity Variations*, ApJ, 667, 900

Karas, V. & Bao, G. 1992, *On the light curve of an orbiting SPOT*, A&A, 257, 531

Knacke, R. F. & Capps, R. W. 1977, *Infrared polarization of the galactic center. II*, ApJ, 216, 271

Knuth, K. H. 2006, *Optimal Data-Based Binning for Histograms*, ArXiv Physics e-prints

Krolik, J. H. & Piran, T. 2011, *Swift J1644+57: A White Dwarf Tidally Disrupted by a* 10^4 $M_{\odot}$ *Black Hole?*, ApJ, 743, 134

Lenzen, R., Hartung, M., Brandner, W., Finger, G., Hubin, N. N., Lacombe, F., Lagrange, A., Lehnert, M. D., Moorwood, A. F. M., & Mouillet, D. 2003, *NAOS-CONICA first on sky results in a variety of observing modes*, in Presented at the Society of Photo-Optical Instrumentation Engineers (SPIE) Conference, Vol. 4841, Society of Photo-Optical Instrumentation Engineers (SPIE) Conference Series, ed. M. Iye & A. F. M. Moorwood, 944–952

Liu, S., Petrosian, V., Melia, F., & Fryer, C. L. 2006, *A Testable Stochastic Acceleration Model for Flares in Sagittarius A**, ApJ, 648, 1020

Markoff, S. & Falcke, H. 2003, *Flares in Sgr A*: A Comparison of Jet-based Models with the Data*, in Bulletin of the American Astronomical Society, Vol. 35, AAS/High Energy Astrophysics Division #7, 606

Markoff, S., Falcke, H., Yuan, F., & Biermann, P. L. 2001, *The Nature of the 10 kilosecond X-ray flare in Sgr A**, A&A, 379, L13

Marrone, D. P. 2006, *Submillimeter properties of Sagittarius A*: The polarization and spectrum from 230 to 690 GHz and the submillimeter array polarimeter*, PhD thesis, Harvard University

Marrone, D. P., Moran, J. M., Zhao, J.-H., & Rao, R. 2006a, *Interferometric Measurements of Variable 340 GHz Linear Polarization in Sagittarius A**, ApJ, 640, 308

—. 2006b, *The Submillimeter Polarization of Sgr A**, Journal of Physics Conference Series, 54, 354

Marscher, A. P. 1983, *Accurate formula for the self-Compton X-ray flux density from a uniform, spherical, compact radio source*, ApJ, 264, 296

—. 2009, *Jets in Active Galactic Nuclei*, ArXiv e-prints, arXiv:0909.2576

Melia, F. 2007, The Galactic Supermassive Black Hole (Princton University Press)

Meyer, L., Do, T., Ghez, A., Morris, M. R., Witzel, G., Eckart, A., Bélanger, G., & Schödel, R. 2008, *A 600 Minute Near-Infrared Light Curve of Sagittarius A**, ApJ, 688, L17

Meyer, L., Do, T., Ghez, A., Morris, M. R., Yelda, S., Schödel, R., & Eckart, A. 2009, *A Power-Law Break in the Near-Infrared Power Spectrum of the Galactic Center Black Hole*, ApJ, 694, L87

Meyer, L., Eckart, A., Schödel, R., Duschl, W. J., Mužić, K., Dovčiak, M., & Karas, V. 2006a, *Near-infrared polarimetry setting constraints on the orbiting spot model for Sgr A* flares*, A&A, 460, 15

Meyer, L., Schödel, R., Eckart, A., Duschl, W. J., Karas, V., & Dovčiak, M. 2007, *On the orientation of the Sagittarius A* system*, A&A, 473, 707

Meyer, L., Schödel, R., Eckart, A., Karas, V., Dovčiak, M., & Duschl, W. J. 2006b, *K-band polarimetry of an Sgr A* flare with a clear sub-flare structure*, A&A, 458, L25

Ott, T., Eckart, A., & Genzel, R. 1999, *Variable and Embedded Stars in the Galactic Center*, ApJ, 523, 248

Porquet, D., Grosso, N., Predehl, P., Hasinger, G., Yusef-Zadeh, F., Aschenbach, B., Trap, G., Melia, F., Warwick, R. S., Goldwurm, A., Bélanger, G., Tanaka, Y., Genzel, R., Dodds-Eden, K., Sakano, M., & Ferrando, P. 2008, *X-ray hiccups from Sagittarius A* observed by XMM-Newton. The second brightest flare and three moderate flares caught in half a day*, A&A, 488, 549

Porquet, D., Predehl, P., Aschenbach, B., Grosso, N., Goldwurm, A., Goldoni, P., Warwick, R. S., & Decourchelle, A. 2003, *XMM-Newton observation of the brightest X-ray flare detected so far from Sgr A**, A&A, 407, L17

Priestley, M. B. 1982, Spectral Analysis and Time Series, sixth edn. (Academic Press, London)

Rafelski, M., Ghez, A. M., Hornstein, S. D., Lu, J. R., & Morris, M. 2007, *Photometric Stellar Variability in the Galactic Center*, ApJ, 659, 1241

Reid, M. J., Readhead, A. C. S., Vermeulen, R. C., & Treuhaft, R. N. 1999, *The Proper Motion of Sagittarius A*. I. First VLBA Results*, ApJ, 524, 816

Revnivtsev, M. G., Churazov, E. M., Sazonov, S. Y., Sunyaev, R. A., Lutovinov, A. A., Gilfanov, M. R., Vikhlinin, A. A., Shtykovsky, P. E., & Pavlinsky, M. N. 2004, *Hard X-ray view of the past activity of Sgr A* in a natural Compton mirror*, A&A, 425, L49

Rousset, G., Lacombe, F., Puget, P., Hubin, N. N., Gendron, E., Fusco, T., Arsenault, R., Charton, J., Feautrier, P., Gigan, P., Kern, P. Y., Lagrange, A., Madec, P., Mouillet, D., Rabaud, D., Rabou, P., Stadler, E., & Zins, G. 2003, *NAOS, the first AO system of the VLT: on-sky performance*, in Presented at the Society of Photo-Optical Instrumentation Engineers (SPIE) Conference, Vol. 4839, Society of Photo-Optical Instrumentation Engineers (SPIE) Conference Series, ed. P. L. Wizinowich & D. Bonaccini, 140–149

Sabha, N., Witzel, G., Eckart, A., Buchholz, R. M., Bremer, M., Gießübel, R., García-Marín, M., Kunneriath, D., Muzic, K., Schödel, R., Straubmeier, C., Zamaninasab, M., & Zernickel, A. 2010, *The extreme luminosity states of Sagittarius A**, A&A, 512, A2

Scargle, J. D. 1982, *Studies in astronomical time series analysis. II - Statistical aspects of spectral analysis of unevenly spaced data*, ApJ, 263, 835

Schödel, R., Najarro, F., Muzic, K., & Eckart, A. 2010, *Peering through the veil: near-infrared photometry and extinction for the Galactic nuclear star cluster. Accurate near infrared H, Ks, and L' photometry and the near-infrared extinction-law toward the central parsec of the Galaxy*, A&A, 511, A18

Schödel, R., Ott, T., Genzel, R., Hofmann, R., Lehnert, M., Eckart, A., Mouawad, N., Alexander, T., Reid, M. J., Lenzen, R., Hartung, M., Lacombe, F., Rouan, D., Gendron, E., Rousset, G., Lagrange, A.-M., Brandner, W., Ageorges, N., Lidman, C., Moorwood, A. F. M., Spyromilio, J., Hubin, N., & Menten, K. M. 2002, *A star in a 15.2-year orbit around the supermassive black hole at the centre of the Milky Way*, Nature, 419, 694

Simonetti, J. H., Cordes, J. M., & Heeschen, D. S. 1985, *Flicker of extragalactic radio sources at two frequencies*, ApJ, 296, 46

Stark, R. F. & Connors, P. A. 1977, *Observational test for the existence of a rotating black hole in CYG X-1*, Nature, 266, 429

Sunyaev, R. & Churazov, E. 1998, *Equivalent width, shape and proper motion of the iron fluorescent line emission from molecular clouds as an indicator of the illuminating source X-ray flux history*, MNRAS, 297, 1279

Terrier, R., Ponti, G., Bélanger, G., Decourchelle, A., Tatischeff, V., Goldwurm, A., Trap, G., Morris, M. R., & Warwick, R. 2010, *Fading Hard X-ray Emission from the Galactic Center Molecular Cloud Sgr B2*, ApJ, 719, 143

Theiler, J., Eubank, S., Longtin, A., Galdrikian, B., & Doyne Farmer, J. 1992, *Testing for nonlinearity in time series: the method of surrogate data*, Physica D Nonlinear Phenomena, 58, 77

Theiler, J., Linsay, P. S., & Rubin, D. M. 1993, *Detecting Nonlinearity in Data with Long Coherence Times*, Contributions to Mineralogy and Petrology, 2003

Timmer, J. & Koenig, M. 1995, *On generating power law noise.*, A&A, 300, 707

Tokunaga, A. T. 2000, Infrared Astronomy (Cox, A. N.), 143

Trippe, S., Paumard, T., Ott, T., Gillessen, S., Eisenhauer, F., Martins, F., & Genzel, R. 2007, *A polarized infrared flare from Sagittarius A* and the signatures of orbiting plasma hotspots*, MNRAS, 375, 764

Uttley, P., McHardy, I. M., & Papadakis, I. E. 2002, *Measuring the broad-band power spectra of active galactic nuclei with RXTE*, MNRAS, 332, 231

Uttley, P., McHardy, I. M., & Vaughan, S. 2005, *Non-linear X-ray variability in X-ray binaries and active galaxies*, MNRAS, 359, 345

Vaughan, S., Edelson, R., Warwick, R. S., & Uttley, P. 2003, *On characterizing the variability properties of X-ray light curves from active galaxies*, MNRAS, 345, 1271

Whittet, D. C. B., Martin, P. G., Hough, J. H., Rouse, M. F., Bailey, J. A., & Axon, D. J. 1992, *Systematic variations in the wavelength dependence of interstellar linear polarization*, ApJ, 386, 562

Witzel, G., Eckart, A., Buchholz, R. M., Zamaninasab, M., Lenzen, R., Schödel, R., Araujo, C., Sabha, N., Bremer, M., Karas, V., Straubmeier, C., & Muzic, K. 2011, *The instrumental polarization of the Nasmyth focus polarimetric differential imager NAOS/CONICA (NACO) at the VLT. Implications for time-resolved polarimetric measurements of Sagittarius A**, A&A, 525, A130

Yuan, F., Markoff, S., & Falcke, H. 2003, *A Jet-ADAF Model for Sgr A**, Astronomische Nachrichten Supplement, 324, 453

Yuan, F., Quataert, E., & Narayan, R. 2004, *On the Nature of the Variable Infrared Emission from Sagittarius A**, ApJ, 606, 894

Yusef-Zadeh, F., Bushouse, H., Dowell, C. D., Wardle, M., Roberts, D., Heinke, C., Bower, G. C., Vila-Vilaró, B., Shapiro, S., Goldwurm, A., & Bélanger, G. 2006a, *A Multiwavelength Study of Sgr A*: The Role of Near-IR Flares in Production of X-Ray, Soft γ-Ray, and Submillimeter Emission*, ApJ, 644, 198

Yusef-Zadeh, F., Bushouse, H., Wardle, M., Heinke, C., Roberts, D. A., Dowell, C. D., Brunthaler, A., Reid, M. J., Martin, C. L., Marrone, D. P., Porquet, D., Grosso, N., Dodds-Eden, K., Bower, G. C., Wiesemeyer, H., Miyazaki, A., Pal, S., Gillessen, S., Goldwurm, A., Trap, G., & Maness, H. 2009, *Simultaneous Multi-Wavelength Observations of Sgr A* During 2007 April 1-11*, ApJ, 706, 348

Yusef-Zadeh, F., Roberts, D., Wardle, M., Heinke, C. O., & Bower, G. C. 2006b, *Flaring Activity of Sagittarius A* at 43 and 22 GHz: Evidence for Expanding Hot Plasma*, ApJ, 650, 189

Yusef-Zadeh, F., Wardle, M., Cotton, W. D., Heinke, C. O., & Roberts, D. A. 2007, *The Variability of Polarized Radiation from Sagittarius A**, ApJ, 668, L47

Yusef-Zadeh, F., Wardle, M., Heinke, C., Dowell, C. D., Roberts, D., Baganoff, F. K., & Cotton, W. 2008, *Simultaneous Chandra, CSO, and VLA Observations of Sgr A*: The Nature of Flaring Activity*, ApJ, 682, 361

Zamaninasab, M., Eckart, A., Meyer, L., Schödel, R., Dovciak, M., Karas, V., Kunneriath, D., Witzel, G., Gießübel, R., König, S., Straubmeier, C., & Zensus, A. 2008, *An evolving hot spot orbiting around Sgr A**, Journal of Physics Conference Series, 131, 012008

Zamaninasab, M., Eckart, A., Witzel, G., Dovciak, M., Karas, V., Schödel, R., Gießübel, R., Bremer, M., García-Marín, M., Kunneriath, D., Mužić, K., Nishiyama, S., Sabha, N., Straubmeier, C., & Zensus, A. 2010, *Near infrared flares of Sagittarius A*. Importance of near infrared polarimetry*, A&A, 510, A3

List of Figures

1.1. The Galactic Center. 1

1.2. HKL-composite of the nuclear cluster. 2
1.3. The Very Large Telesope. 4
1.4. NAOS/CONICA. 5
1.5. Adaptive optics. 6
1.6. Improvement of the Strehl ratio by the AO system of NACO 7
1.7. Sgr A* in a flaring state 8
1.8. Steady state SED 9

2.1. Map of calibrators. 18
2.2. The concatenated light curve of Sgr A*. 22
2.3. Light curve of Sgr A* with true time support. 23
2.4. Flux density histogram of Sgr A*. 24
2.5. Log posterior probability as a function of the number of bins. 25
2.6. Best piecewise-constant probability density model for the flux densities of Sgr A*. 26
2.7. The normalized flux density histograms of ten calibration stars. 28
2.8. The measurement error as a function of flux density. 29
2.9. Flux density histograms of two background apertures. 29
2.10. Estimation of the goodness parameter p by a Kolmogrov statistic. . . 32
2.11. The scaling parameter α as a function of $x_{\min}$. 32
2.12. Extrapolation of the best power-law fit. 34
2.13. Schematic view of the power-law flux density distribution and the parameters $x_{\min}$, $x^*_{\min}$, x_0 and the background flux density. 35
2.14. Relation between the rms and average flux density 38
2.15. The PSD under transformation. 42
2.16. The structure function of the observed data sample. 43
2.17. Observed and best fitting structure functions. 44
2.18. Simulated lightcurves I. 48
2.19. Simulated lightcurves II. 49
2.20. Simulated lightcurves III. 49

2.21. The observed CDF and 20 randomly selected CDFs of time correlated power-law surrogate data. 50
2.22. The likelihood of extreme flux density excursions. 53

3.1. Angle definitions. 59
3.2. Intensity of partially polarized light as a function of the orientation of the polarimetric analyzer. 59
3.3. Reflection properties of metallic surfaces in Ks-band. 60
3.4. Optical elements of UT4, NAOS & CONICA. 61
3.5. Polarimetric observations with the Wollaston. 63
3.6. Light train in the adaptive optics module NAOS. 63
3.7. Polarimetric measurement of IRS21 in 2005. 65
3.8. Predicted instrumental polarization. 69
3.9. Histogram of flat-field pixel values. 72
3.10. Normalized transmission of the wires grid. 73
3.11. Q and U parameters as a function of time for IRS16C. 79
3.12. Simulation of systematic calibration artefacts. 84
3.13. Polarimetric measurements of Sgr A*, 2006 June 1. 86

A.1. Time series of quality parameters. 89
A.2. Histograms of the guide star seeing, the Strehl ratio, and the atmospheric coherence time. 90
A.3. Integration times and average calibrator flux densities. 90

B.1. Light curves of Sgr A*. 101

C.1. Flux density histograms with different binning. 107
C.2. Comparison of the observed CDF with surrogate data. 108

E.1. Stokes-fits for IRS16NW, IRS16CC, IRS16CC and S67. 113
E.2. Polarimetric light curve from 2007 May 15. 114
E.3. Polarimetric light curve from 2007 May 17. 114

List of Tables

2.1. List of calibrators. 19

3.1. Encoder positions of the HWP. 65
3.2. Material constants of coatings. 67
3.3. Standard stars. 77
3.4. Apparent polarization of sources at the GC. 79

B.1. Basic information for each light curves. 105

E.1. Polarimatric observations in the Ks-band. 115

Danksagung

Diese Dissertation ist in einem Umfeld außergewöhnlich freundlichen Umgangs und weitgehender Unterstützung geschrieben worden, und ich möchte mich hier sehr herzlich bei allen Beteiligten bedanken.

Mein erster Dank gilt meinem Betreuer und Doktorvater Prof. Andreas Eckart. Ihm habe ich meine Einführung in viele wichtige Zweige der wissenschaftlichen Arbeit zu verdanken, von der Datenauswertung bis zur Beobachtungspraxis, von Konferenzvorträgen bis zum Verfassen wissenschaftlicher Artikel. Die intensiven Diskussionen und die Beratung, seine immer offene Tür und die große Freiheit in der Einteilung und Ausrichtung der Arbeit haben die letzten Jahre zu den fruchtbarsten meines Studiums gemacht. Die freundschaftliche Unterstützung auch in nicht dienstlichen Angelegenheiten und natürlich die Einführung in die Preziosen der Science-Fiction-Verfilmungen haben meine Zeit in Köln weit über die Wissenschaft hinaus bereichert.

Ich möchte mich sehr herzlich bei Herrn Prof. Andreas Zilges für seine Bereitschaft bedanken, das Zweitgutachten meiner Arbeit zu übernehmen.

Vielen herzlichen Dank an Prof. Peter Schneider für seine Bereitschaft, sich als dritter Gutachter zur Verfügung zu stellen, sowie für besonders hilfreiche Anregungen und Diskussionen hinsichtlich meiner zukünftigen Arbeit.

Herzlichen Dank auch an Herrn Prof. Claus Kiefer und Dr. Peter Schuller für ihre Bereitschaft, Mitglied meiner Prüfungskommission zu sein.

Ich danke allen meinen hier nicht namentlich aufgeführten akademischen Lehrern.

Vielen herzlichen Dank an PD. Dr. Walter Huchtmeier für seine lebenslange Begleitung und besonders für unsere musikalischen Ausflüge, die mir ein so wichtiger Ausgleich waren.

Ein besonderer Dank gilt PD. Dr. Silke Britzen für viele anregende Diskussionen zu Themen der Wissenschaft, Philosophie und Kultur, für ihr Engagement für COST und ihre zuverlässige Hilfsbereitschaft. Selten hat man die Gelegenheit, mit jemandem zu sprechen, dessen Kenntnisse eine solch große Breite haben.

Ausdrücklich möchte ich mich bei Prof. Anton Zensus bedanken für seine langjährige Beratung und Unterstützung und sein fortwärendes Interesse an meinen Belangen.

Vielen Dank an Dr. Christian Straubmeier für die Unterstützung in allen Computerbelangen.

Dr. Rainer Lenzen, Dr. Rainer Schödel, und Dr. Leo Meyer danke ich für viele interessante Diskussionen.
Meinen Freunden Nicola Marchili, Manolis Angelakis und Alex Karim möchte ich für Diskussionen und all die schönen Stunden danken, die wir zusammen verbracht haben.
Meinem engeren Freundes- und Kollegenkreis am Kölner Institut danke ich für eine großartige Zeit des Austausches und der Zerstreuung, und dafür, dass jeder mich nach Kräften unterstützt hat: Devi Kunneriath, Monik Valencia, Momo Zamaninasab, Nadeen Sabha, Kora Muzic, Angela Vitale, Marcus Bremer, Ban Shazamanian, Senol Yazici, Rainer Buchholz und Gerold Busch. Ich hoffe sehr, dass uns der Kontakt und die Freundschaft auch über Distanz und Zeit hinweg erhalten bleibt.
Ich danke allen Mitarbeitern am I. Physikalischen Institut für die freundliche und kollegiale Atmosphäre, ganz besonders auch Frau Krämer, Frau Krause, Frau Selt, Frau Viersen und Frau Bodendorf.
Ein ganz besonderer Dank gilt der Familie Zetel. Meine nun fast zehnjährige musikalische Ausbildung bei allen Mitgliedern der Familie gehört zu meinen wichtigsten Erfahrungen und meinen kostbarsten Erinnerungen. Ganz besonders gilt dies für Prof. Isaac Zetel, dessen hoher Anspruch, Schüler jeder Begabung nach ihren Fähigkeiten zu fördern, mich tief beeindruckt hat, und dessen Lob mir immer motivierend in Erinnerung bleiben wird.
Peter und Helga Höcker danke ich für ihre freundschaftliche Zuwendung und ihr stetes Interesse an meinem Fortkommen.
Meinem längstjährigen Schulfreund Alex Reinarz danke ich für seine treue Freundschaft.
Schließlich möchte ich mich bei meinen Eltern bedanken. Es ist unmöglich, hier ausreichend zum Ausdruck zu bringen, wie dankbar ich bin für die hingebungsvolle Unterstützung, die ich immer durch sie erfahren habe. Die Tatsache, dass meine Vater auch fachlich sehr zum Gelingen meines Studiums beigetragen hat, ist der Grund, dass ich ihm diese Dissertation widme.
Für diese Arbeit habe ich IDL-Skripte zur Zeitserienanalyse aus der Bibliothek von S. Vaughan benutzt (http://www.star.le.ac.uk/∼sav2/idl.html).
Diese Arbeit ist entstanden im Rahmen der COST action: Black Holes in a Violent Universe.
Diese Arbeit beruht auf Beobachtungen mit YEPUN am VLT UT4 und Daten aus dem Archiv der Europäischen Südsternwarte.

Erklärung

Ich versichere, dass ich die von mir vorgelegte Dissertation selbständig angefertigt, die benutzten Quellen und Hilfsmittel vollständig angegeben und die Stellen der Arbeit – einschließlich Tabellen, Karten und Abbildungen –, die anderen Werken im Wortlaut oder dem Sinn nach entnommen sind, in jedem Einzelfall als Entlehnung kenntlich gemacht habe; dass diese Dissertation noch keiner anderen Fakultät oder Universität zur Prüfung vorgelegen hat; dass sie - abgesehen von unten angegebenen Teilpublikationen - noch nicht veröffentlicht worden ist sowie, dass ich eine solche Veröffentlichung vor Abschluss des Promotionsverfahrens nicht vornehmen werde. Die Bestimmungen der Promotionsordnung sind mir bekannt. Die von mir vorgelegte Dissertation ist von Prof. Dr. A. Eckart betreut worden.

Köln, den 22. Februar 2012

(Gunther Witzel)